ENGINEERING NANOCOMPOSITES AND INTERFACES FOR CONDUCTION AND RADIATION THERMAL MANAGEMENT

A Dissertation

Submitted to the Faculty

of

Purdue University

by

Xiangyu Li

In Partial Fulfillment of the

Requirements for the Degree

of

Doctor of Philosophy

December 2018

Purdue University

West Lafayette, Indiana

THE PURDUE UNIVERSITY GRADUATE SCHOOL
STATEMENT OF DISSERTATION APPROVAL

Dr. Xiulin Ruan, Chair

School of Mechanical Engineering

Dr. Amy Marconnet

School of Mechanical Engineering

Dr. Ali Shakouri

School of Electrical and Computer Engineering

Dr. Liang Pan

School of Mechanical Engineering

Approved by:

Dr. Jay P. Gore

Head of the School Graduate Program

ACKNOWLEDGMENTS

First, I would like to thank my Ph.D. advisor Prof. Xiulin Ruan, who gave me the chance to work in the group and introduced me to the field of nanoscale heat transfer. During my stay at Purdue University, what impresses me is not only his immense knowledge in the field, but also his passion, hard work, patience, and great attention to details. I also want to thank Prof. Ruan for his guidance on my presentation, writing as well as teaching ability while I was a teaching assistant. I want to give my appreciation to the committee members including Prof. Amy Marconnet, Prof. Ali Shakouri, and Prof. Liang Pan, as well as Prof Yue Wu for their support and help during my Ph.D. study.

I want to thank my parents for their continuous mental and financial support, who love me with all their hearts. They have been struggling and working extremely hard all their lives, and continue to do so to help me. I also want to thank the encouragement from my girlfriend, Mian Wang, and I have been enjoying great Chinese food thanks to her excellent cooking skills. I have made many friends, both in Mechanical Engineering and across the Purdue University. They have kept me company and I enjoy everyday with them.

I would like to give my thanks to my collaborators: Prof. Yong P. Chen and Dr. Wonjun Park, who helped me start on sample preparation and thermal characterization, Prof. John A. Howarter and Dr. Alex Bruce, who offered help on composite mixing, Prof. Rebecca Kramer and her student Jennifer Case and Michelle Yuen for their help in composite mixing and viscosity measurement, Prof. Zhi Zhou and Mian Wang for their help in particle dispersion, Dr. Jeffery Meth, who offered great help and advice on particle aggregation. I also want to thank all of the group members, also my friends, who provided me with insights in research: Prof. Bao Hua, Dr. Liangliang Chen, Dr. Jingjing Shi, Dr. Tianli Feng, Prof. Yan Wang, Dr. Zexi Lu, Prof. Zhifeng Huang, Dr. Zuyuan Wang, Prof. Jun Qiu, Dr. Kelly Rickey, Jacob Faulkner, Xuan Li, Jai Singh, Peiyan Yao, Joseph Peoples, Zixuan Zhao, Luis Delgado, Prabudhya Chowdhury and Dr. Tingting Du.

This work was partially supported by National Science Foundation and Cooling Technology Research Center. Some of the experiments were conducted in Birck Nanotechnology Center. Simulations were performed at the Rosen Center for Advanced Computing (RCAC) of Purdue University.

TABLE OF CONTENTS

Page

LIST OF TABLES

LIST OF FIGURES

Figure Page

Figure Page

ABSTRACT

Li, Xiangyu PhD, Purdue University, December 2018. Engineering Nanocomposites and Interfaces for Conduction and Radiation Thermal Management . Major Professor: Xiulin Ruan, School of Mechanical Engineering.

The rapid advance in nanoscale fabrication of nanoparticles and thin films has urged a new perspective in the field of heat transfer. In one of the applications, composite materials, fillers are added in polymer matrix to enhance certain properties. Thermal interface materials are such composites to increase thermal conductivity of polymer for better heat transfer between interfaces. Nanoparticles introduces other mechanisms rarely seen in large fillers, such as aggregation and sintering effect. Such nanocomopsites can be utilized as thermal interface materials for better thermal transport between macro-interfaces. Though thermal interface materials have been studied for decades, aggregation and size effect have never been of great attention as micro-particles diffuse slowly, stay isolated and get separated easily. Thus, aggregation does not show much impact on the overall thermal conductivity. Most of the theoretical models simply ignore aggregation to assume isolated or uniform particle dispersion. However, with size shrinking down to nanometers, nanoparticles diffuse much faster and form clusters more frequently. Along with sintering effect during curing process, clusters with continuous filler phase are common, resulting in a further increase for thermal conductivity. In this work, we focus on the aggregation and size effect on thermal conductivity of metal-polymer nanocomposite. We have fabricated nickel-epoxy nanocomposites and observed higher thermal conductivity than effective medium theory predicts. Contrary to classical models indicate, smaller particles are also found to show higher thermal conductivity with the same particle concentration. A two-level EMA model is developed to account for the aggregation effect and to explain the size-dependent enhancement of the thermal conductivity by introducing local concentration in aggregation structures. An aggregation simulation during the curing process is followed to illustrate

both qualitatively and quantitatively that the size-dependent enhancement of thermal conductivity is caused by the aggregation effect due to higher diffusing speed of the smaller particles. The results help a better understanding on the impact of aggregation, provide guidance in nanocomposite designing and can also apply for other areas such as composite aging process. Metal-nonmetal interfacial thermal resistance that exist in the nanocomposites is further studied in details using thin-film sandwich structures, as quantifying interfaces in nanocomposite is challenging especially with aggregation effect.

Heat generation in modern microelectronic device surges as the number of transistors skyrockets along with the prediction of the Moore's Law. What is worse, with a much higher density of interfaces, especially metal-dielectric interfaces, their contribution has dominated the overall thermal resistance and greatly impeded the thermal management, resulting in one of the largest challenges for enhancing performance nowadays. In this work, in order to decrease gold-alumina interfacial thermal resistance, we inserted an intermediate metal layer nickel between gold and alumina and observed a 70% reduction in total interfacial thermal resistance. Though one more interface is introduced with the inserted nickel layer, the higher electron-phonon coupling factor and the lattice constant of nickel reduce the total thermal resistance. The two temperature model (TTM) is applied to explain the reduction of interfacial resistance, and the results show that the nickel layer functions as a bridge that reduces the phonon mismatch between gold and aluminum oxide. Moreover, nickel has strong electron-phonon coupling, which reduces the thermal resistance caused by the weak electron-phonon coupling in gold.

On the other hand, the thermal conductivity of nanoparticles and thin films changes as the scale goes down to the mean free path of phonons. This size effect opens up more opportunities for thermal conductivity engineering for applications such as thermoelectric energy harvesting. Superlattices or multi-layer structures with minimal lattice mismatch can achieve higher thermal conductivity than expected due to coherent phonons and coupled interfaces. However, such multi-layer structures are rarely seen in actual devices, where the coupling effect of two adjacent thermal interfaces is yet to be well understood. In this work, sandwich structures of aluminum oxide, nickel, and aluminum oxide films are fab-

ricated with atomic layer deposition to study thermal interfacial resistance between metal and dielectric material and interfacial coupling effect across a thin metal layer. Thermal resistances of thin nickel layer and two interfaces are measured with the 3ω method. Experimental results show interfacial thermal resistance between nickel and aluminum oxide as $6.8 \times 10^{-3}\mathrm{mm}^2\mathrm{K/W}$ at 300K, with weak dependence on metal thickness and temperature. Two-temperature model and detailed diffuse mismatch model have been used to estimate interfacial resistance theoretically, and the results agree reasonably well with experiments. Estimations from the two temperature model indicate that in the overall thermal interfacial resistance, the phonon-phonon interfacial resistance dominates over the resistance due to electron-phonon coupling effect and inside the metal layer. Also, the phonon-phonon interfacial resistance does not vary as the metal layer thickness decreases below electron-phonon cooling length indicating the two adjacent interfaces are not thermally coupled.

Additional to function as fillers in thermal interface materials for thermal conduction, nanocomposites have the potential to provide passive radiative cooling as exterior paints, which holds significant promise for reducing the cost of cooling in residential, commercial, and industrial sectors. Passive radiation cooling utilizes a transmission window of the atmosphere between $8\mu\mathrm{m}$ and $13\mu\mathrm{m}$, the sky window, for emission into the deep sky. With a high solar reflectance, such a coating can remain below ambient temperature throughout 24h even under direct sunlight, a potential application for cutting utility bills in commercial and residential buildings. Although there has been decades-long interest to develop paints with radiative cooling capability mainly involving TiO_2, no previous paints have shown cooling below the ambient under direct sunlight, due to insufficient solar reflectance at around 80-85%. Other solutions other than paints utilized complicated photonic structures that are expensive to fabricate, or metallic layer for high solar reflectance. However, in most outdoor equipment for communication network, metal coatings or fillings cause malfunctions as metals interfere with high frequency signals. The lack of a paint form restricts the applications of most exterior surfaces. Here we have demonstrated that with the right fillers, we can achieve below-ambient cooling in paints under direct sunlight with ultra-high efficiency. Barium sulfate and calcium carbonate nanoparticles were selected

for their large intrinsic band gaps which help minimize the absorption in UV. Appropriate particle sizes and high particle concentrations were used to strongly reflect sunlight. The vibrational resonances of the particles or acrylic matrix provide strong emission in the sky window. Our $BaSO_4$-film shows a solar reflectance of 97.6% which is unseen in other paints, and a high sky-window emissivity over 0.93. The resulted cooling power exceeds 110 W/m^2 over the 10am to 2pm period when the average solar irradiation is 930 W/m^2. The surface is cooled 4.5^{o}C below the ambient at noon. Our radiative cooling paints show comparable or better cooling performance than the other state-of-the-art approaches, while offering unprecedented benefits including the convenient paint form, a fraction of the cost of the other approaches, and the compatibility with commercial paint fabrication process.

1. INTRODUCTION

1.1 Particle Aggregation in Particle-Polymer Composite Thermal Interface Materials

With low cost and easy manufacture, excellent mechanical properties as well as strong chemical resistance, polymer such as epoxy, PMMA has been of great significance in modern world. In spite of its high bonding strength and its ability of fill in the gap between interfaces, polymer has a thermal conductivity too low for thermal applications, such as thermal interface materials. Adding fillers with higher thermal conductivity, such as metal, metal oxide, graphene, BN and diamond, helps improve its thermal performance [1]. The improvement depend on volume concentration, thermal conductivity, aspect ratio of the fillers, polymer thermal conductivity as well as interfacial resistance between fillers and polymer. To estimate the overall thermal conductivity of the composite based on these factors, many effective medium approximation models are proposed and reviewed [2–4]. The Maxwell model assumes isolated and spherical particles in matrix material, neglecting any interactions between particles [5,6]. Several modifications, such as the Hamilton model [7] and modified effective medium approximation [8], include a geometry factor of fillers, interfacial resistance and size effect both in filler and matrix material. Utilizing Green's function, Nan has developed a model that treats filler aspect ratio, orientation, and interfacial resistance [9]. However, these models only consider isolated particles, while aggregation effect remains neglected. The Series and Parallel models [10] consider the most simplified geometry of multi-film stacked together. The Bruggeman model [11] was developed for powder compact, and it neglects the effect of continuous phase of the matrix material. The Percolation model [12] for thermal conductivity does include interactions between particles and distinguish particles and matrix, with percolation threshold and percolation exponent as two fitting parameters, though on the assumption that particles still dissipate randomly and

independently. Compared with electrical properties in metal-polymer composites, thermal transport does not show an increase in conductivity as dramatic as electrical conductivity [12–14]. Thus, fitting parameters can be sensitive to experimental data. Some methods for nanofluid utilize hierachical EMA models to include the aggregation effect [15] by using fractal dimensions, which can be difficult to determine [13, 16, 17] especially for composites. These models work relatively well for micro-scale fillers as they are easy separated and staying isolated to provide a uniform composite. However, commercial products using large size of fillers, including thermal pads, grease, can rarely get to thermal conductivity as high as 5W/mK without sacrificing viscosity or affordability due to the lack of filler interactions and continuous phase of high thermal conductivity.

Nanomaterials, such as nanoparticles, nanowire, or graphene, has the potential to offer new opportunities as fillers in thermal interface materials. Due to its high surface-volume ratio and active surface atoms, nano-fillers tend to aggregate faster and harder to separate once clustered together than micro-scale ones. Sintering effect can be possible during the curing process, resulting more and longer continuous paths with high thermal conductivity. Compared with larger particles uniformly dissipated and isolated by insulated polymer matrix, nanoparticles offer higher performance with similar loadings. Pashayi et al utilizes sintering effect occurring during the curing process for a self-construct struture to achieve thermal conductivity as high as $27\mathrm{W/mK}$ with around 45% silver concentration in epoxy [18]. Figure 1.1 illustrate that larger particles stay isolated with low overall thermal conductivity while smaller particles with similar concentration form higher overall thermal conductivity with a longer continuous silver phase. With microwave welding, silver wires with 4% concentration in PDMS achieve thermal conductivity as high as $6\mathrm{W/m^2}$ by connected in a fashion shown in Fig. 1.2 [19]. Even though many EMA models exist for thermal conductivity, most of them ignore aggregation effect due to its complication, underestimating most of nanocomposite thermal conductivity. A better understanding on the aggregation effect on thermal performance as well as structural change is crucial for more efficient composite design.

Interfacial resistance between metal and nonmetal in nanocomposite can be a challenge to quantify with the existence of aggregation and sintering effect. Followed are some studies specifically on metal-nonmetal interfacial resistance.

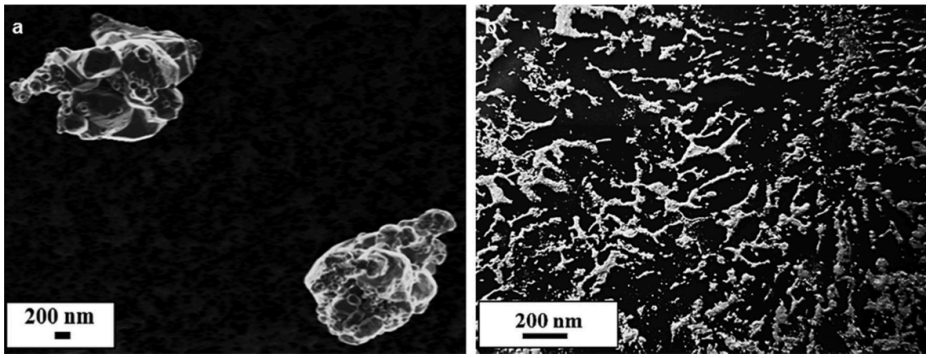

Figure 1.1. : left: isolated micro-scale silver particles in epoxy provide low thermal conductivity around $0.6\mathrm{W/mK}$. right: 20nm silver particles with same concentration in epoxy form continuous path due to sintering effect, and yield thermal conductivity of $27\mathrm{W/mK}$ [18]

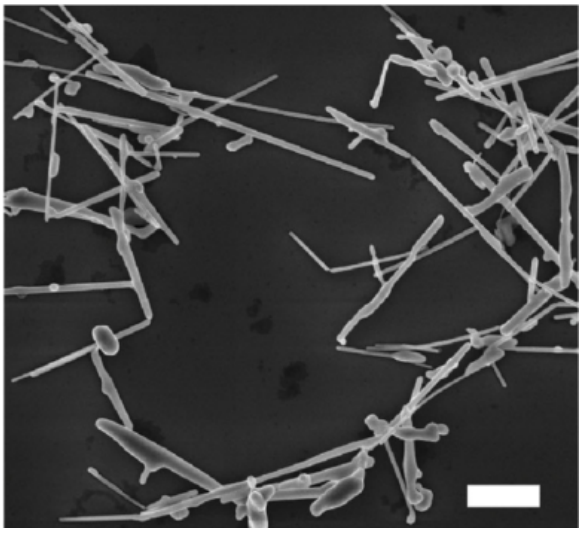

Figure 1.2. : Ag nanowires are microwave welded together to provide continuous path in PDMS for higher overall thermal conductivity. The white bar stands for $1\mu\mathrm{m}$. [19]

1.2 Metal-Dielectric Thermal Interfacial Resistance

The recent development of material synthesis, nanoscale characterization, microelectronic fabrication has pushed the scale of interest down to several nanometers. One of the most significant applications is the integrated circuits, widely applied in modern electronic devices, such as computer processors, mobile phones, memory storage devices, and sensors. The continuous advance in manufacture has made it possible to follow the Moore's Law, that transistor number doubles every 18 months. The transistors are getting smaller as feather length falls from $10\mu\mathrm{m}$ in 1970s to 10nm in 2017. Not only do they get smaller and denser horizontally, they are also stacked multiple layers to ensure performance improvement. However, the power consumption increases, so does heat generation. What makes it worse is that overall thermal resistance increases dramatically as well. Total thermal resistance consists of both that of films and interfacial resistance between films. Thermal resistance for films themselves can be estimated according to Fourier's Law as

$$R''_f = L/k_f, \tag{1.1}$$

where R''_f is the thermal resistance for films, L stands for the thickness of the film, and k is the thermal conductivity of films. On the other hand, interfacial resistance occurs between films, where temperature jumps across the interface. Thermal interfacial resistance R_i between metals and dielectric materials is often in the scale of $10^{-8}\mathrm{m}^2\mathrm{K/W}$. Where as R''_f scales with the thickness of each film, interfacial resistance R_i increases as the number of interfaces surges. When the feature length and film thickness remain rather large, most of thermal resistance comes from thin films themselves that are relatively thermal conductive, and interfaces do not contribute much due to its low resistance($\sim 10^{-8}\mathrm{m}^2\mathrm{K/W}$) [20–24] and smaller count number. As transistors get smaller, thinner films introduce interfaces with much higher density while total thickness of films remain relatively constant. With each interfacial resistance remains similar as before, total thermal resistance now is dominated by the much larger overall thermal interfacial resistance. On the road to higher performance and more compact integration, thermal management has become one of the biggest challenges, and decreasing thermal interfacial resistance is the key.

To measure thermal interfacial resistance, 3ω method [25–27] as well as time-domain thermoreflectance (TDTR) [28] are often utilized. Figure 1.3 [29] shows an example of interfacial resistance measured by 3ω method between Au and Si in a multi-layer structure. A schematic view of TDTR method is illustrated in Fig. 1.4 [28]. The sample surface is usually deposited with gold or other metal. A high-frequency pump light pulse as well as a delayed weaker probe pulse shines on the metal surface, reflected into a detector. The pump pulse excites the sample surface, causing changes in optical properties. Probe pulse carries the information back to the detector. Associated with the changing optical properties, thin film or interfacial resistance is obtained.

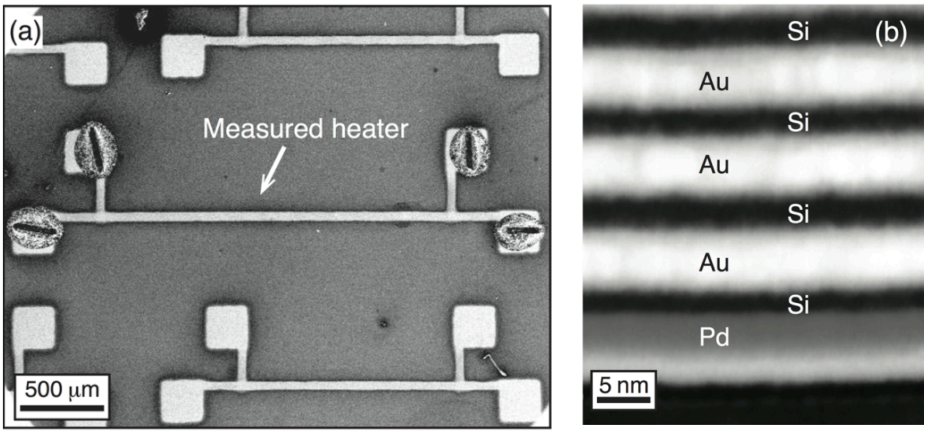

Figure 1.3. : An example of 3ω method is applied for thermal interfacial resistance measurement. (a) A metal line deposited on the surface, necessary for 3ω measurement (b) A multi-layer structure of Au and Si [29]

Things get worse as most of the interfaces in modern electronic devices are metal-dielectric interfaces. For interfaces between dielectric materials, there are many approaches to estimate interfacial resistance, such as acoustic mismatch model (AMM) [30, 31], and diffuse mismatch model (DMM) [31]. These two models can reach reasonable agreement with experiments at low temperatures below 40K depending on different interface conditions, given phonon spectrum of each material. Certain modifications [32] are proposed for high temperatures, by introducing and relying on parameters fitted with experimental data, though the use of such fitting parameters may make the agreement coincidental. The

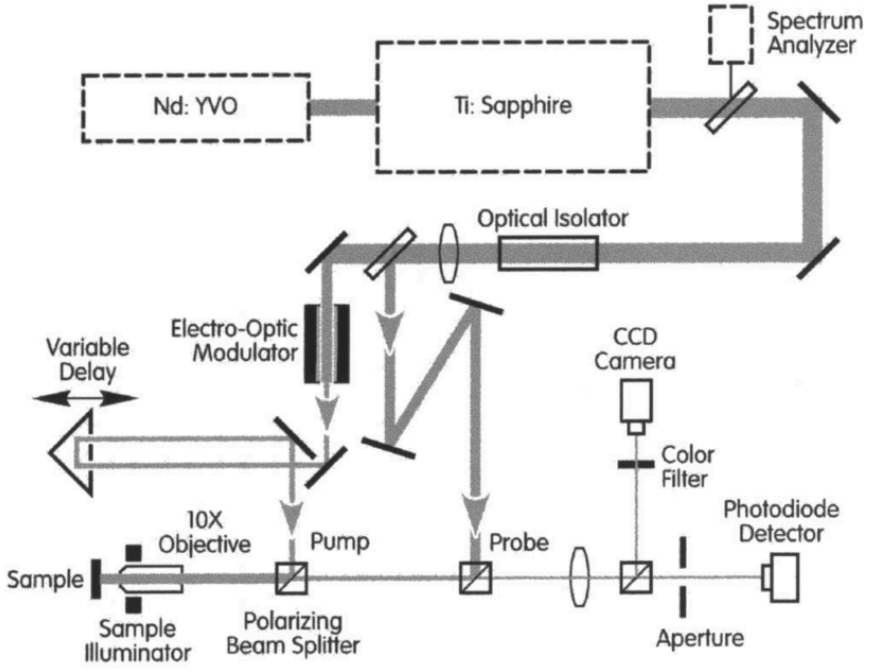

Figure 1.4. : A schematic view of a TDTR setup in use at the Laser Facility of the Frederick Seitz Materials Research Laboratory [28]

method mentioned above can only account for thermal transfer through phonons, ignoring the contribution of other carriers. For metals, semimetals, or heavily doped semiconductors where electron is the main carrier of heat transfer, its contribution to heat transfer cannot be neglected. Due to differences in main heat carriers, electrons and phonons at different sides of the interface between metal and dielectric materials may have a large difference in kinetic energy, as shown in Fig. 1.5, when thermal energy has to be transferred from electrons to phonons in metal before crossing to dielectric material, where phonons are the dominant heat carrier [29, 33]. With additional energy transfer occurred during the thermal transport, metal-nonmetal interfacial resistance is often reported to be higher than that between two metals or two dielectric materials.

To reduce thermal interfacial resistance on lattice mismatch aspect, English et al [34] illustrated in molecular dynamics (MD) that an intermediate layer between two materials with highly vibrationally mismatch can help reduce total resistance. Both the thickness of

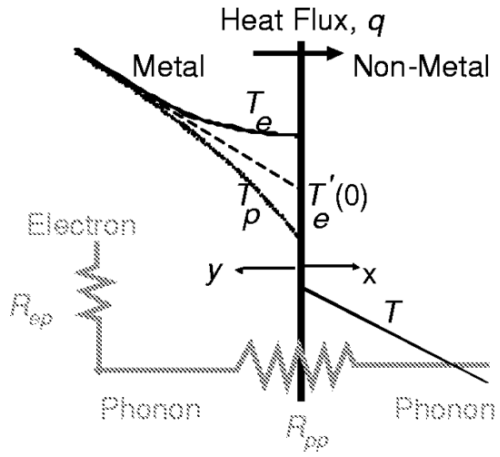

Figure 1.5. : Electron-phonon coupling effect happens at metal-nonmetal interfaces. Electron has to transfer heat to phonon in metal material before thermal energy crosses to nonmetal material. [33]

the interlayer and the disorder of the interfaces are studied in their simulations, shown in Fig. 1.6. Wang et al [35] stepped it further to consider electron-phonon coupling effect in Boltzman transport simulation as well. In a similar fashion that an interlayer help ease the lattice mismatch between two materials, it can also be beneficial for electron-phonon coupling. Gold is often used in microelectronics due to its high electrical conductivity and excellent chemical stability. However, low electron-phonon coupling factor indicates a higher resistance regarding to electron-phonon coupling. In Wang's paper, an interlayer is inserted between Au and Si, shown in Fig. 1.7, such as Al and Pt, resulting in a more efficient way for electron-phonon coupling and reduce overall thermal resistance.

1.3 Interface Coupling and Phonon Coherence

Previous discussion is mostly on an assumption that the metal layer is thick enough that electrons are more efficient in thermal transfer in metal, as the resistance of heat carried by phonons is far higher. Electron-phonon cooling length can be defined as the length where electrons and phonons reach equilibrium in metal layer [36]. However, when the thickness

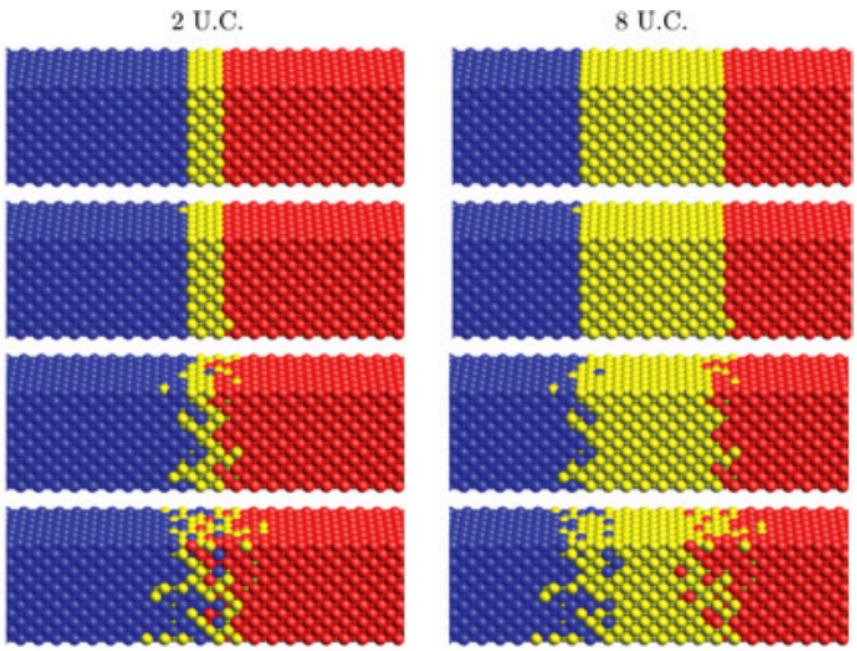

Figure 1.6. : A MD simulation study is focused on how an interlayer helps reduce overall thermal interfacial resistance between two materials with vibrationally mismatch. [34]

of the metal film decreases close to phonon mean free path or the cooling length, thermal resistance of metal layer through phonon channel scales down with the thickness while electron-phonon coupling resistance remains mostly unchanged. In this case, electron-phonon coupling is insufficient for electrons to contribute to for thermal transport. Phonon may be the dominant heat carrier not only in nonmetal material, but also in metal film, illustrated by Li's work in a Mo/Si superlattice [37]. Figure 1.8 shows thermal resistance network with additional phonon channel.

As the film thickness lowers and interface quality improves, coherent phonons are under investigation to yield lower overall thermal resistance. Luckyanova et al [38] has shown coherent phonons in AlAs/GaAs superlattice in Fig. 1.9. Similar result is found by Ravichandran et al [39] using both (STO)m/(CTO)n and (STO)m/(BTO)n superlattice. Figure. 1.10 illustrates that as period thickness, or film thickness decreases into coherent regime, thermal conductivity increases, in other words, each individual interfacial resis-

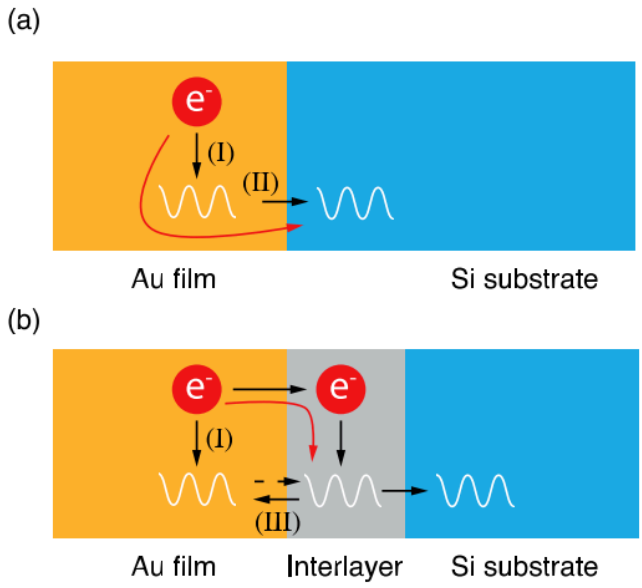

Figure 1.7. : A BTE simulation study regarding to electron-phonon coupling is focusing on how an interlayer helps reduce overall thermal interfacial resistance between metal and dielectric material. [35]

tance decreases. With non-equilibrium molecular dynamics simulation, Wang et al compares superlattice with random multilayer structure [40], shown in Fig. 1.11. The work demonstrates that total resistance is higher for random multilayer as phonon coherency is destroyed. Both the phonon coherency and inefficient electron-phonon coupling contribute to thickness-dependent interfacial resistance. However, they are mostly studied in a multi-layer structure, rather than few-layer or sandwich structure, which is more common in modern integrated circuit.

1.4 Ultra-efficient Low-cost Radiation Cooling Paint

Radiative cooling is a passive cooling method where heat is lost to the deep sky through the transparent ”sky window” from $8\,\mu\mathrm{m}$ to $13\,\mu\mathrm{m}$ of the atmosphere. Emissive power from the earth can directly travel to the deep sky, functioning as an infinite heat sink with temper-

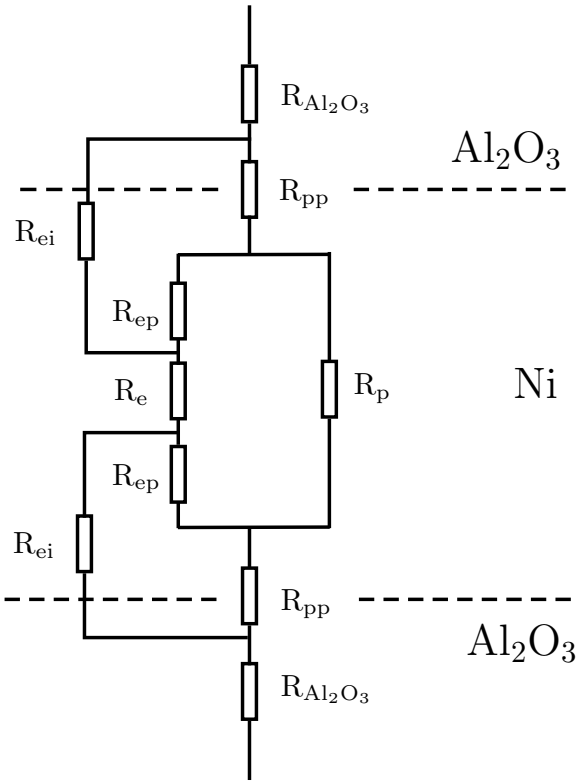

Figure 1.8. : An update on the thermal resistance network by adding a direct phonon channel through the metal layer.

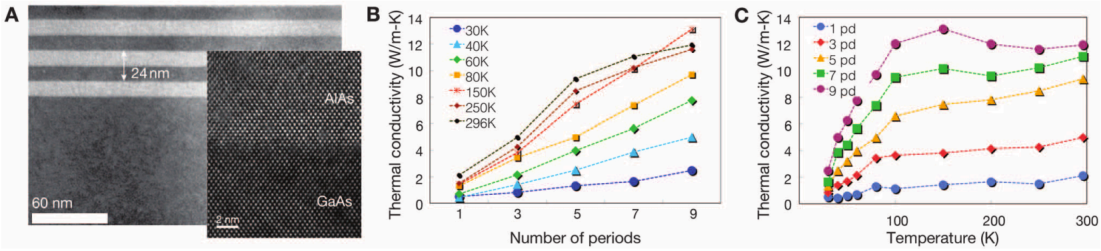

Figure 1.9. : Superlattice with AlAs and GaAs shows linear thermal conductivity increase with superlattice period, indicating phonon coherency is conserved through interfaces. [38]

ature as low as 4K. Combined with high solar reflectance, it is possible to achieve passive refrigeration even under direct sunlight, which holds significant promise for reducing the

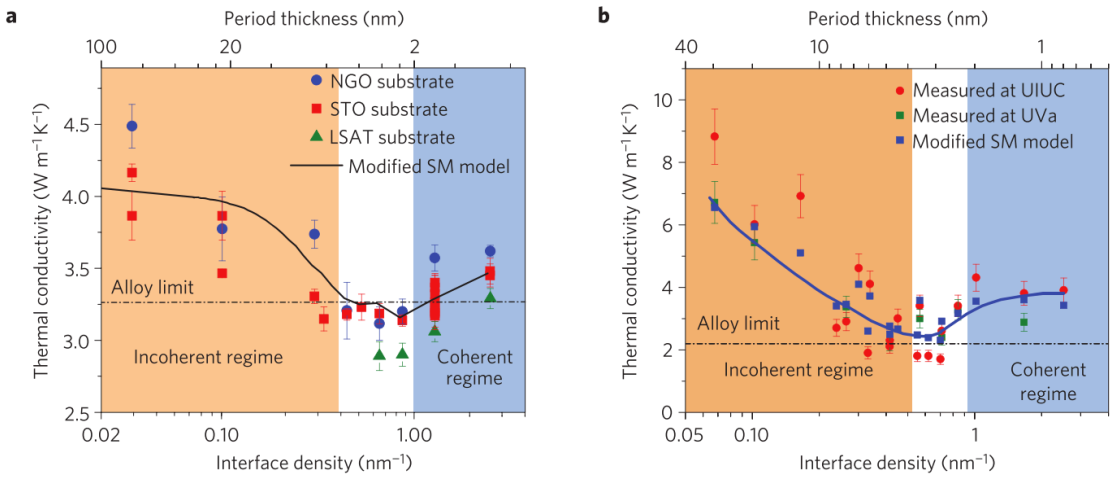

Figure 1.10. : With the period of (STO)m/(CTO)n and (STO)m/(BTO)n superlattices decreases to coherent regime, a further increase in interface density increases overall thermal conductivity, indicating that coherent phonons are beneficial for thermal transport. [39]

cost of cooling in residential, commercial, and industrial sectors. The schematic view of energy flow is shown in Fig. 6.4(a). There have been decades of efforts to create paints with radiative cooling capability under direct sunlight [41–52], most of the studies involved TiO_2 nanoparticles. As the diameter of nanoparticle or the thickness of thin film gets close to solar irradiation wavelength, engineering radiative properties with materials as well as size has proven possible for daytime passive radiation cooling. Unfortunately no previous paints have shown full daytime cooling due to insufficient solar reflectance.

Other approaches are adopted to achieve full daytime cooling. A photonic structure is shown to have both high solar reflectance and sky window emissivity [53]. A multi-layer photonic structure from Stanford University remains 5 degrees cooler than ambient temperature under direct sunlight [54], as shown in Fig.1.13. Unfortunately both designs suffer from complicated structures and expensive fabrication processes. One scalable solution involves silica-TPX nanocomposite with silver backing in Fig. 1.14, which manages to provide $93\mathrm{W}/\mathrm{m}^2$ continuous throughout 24 hours [55]. Another simple design of three

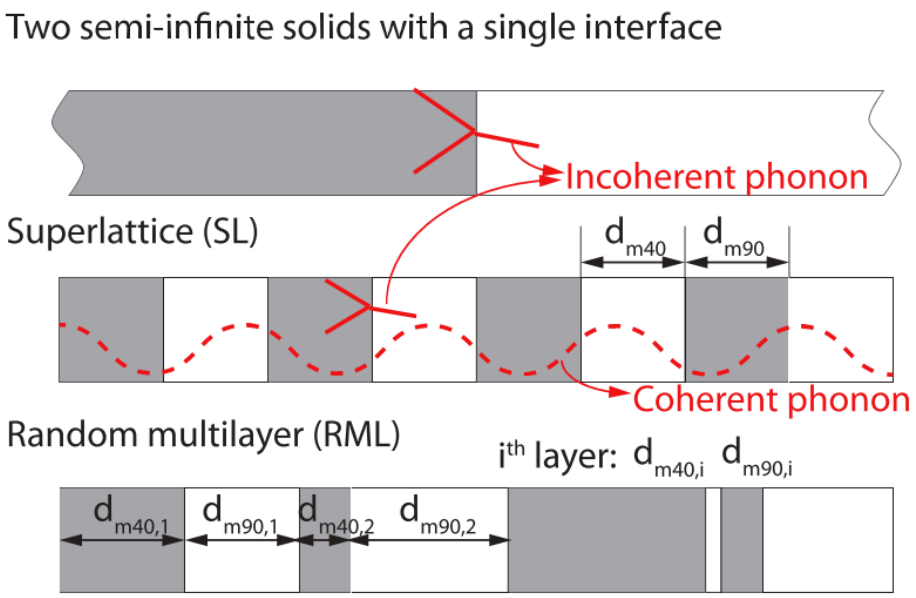

Figure 1.11. : Superlattice is compared with random multilayer to demonstrate the contribution of coherent phonons in thermal transport in non-equilibrium molecular dynamics. [40]

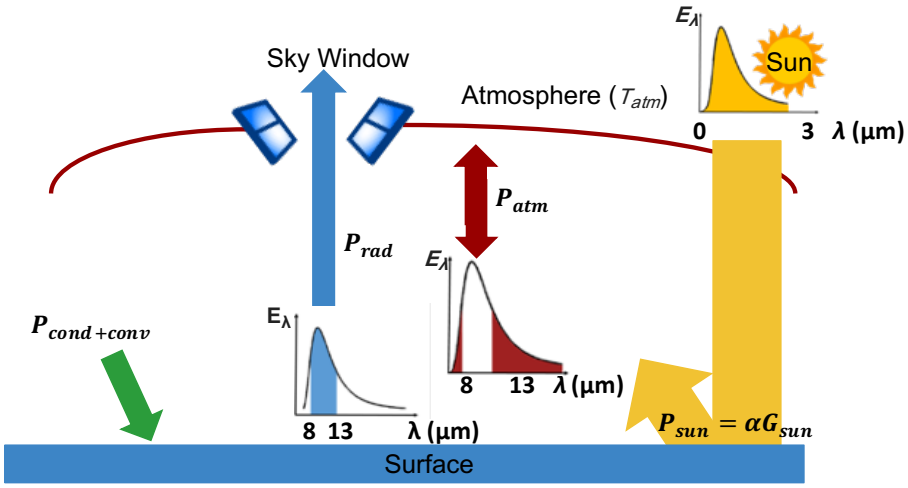

Figure 1.12. : Energy flow of a coating under direct solar irradiation

layers of PDMS, silica and silver, in Fig. 1.15, maintains more than 8 degrees lower than ambient temperature under direct sunlight [56]. However, none of the designs is in paint

form which limits its applications on exterior surface. Furthermore, metal components are present in previous studies to achieve high reflection in solar spectrum as high as 97% and to be mass produced, which may be a problem for some applications [57, 58]. Regarding to most outdoor equipment in communication network, metal coating or component interferes with high frequency signals, which may cause malfunctions. Even in most residential and commercial buildings, coatings containing too much metal will require extra antennas and signal amplifiers to ensure sufficient cell phone receptions. A recent paint-like coating (but not exactly paint) of highly porous poly(vinylidene fluoride-co-hexafluoropropene) achieves full daytime cooling without metallic components [59], while the layer needs to be thicker than $300\,\mu\mathrm{m}$ to be effective, and the material is five times as expensive as acrylic used in commercial paints [60]. Nevertheless, it still remains a pertinent task to develop radiative cooling paints that are high-performance, low-cost, and compatible with commercial paint fabrication process.

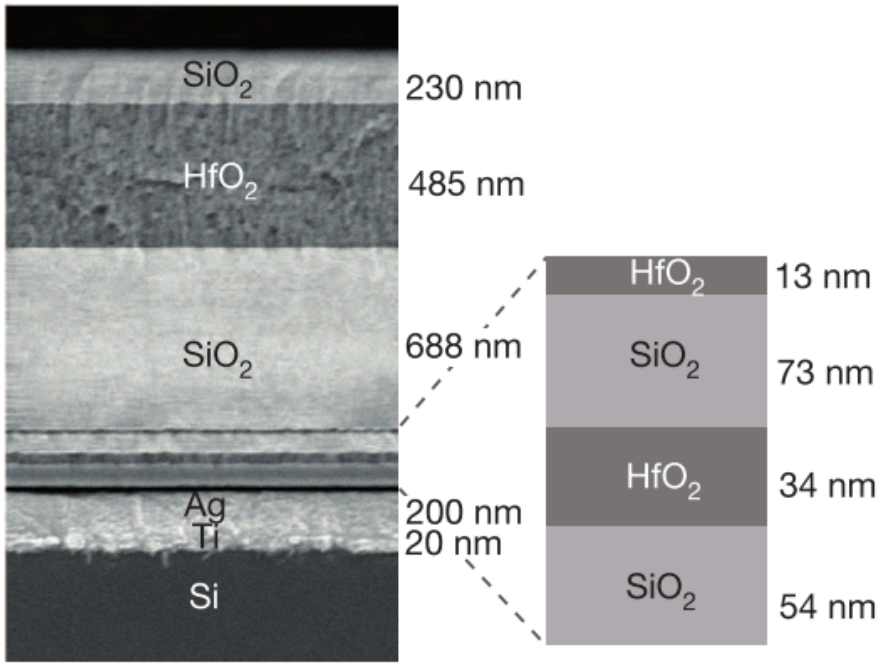

Figure 1.13. : A multilayer photonic structure achieves daytime and nighttime cooling around 5 degrees lower than ambient temperature. [54]

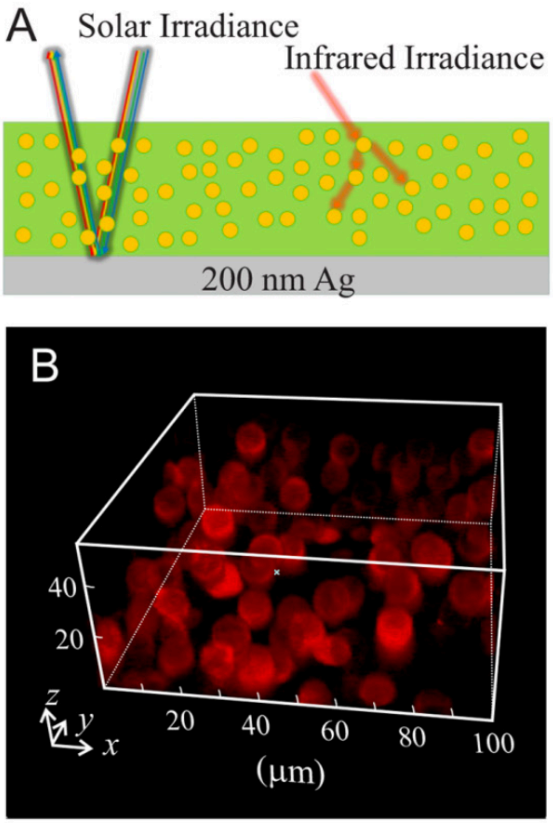

Figure 1.14. : A scalable solution with silica-TPX and Ag backing yields cooling power over 93$\mathrm{W/m^2}$ throughout a day and an average of $\mathrm{W/m^2}$. [55]

1.5 Fabrication Method

1.5.1 Electron-Beam Physical Vapor Deposition

Electron-beam physical vapor deposition is a micro-fabrication method to apply a thin film of certain materials to the target substrate. Illustrated by Fig. 1.17 [61], inside a high vacuum area, electrons coming out of the hot filament travels to the material ingot with the help of magnet field at high speed. The kinetic energy is converted once electron hit upon the evaporant, causing it to melt or sublimate. Once reaching a certain temperature and vacuum level, the material will evaporate and coat on the target substrate. Electron-beam physical vapor deposition is applicable for a wide range of materials with a moderate de-

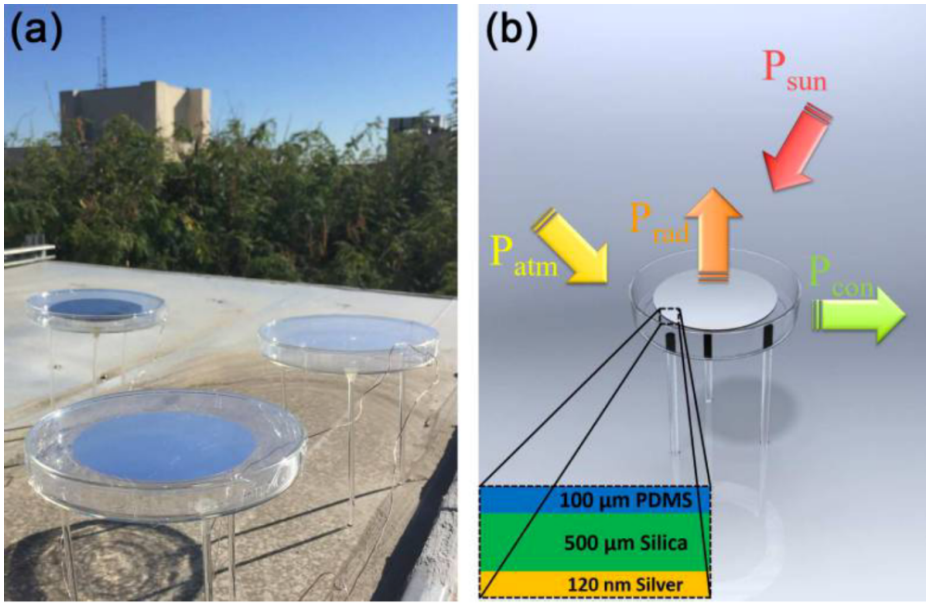

Figure 1.15. : A 3-layer structure of PDMS, silica and silver remains 8 degrees lower than ambient temperature under direct sunlight. [56]

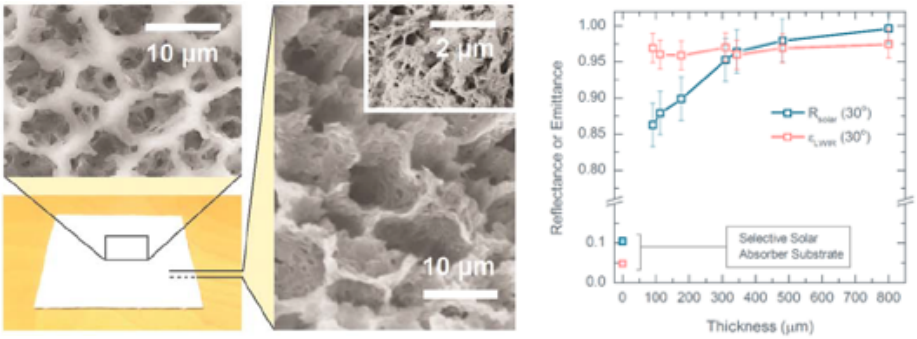

Figure 1.16. : A highly porous P(VdFHFP) shows high solar reflectance and sky window emissivity without metallic component when thickness reaches over $300\,\mu\mathrm{m}$. [59]

position rate. However, the method is only suitable for a simple flat surface, and deposition rate may see some fluctuations during the process.

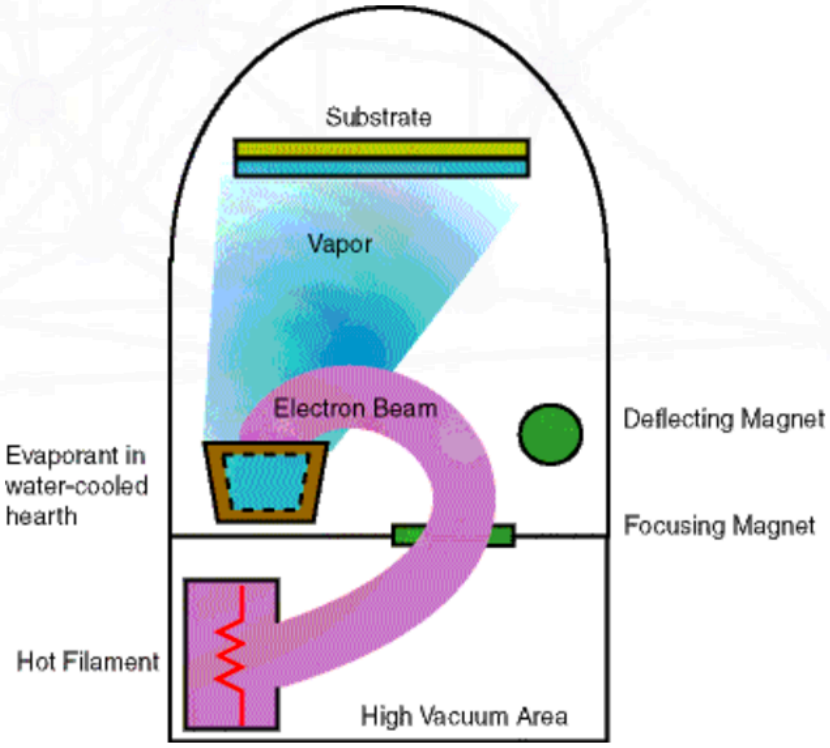

Figure 1.17. : A schematic view on how electron-beam physical vapor deposition works [61]

1.5.2 Atomic Layer Deposition

Atomic layer deposition is a chemical method for thin film deposition with very fine control on the thickness and quality of the films. It works by filling the chamber with a pair of precusors, each at a time. Chemical reactions will occur only at the surface of the sample slowly, resulting in only one layer of atoms deposited on the substrate. Extra precusors will be purged away after each cycle. Figure. 1.18 [62] has showcased the capability of ALD for thin film deposition of uniform thickness and high quality. With such precision, it comes with high cost and very slow deposition rate. Only a list of materials can be deposited successfully, and recipes can also be a challenge to design.

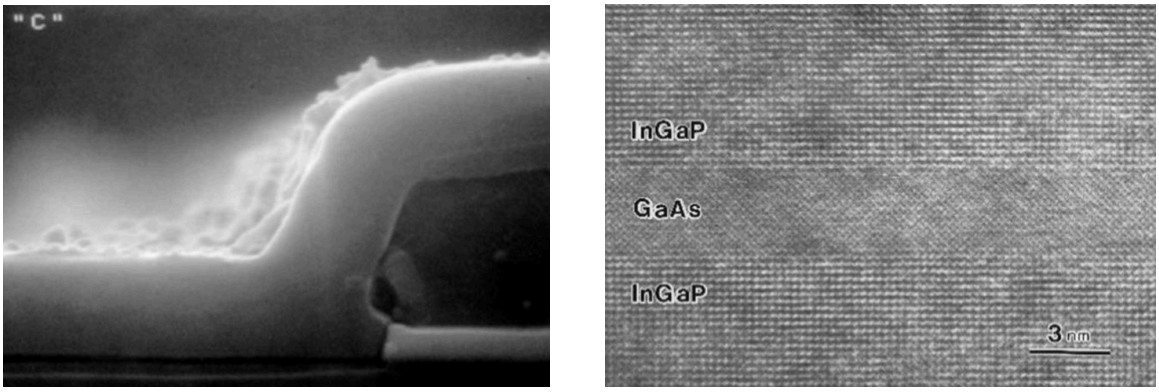

Figure 1.18. : ALD has proven to be one of the best methods to provide a uniform coating even on complex surfaces (left). It also provides thin films of a very high quality (right) [62]

1.6 Thermal Conductivity and Interfacial Resistance Characterization

1.6.1 3ω Method

The original 3ω method was developed by Cahill to measure the thermal conductivity of bulk materials and thin films [25, 26]. The setup is shown in Fig. 1.19. It requires a thin metal line on the surface of the sample, functioning as a heater and detector. Because of the micro-scale metal line, radiation loss even for high temperature is insignificant. There have been different variations on this method to measure thin films, fluid, anisotropic thermal conductivity concerning various materials. During the measurement, an AC current of frequency ω is applied to the metal line, heating up the surface of the sample. The penetration depth depends on the frequency of current and the thermal diffusivity of sample material. With a current of frequency ω, total power consumption of joule heating and temperature of the metal line fluctuate at 2ω frequency, with which, the resistance of the metal line follows accordingly. Considering the ω frequency of the driving current, the voltage between two ends of the metal line includes a 3ω-frequency component. In traditional 3ω method for bulk materials, by analyzing the 3ω voltage, one can obtain temperature oscillation ampli-

tude ΔT in Equation 1.2, where p is the power consumption across the metal line, k, D is the thermal conductivity and thermal diffusivity of the sample, b is half width of metal line.

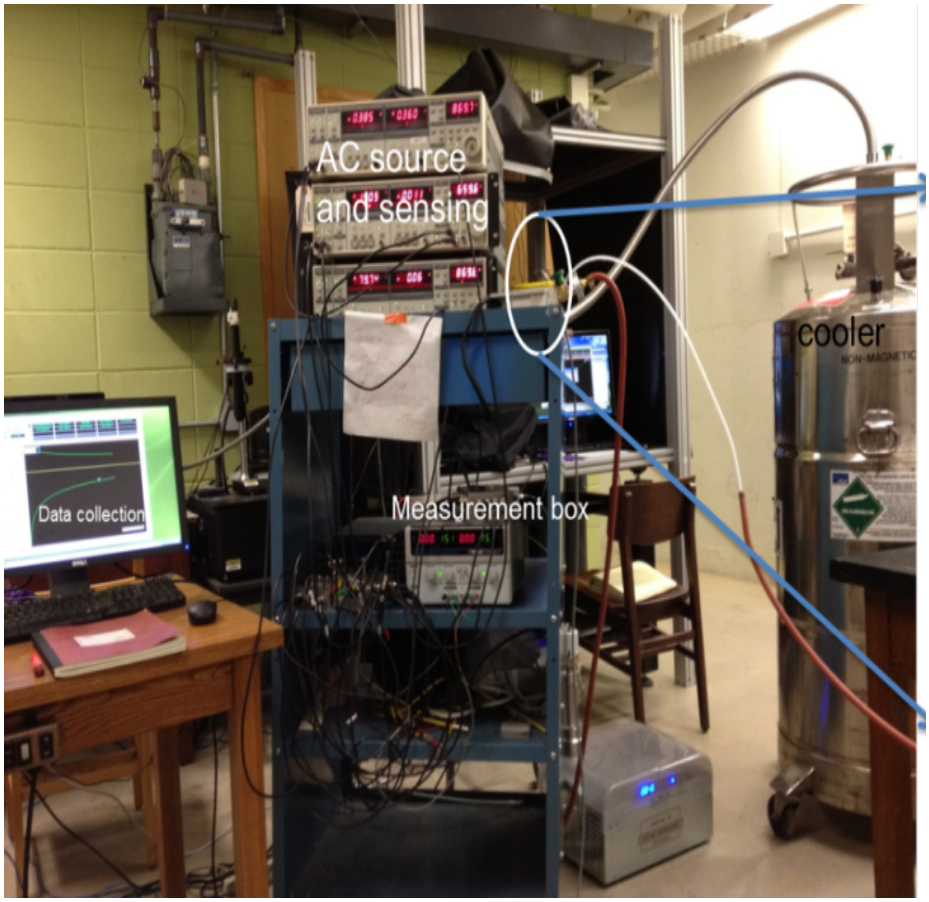

Figure 1.19. : 3ω setup for thermal conductivity characterization and interfacial resistance measurement

Furthermore, we will observe a linear relation between temperature increase and $ln\omega$ in Equation 1.3, as long as the penetration depth ($q^{-1} = (\frac{D}{i2\omega}).^{0.5}$) is much larger than half width b of the metal line. C_{rt} is temperature coefficient for metal line. The bulk thermal conductivity is then obtained from the slope. Three lock-in amplifiers are utilized to monitor AC current, metal line $v_{1\omega}$ and $v_{3\omega}$. However, since the ω frequency part voltage of the metal line remains dominant compared with the 3ω signal, it is necessary to adjust a

resistance to balance out the ω signal, either with two Op-Amplifiers or Whetstone Bridge. It is clear from the equation, that with a higher thermal conductivity, ΔT will be lowered.

$$\Delta T = \frac{p}{\pi k}\int_0^\infty \frac{sin^2(\lambda b)}{(\lambda b)^2(\lambda^2 + 2i\omega/D)^{1/2}}d\lambda \tag{1.2}$$

$$\Delta T = \frac{2v_{3\omega}}{v_{1\omega}C_{rt}} \approx -\frac{p}{\pi lk}(0.5ln\omega + Const) \tag{1.3}$$

A differential 3 ω method [27] is also developed to measure thin film samples by measuring 2 batches of samples separately, one with thin films on substrate, the other without thin films, leading to different temperature changes of metal line even with the same power consumption, according to Eqn. 1.4. By subtracting temperature oscillation amplitude of reference sample from that of thin-film structure, temperature change across thin films can be obtained. If we define thermal impedance as temperature change over power consumption, the thermal impedance difference between two samples can also be calculated with Eqn. 1.5, which is the thermal impedance of the thin film.

$$\Delta T_{R+F} = \Delta T_R + \frac{p}{2bl}R_{diff} \tag{1.4}$$

where p, b, l are the power consumption, half width and length of the metal line. ΔT_R is for reference sample, and ΔT_{R+F} is for sample with thin films. Thermal resistance difference ΔR between samples can be obtained as

$$\Delta R = 2bl\left(\left(\frac{\Delta T}{p}\right)_{R+F} - \left(\frac{\Delta T}{p}\right)_R\right) \tag{1.5}$$

2. AGGREGATION AND SIZE EFFECT ON METAL-POLYMER NANOCOMPOSITE THERMAL INTERFACE MATERIALS

A version of the chapter is published as [63].

2.1 Introduction

Including metal nanoparticles in polymers, such as epoxy, helps to enhance thermal conductivity and to maintain electrical insulation below percolation threshold. Because of the low cost of fabrication, metal-epoxy composite has been a great option for thermal interfacial material in many applications [1]. Aggregation effect is often observed in nanocomposites and attributed as a dominant factor in thermal conductivity enhancement [64–72]. However, its complex morphology posts a great challenge for nanocomposite design and theoretical modeling.

To estimate overall thermal conductivity with fillers, many effective medium approximation models are proposed and reviewed [2–4]. The Maxwell model assumes isolated and spherical particles in matrix material, neglecting any interactions between particles [5, 6]. Several modifications, such as the Hamilton model [7] and modified effective medium approximation [8], include a geometry factor of fillers, interfacial resistance and size effect both in filler and matrix material. Utilizing Green's function, Nan has developed a model that treats filler aspect ratio, orientation, and interfacial resistance [9]. However, these models only consider isolated particles, while aggregation effect remains neglected. The Series and Parallel models [10] consider the most simplified geometry of multi-film stacked together. The Bruggeman model [11] was developed for powder compact, and it neglects the effect of continuous phase of the matrix material. Therefore, the Bruggeman model provides a much lower thermal conductivity when interfacial resistance is considered. The Percolation model [12] for thermal conductivity does include interactions between particles

and distinguish particles and matrix, with percolation threshold and percolation exponent as two fitting parameters, though on the assumption that particles still dissipate randomly and independently. Compared with electrical properties in metal-polymer composites, thermal transport does not show an increase in conductivity as dramatic as electrical conductivity [12–14]. Thus, fitting parameters can be sensitive to experimental data. Some methods for nanofluid utilize hierachical EMA models to include the aggregation effect [15] by using fractal dimensions, which can be difficult to determine [13, 16, 17] especially for nanocomposite. The Backbone method is another three-level homogenization model developed by Prasher, et al. [73, 74]. It relies on two predetermined fractal dimensions. However, it still fails to fit against our experimental data of nanocomposites. Other modeling methods, such as Monte Carlo, Boltzman Transport Equation, or Molecular Dynamics, are limited to simple periodic geometries due to their high computing cost [75].

In our work, we have fabricated nickel nanoparticle-epoxy nanocomposites and observed that they show higher thermal conductivity than effective medium theory predicts even at low concentrations below the percolation threshold. Furthermore, larger enhancement in thermal conductivity is obtained with smaller nanoparticles at the same concentration, contrary to what classical EMA models predict. Thermal conductivity characterization is done by 3ω method, and microscopy analysis by TEM indicates thermal conductivity enhancement and size-dependency are caused by the aggregation effect. A two-level effective medium approximation model is developed to consider inhomogeneous dispersion of nanoparticles, by distinguishing aggregation and global concentrations. Overall, the new two-level EMA model helps explain aggregation effect in nanocomposite and the size-dependent thermal conductivity enhancement, which other EMA models fail to explain.

2.2 Sample Fabrication

Nickel particles of multiple sizes 10nm (10.2 ± 0.2nm), 40nm (37.1 ± 2.2nm), 80nm (80.7 ± 2.5nm), and 1μm ($1.08\pm0.09\mu$m) are used to make nanocomposites. 10nm nickel particles are purchased through mkNano Inc, and other nickel particles are from Skyspring

Nanomaterials. Matrix materials consist of epon 862, epikure W, both purchased from Miller-Stephenson, and curing accelerator epikure 3253 for preventing particle precipitation provided by Matteson-Ridolfi, Inc. Nickel particles, epoxy resin, curing agent, and accelerator are mixed together in THINKY mixer ARE-310 for 10 minutes. The mixture is degassed for one hour, then poured into aluminum mold. Releasing agents are sprayed ahead of time to ensure an easier removal of samples. The curing procedure occurs in an oven, with 30min temperature ramp from room temperature to 121°C with 2h hold, followed by a 30min ramp from 121°C to 177°C and 2h hold, and then a slow cooldown to room temperature [76].

The samples produced are pellets of 2.5mm thickness and 1.5cm in diameter. The top and bottom surfaces are polished to avoid contamination from releasing agent, and to make the surfaces smooth for 3ω measurements. The density is measured before and after polishing to ensure that the volume concentration of nickel is consistent.

2.3 Thermal Conductivity Characterization

Thermal conductivity is measured by the 3ω method [25, 26]. A typical fitting procedure on one of our Ni-epoxy nanocomposite samples is shown in Fig. 4.2, with thermal conductivity obtained as $0.28\mathrm{W/mK}$. The thermal penetration depth is around $25\mu\mathrm{m}$ at 5Hz, $5\mu\mathrm{m}$ at 100Hz and $1.3\mu\mathrm{m}$ at 2000Hz, while the largest size scale of the inhomogeneity due to aggregations is $1\sim3\mu\mathrm{m}$ as seen in Fig. 2.3(b) (Figure 2.3(a) shows smaller inhomogeneity scale). Besides, the inhomogeneity is also averaged across the metal line ($4\mathrm{mm}\times40\mu\mathrm{m}$), which is large enough to obtain an effective thermal conductivity of the sample.

The thermal conductivities of nanocomposites with different nickel particle sizes and volume concentrations are shown in Fig. 2.2, where the Maxwell model curve is also plotted. Without the inclusion of interfacial resistance, the thermal conductivity from the Maxwell model is independent on particle sizes. All of the thermal conductivities are higher than the Maxwell model predicts. Surprisingly, it is also observed that smaller

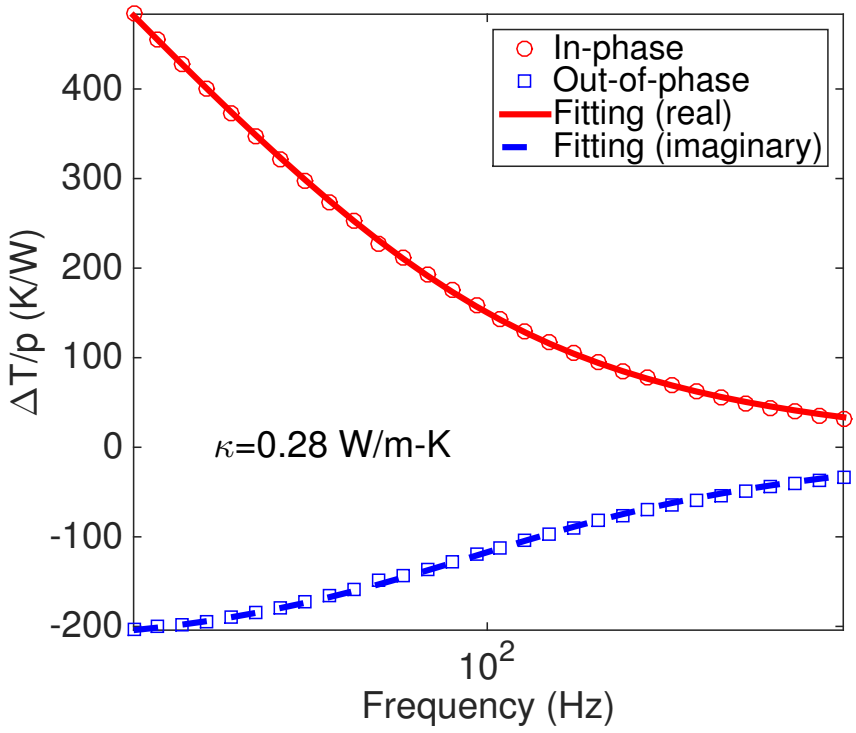

Figure 2.1. : In-phase and out-of-phase 3ω signals (hollow circles and squares) with analytical solution (red solid line and blue dash line) to obtain thermal conductivity of Ni-epoxy nanocomposites.

fillers provide higher thermal conductivity at the same concentration, contrary to the trend of classical EMA models, where thermal conductivity decreases with smaller particles due to interfacial resistance. Motivated by these observations, we slice our composites samples into 100nm thickness and characterize the microscopy structure with transmission electron microscopy(TEM). According to Fig. 2.3, nickel particles (dark dots), are not isolated or located evenly. Instead, they aggregate to form some clusters with high local concentration. Interactions between particles help form a continuous path to conduct heat better within nickel phase, thus increase the overall thermal conductivity more effectively than isolated dispersion. On the other hand, these clusters are mostly isolated from each other. It is also important to note that 40nm nanoparticles form a more spread-out cluster structure than

80nm, which is likely the reason for size-dependent thermal conductivity. In this case, using a single-level EMA model like the Maxwell model would ignore the aggregation effect. On the other hand, although the percolation model considers the aggregation effect, it does not treat the nonuniform particle distribution. In this work, a 2-level EMA is developed to account for the aggregation effect.

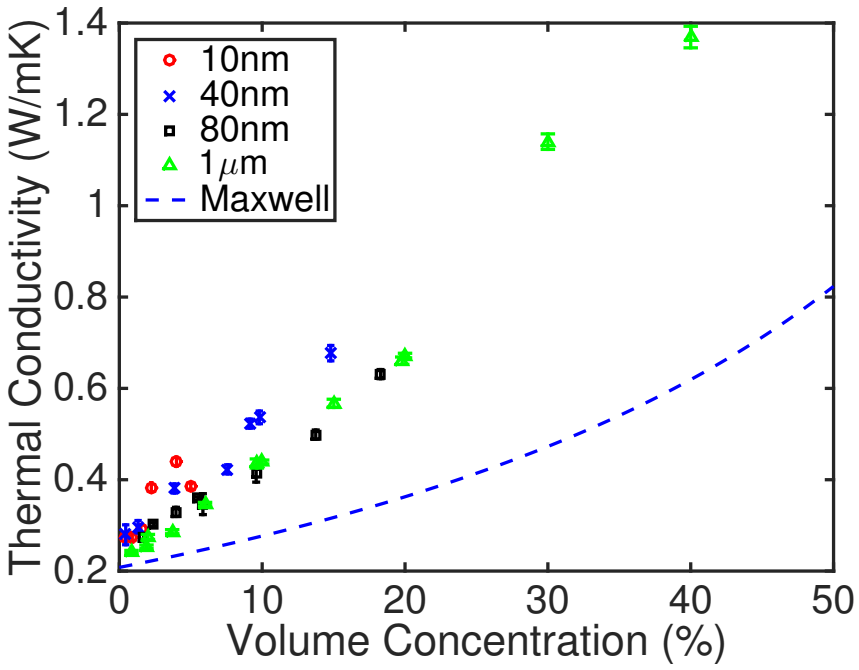

Figure 2.2. : Thermal conductivities of Ni-epoxy composites with different particle sizes and concentrations are compared with the Maxwell model. All thermal conductivities are higher than the Maxwell model and smaller particles yield higher thermal conductivities than larger ones.

2.4 Two-Level EMA Modeling

Our 2-level EMA model adopts a different EMA model at each level, shown in Fig. 2.5. The first level is a cluster where nanoparticles are packed closely, and the second level is the whole composite where each cluster is treated as an isolated new particle. A local

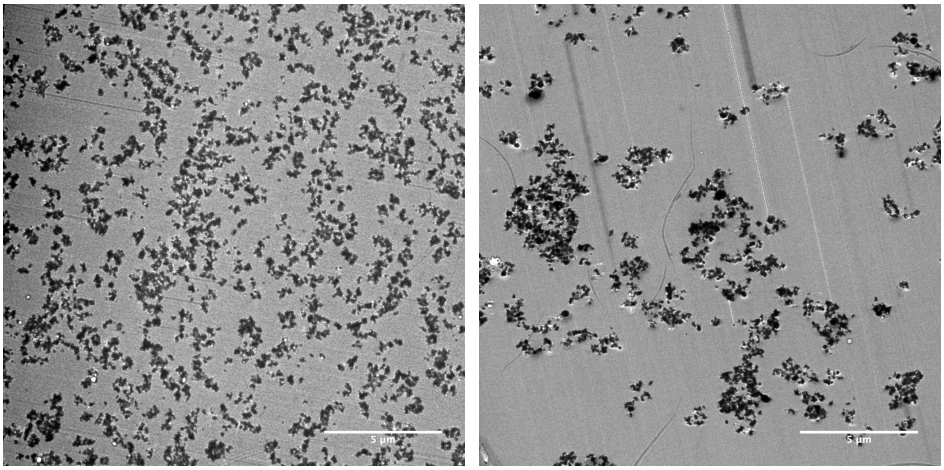

(a) 40nm Ni at 5.74% (b) 80nm Ni at 5.52%

Figure 2.3. : TEM figures of nanocomposites with 40nm and 80nm nickel particles are taken at the same magnification, scale bar set as 5μm for (a) and (b). A more spread-out aggregation structure is observed in nanocomposites with smaller particle size than that in larger one at similar concentrations.

concentration, ϕ_l, is defined as the volume concentration of particles inside clusters. The aggregation concentration ϕ_a, is defined as volume concentration of aggregation structures inside the matrix material. Thus the overall concentration of nanoparticles will be preserved as $\phi = \phi_l \times \phi_a$. For the first level EMA, where particles are packed together and assumed to form a continuous nickel path, the Hashin and Shtrikman model [77] is used as

$$k_{c,o} \quad = k_p \frac{2\phi_l}{3 - \phi_l}, \tag{2.1}$$

where k_p is nickel particle thermal conductivity, ϕ_l is the local volume concentration, $k_{c,o}$ is the thermal conductivity of clusters neglecting interface resistance. Several attempts in literature have shown that with sufficient particle interactions at high concentration, thermal conductivity enhancement can be comparable to the higher bound of the Hashin and Shtrikman model [18, 67–71]. Thermal interface resistance between epoxy and nickel particles can also be included as [78]

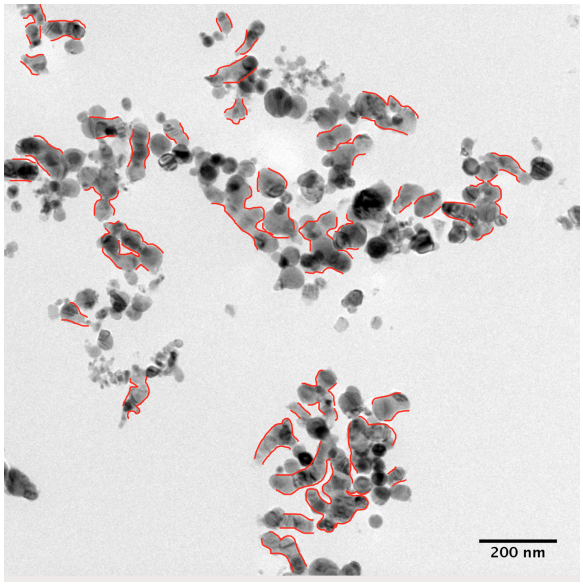

Figure 2.4. : Sintering effect is observed in nanocomposite with 40nm Ni at 5.74%. Red lines are labeled where a continuous path is formed among nanoparticles. The scale bar is set as 200nm.

$$\frac{1}{k_c} = \frac{1}{k_{c,o}} + \frac{2R_i}{d}, \tag{2.2}$$

where k_c is the thermal conductivity of clusters considering interfacial resistance, R_i is the thermal interfacial resistance, and d is the diameter of nickel particles. The interfacial resistance is added in the same manner that it is included for isolated spheres [9]. However, aggregation and sintering effects shown in Fig. 2.4 decrease the surface area significantly and change the shape of clusters [18], resulting in a diminished effect of thermal interfacial resistance on overall thermal conductivity. Thus, simply applying R_i and the diameter of individual particles as d will overestimate the effect of interfacial resistance. Due to its complexity, another model is needed to quantify the exact effect of interfacial resistance due to the agglomerations. On the second level, even though the aggregation structures appear as cylinders, rods, and some irregular shapes in TEM images, the true geometry factor remains uncertain. The TEM figures only show a slice of around 100nm thickness, thus

those agglomerations that seem to be connected together might be relatively distant away, and some small agglomerations might be only part of larger ones. Because of spherical particles and isolated clusters, we assume spherical agglomerations based on the Maxwell model for the second level as

$$k_e = k_m \frac{k_c + 2k_m + 2\phi_a(k_c - k_m)}{k_c + 2k_m - \phi_a(k_c - k_m)}, \tag{2.3}$$

where k_c is the thermal conductivity of clusters, k_e is effective thermal conductivity of nanocomposites, k_m is matrix thermal conductivity, and ϕ_a is the volume concentration of aggregation in epoxy. In this work, thermal interface resistance is set to be $5\times10^{-9}\mathrm{m}^2\mathrm{K/W}$ [79]. We applied a constant interfacial resistance between nickel and epoxy, although it is reported that interfacial resistance may vary depending on particle sizes [79]. The thermal conductivity of nickel particles is estimated based on the mean free path of phonons and the electron cooling length [36], shown in Table 2.1. If the aspect ratio is to be measured or fitted in the model, Nan's model can be an alternative model to include the geometry factor.

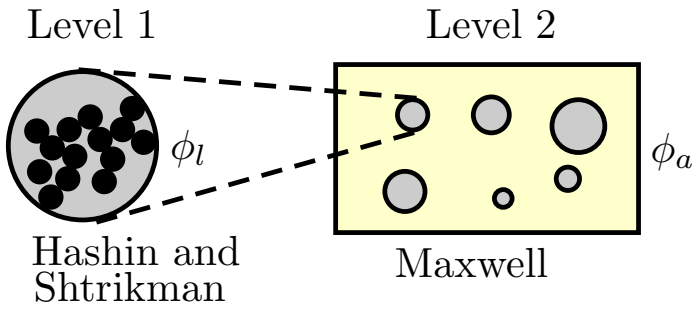

Figure 2.5. : 2-Level EMA model applied two different EMA models to calculate thermal conductivities of the clusters (level 1) and the overall composite (level 2).

The aggregation concentration ϕ_a of each sample is an exact fit with experimental thermal conductivity data based on the 2-level EMA model in Fig. 2.6, where the curve $\phi_a = \phi$ is also included for comparison, representing the Maxwell model. All aggregation concentrations are above the curve $\phi_a = \phi$, indicating higher aggregation concentrations as

Table 2.1. : Thermal Conductivity of Nickel Particles with Size Effect

Particle size	10nm	40nm	80nm	$1\mu\mathrm{m}$
Thermal Conductivity*	36.7	66.0	74.5	90.9

* $\mathrm{W/mK}$

clusters include both particles and matrix materials. Aggregation concentration of smaller particles, such as 40nm, rises higher than that of larger ones, such as 80nm and $1\mu\mathrm{m}$ at the same overall concentration. Even though it means the thermal conductivity of clusters with 40nm particles is lower than that of denser ones, the overall thermal conductivity yields higher as clusters cover more space, with thermal conductivity still much higher than that of epoxy. A comparison is made between 40nm sample at 5.74% and 80nm sample at 5.52% in Table 2.2. Even though 80nm nanocomposite has a higher local concentration, and a higher cluster thermal conductivity, its lower aggregation concentration limits its overall thermal conductivity. Referring to Fig. 2.3 at similar concentrations and the same magnification, aggregation structure of 40nm nanoparticles is more beneficial for heat transfer, since clusters are more spread-out, which translates into larger ϕ_a or smaller ϕ_l. Thus, aggregation effect enhances thermal conductivity compared with isolated particle dispersion, and an extensive aggregation structure or higher aggregation concentration is preferred for higher thermal conductivity.

Table 2.2. : Comparison Between Two Nanocomposites

Particle size	ϕ	ϕ_l	ϕ_a	k_c^*	k_e^*
40nm	5.74%	23%	25.0%	11.1	0.37
80nm	5.52%	35%	15.8%	19.9	0.31

* $\mathrm{W/mK}$

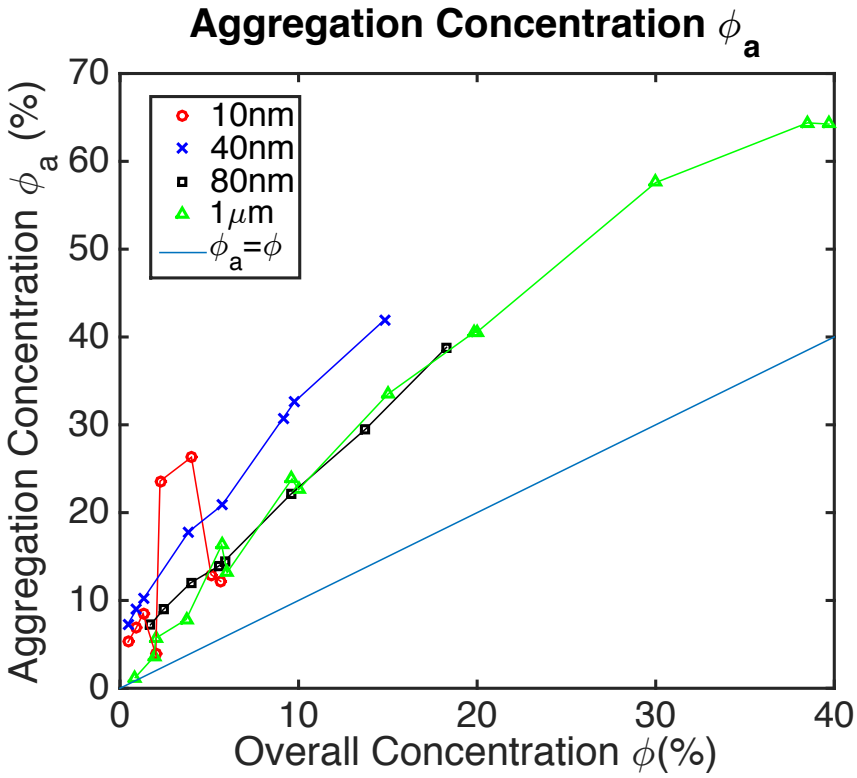

Figure 2.6. : Aggregation concentration of Ni particles in aggregations is plotted with different overall concentrations and nickel particle sizes.

2.5 Conclusion

In this work, we observe higher thermal conductivity of nickel-epoxy nanocomposites compared with other EMA models predict, due to aggregation effect. At the same concentration, smaller particle size shows higher thermal conductivities due to its wider-spread aggregation structures in epoxy, according to TEM figures. A two-level EMA model with the local concentration as a fitting parameter indicates a lower local concentration, higher aggregation concentration for smaller particles, thus a higher effective thermal conductivity than that of nanocomposites with larger particles. Overall, the new two-level EMA model works well with nanocomposites, and helps explain the aggregation effect and size dependent thermal conductivity enhancement.

3. DIFFUSION LIMITED CLUSTER AGGREGATION LATTICE SIMULATION ON THERMAL CONDUCTIVTY

3.1 Introduction

Random aggregation of particles often leads to overall property changes of the whole composite, both mechanical and thermal properties wise. This is often found in nanofluids, the curing period of nanocomposites, or even happening very slowly in the aging process [80–83]. However, the statistical and random nature of aggregation makes experimental characterization of detailed aggregation process expensive and sometimes rather impractical, thus computational models are often utilized. Early computational models of cluster aggregation involves growing clusters by adding one particle or one cluster at a time, such as ballistic growth [84] and ballistic cluster-cluster aggregation [85–87]. Two modern models that produce simulation results closer to realistic aggregation of nanoparticles are diffusion-limited cluster-cluster aggregation [17] and reaction-limited cluster-cluster aggregation [88]. The former one assumes every collision leads to a permanent combination of two clusters, while every merge of clusters takes multiple attempts according to the latter one. In the case of metal particles in polymer matrix, particles and clusters are more inclined to merge with each other rather than bond with polymers. Thus, DLCA will be more appropriate. A Monte Carlo simulation of diffusion-limited cluster-cluster aggregation [17, 89, 90], that can converge with experimental data, can help shine lights on how structures evolve with the aggregation process, and guide the design of most composite materials.

In this work, we are applying diffusion limited cluster aggregation simulation of Ni spherical particles of different sizes in epoxy, with 2% volume concentration to simulate the curing process. We have observed that thermal conductivity increases with aggregation proceeds, and a scalable diffusing time as time over particle volume can help predict

thermal conductivity change regarding to both particle size and aggregation time. The simulation results agree both qualitatively and quantitatively with our previous experiment results [63], that with similar curing time, small particles yield higher overall thermal conductivity. Simulations of higher concentrations of 6% and 10% follow the same trend. However, as the aggregation is enhanced with closer particle-particle distances, the overall thermal conductivity becomes less dependent on particle sizes.

3.2 Simulation Method

3.2.1 Aggregation Simulation

In this work, we are using diffusion-limited cluster aggregation with lattice simulation domain $500\times500\times500$ and period boundary conditions to reduce the finite-size effect in simulation. Each particle is randomly dispersed in the box, occupying one unit cube. The volume concentration v is set as $v = N/L^3$, where N is the number of particles, L is the size of the domain. At the beginning of the aggregation process, particles or small clusters are often well separated in the matrix materials. Any connected particles are set as a cluster. Occasionally, random collisions bring clusters to collide. Depending on different pairs of particle and matrix, either of two cases might be happening [17]. One is diffusion-limited cluster aggregation (DLCA), in which case, clusters form bondings in every collision. The other scenario is reaction-limited cluster aggregation (RLCA), when clusters bind only at a possibility. The former one works mostly when particles tend to have strong attraction with particles, while with the latter one, particles are more likely to bond well with matrix materials. The simulation continues as clusters random walk, and merge as larger ones after collisions. The speed of the random walk is inverted to the size of the cluster, thus as aggregations grow larger, the diffusion process becomes slower. Similarly, larger particles also diffuse slower than smaller particles.

During the aggregation process, the average mean square displacement $< r^2 >$ can be determined by the diffusion coefficient as in Eqn. 3.1. If r is set to be the diameter of the particle, each time step Δt is set as Eqn. 3.2

$$< r^2 >= 6Dt \tag{3.1}$$

$$\Delta t = \frac{d^2}{6D} \tag{3.2}$$

where d is the diameter of the particle, and D is the diffusion coefficient. Diffusing speed is inverted to the diameter of the particle or cluster [74]. A bonding is formed once particles or clusters collide, and the new cluster moves as a whole at a slower speed.

Volume concentration is 2% for curing process to match our previous nanocomposite results. We set curing process effective as 2 hours, when nanocomposite usually begins to harden and aggregation slows down dramatically [76]. In this period of time, diffusion coefficient for 40nm particle is set as $D = 3 \times 10^{-4} \mu\mathrm{m}^2/\mathrm{s}$ [91]. Simulations run for three different sizes of nanoparticles, 40nm, 60nm, and 80nm.

3.2.2 Effective Thermal Conductivity

To get the overall thermal conductivity of the composite sample from aggregation simulation, a random walker method based on Monte Carlo algorithm is applied [92]. Each cell is assigned with a thermal conductivity, either as k_p, nickel particle thermal conductivity, or as thermal conductivity of epoxy, k_e. Continued with the same simulation domain as the previous cluster generation, a random walker is located at a random location. The walker attempts to move into one of its neighbor cells after each time step. The probabilities of successful movement are not uniform, calculated as $P = k_n/(k + k_n)$, where k represents the thermal conductivity of the cell that the walker locates in, and k_n refers to the targeted neighbor cell. The non-uniform probability makes the walker prefer a path with high thermal conductivity, similar to the way how heat is transfered through nanocomposites.

In our work, random walk lasts for 10^8 Monte Carlo steps, ensuring accurate results for thermal conductivity. The displacement r of the walker follows Gaussian distribution, with

an expectation of zero. On the other hand, mean squared displacement (MSD) $< r^2 >$ has a linear relationship with simulation time t, slope of which represents thermal conductivity, as $< r(t)^2 >= 6kt$, where k is the effective thermal conductivity of nanocomposite.

3.3 Results and Discussion

Figure 3.1 shows snapshots of aggregation structures for different particle sizes at various time. Each row represents a particle size, and each column for a time spot. Only a portion of the simulation domain with $2\mu\mathrm{m}$ cube is shown for better illustration. Because of higher diffusion coefficient and larger count for smaller particles, they aggregate faster, and form clusters with more particles.

Figure 3.2(a) plots thermal conductivity continuously increasing during the 2-hour curing process, where 40nm data is represented by blue crosses, 60nm by purple triangles, and 80nm by black squares. Overall, thermal conductivity keeps increase as aggregation proceeds, and thermal conductivity of small particles remain higher than larger ones throughout the process. Since diffusion coefficient D is inverted to particle size, $D = D_0/d$, where d is the particle diameter. Another form of Eqn. 3.3 can be written as

$$\frac{\Delta t}{d^3} = \frac{1}{6D_0}. \tag{3.3}$$

If a scalable diffusing time $t_S = t/d^3$ is applied, thermal conductivities of different particle sizes converge into Fig. 3.2(b), along with experimental results of 2% nickel-epoxy nanocomposite with 40nm, 80nm and $1\mu\mathrm{m}$ particles [63]. Our simulation does not include $1\mu\mathrm{m}$ particles because a domain size suitable for $1\mu\mathrm{m}$ particles will be impractical to other nanoparticles. Due to its much larger diameter, scalable diffusing time for $1\mu\mathrm{m}$ sample will be negligible compared to other nanoparticles. Figure 3.2(b) shows that even diffusing time is set the same, nanoparticles are more inclined to be influenced by aggregation while micro-scale particles are barely affected.

Similar simulations are conducted for 6% and 10% composites for 40nm, 60nm and 80nm, shown in Fig. 3.3. It still holds true that smaller particles (40nm) yield higher thermal conductivity than larger ones (80nm) at the same concentration due to its small particle

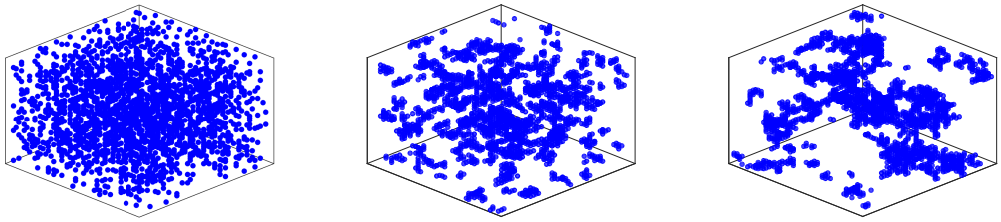

(a) t=0s (b) t=10min (c) t=120min

(a)(b)(c) Nanocomposite with 40nm Ni Particles

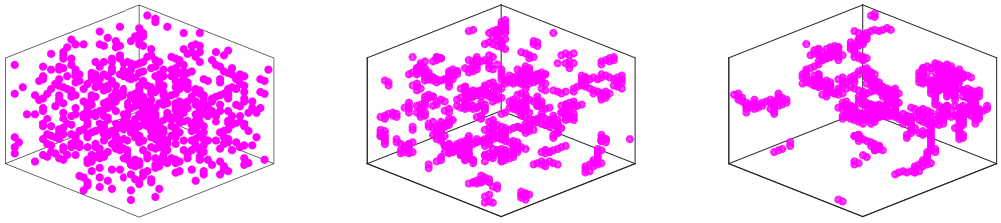

(d) t=0s (e) t=10min (f) t=120min

(d)(e)(f) Nanocomposite with 60nm Ni Particles

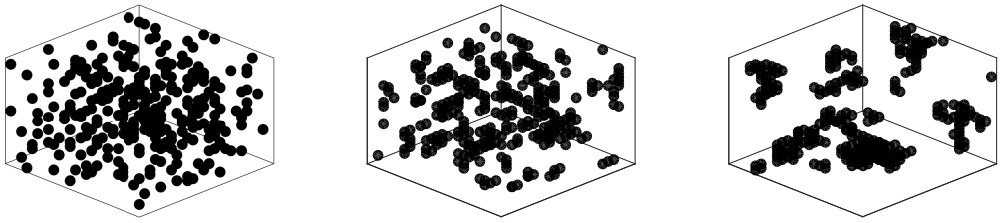

(g) t=0s (h) t=10min (i) t=120min

(g)(h)(i) Nanocomposite with 80nm Ni Particles

Figure 3.1. : Snapshots of Aggregation Structures for Different Particle Sizes

size and larger scalable diffusing time. At 2% concentration where the diffusion process is mostly dominated by individual particles or small clusters, scalable diffusing time of 40nm composite is 8 times of 80nm composite. However, the difference decreases to 7 and 4 times for 6% and 10% concentrations. At higher concentrations, clusters are aggregated more easily due to closer particle-particle distance, making clusters more dominant in the diffusion process than individual particles. Thus, the original particle size has a smaller

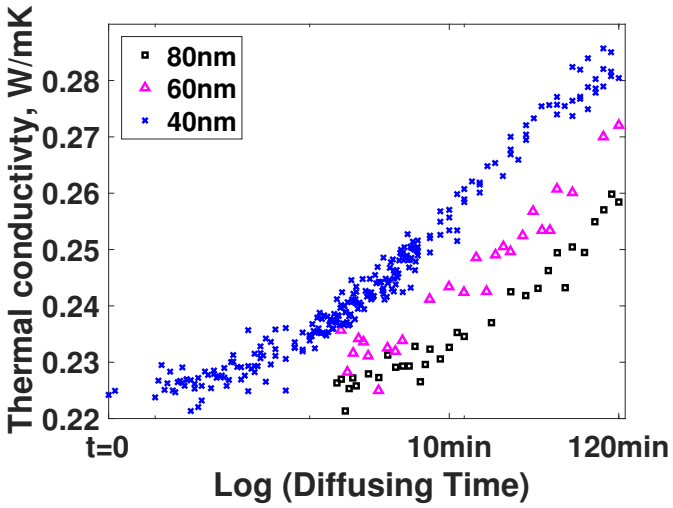

(a) Thermal Conductivity Change with Diffusing Time in 2 Hours for 40nm, 60nm, 80nm Ni Nanoparticles at 2% Concentration

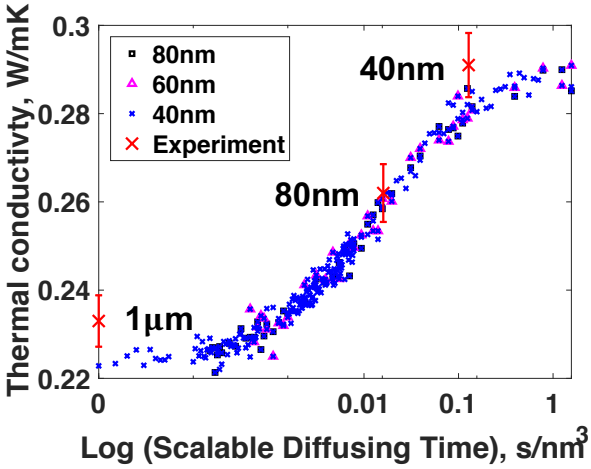

(b) Thermal Conductivity Change with Scalable Diffusing Time Compared with Experiment Results of 2% Nickel-epoxy Nanocomposites

Figure 3.2. : Thermal Conductivity Change with Aggregation

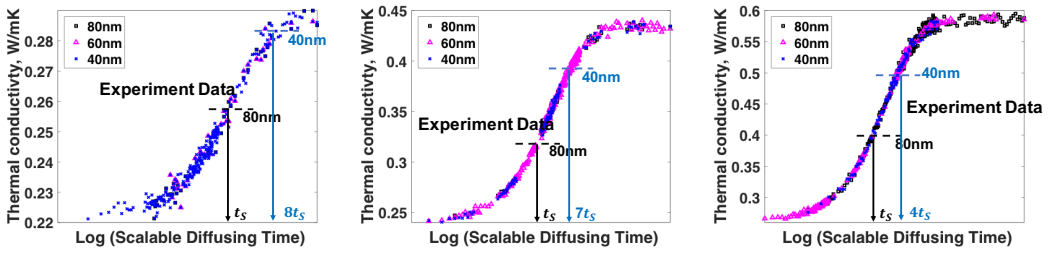

(a) 2% Concentration (b) 6% Concentration (c) 10% Concentration

Figure 3.3. : Thermal conductivity changes are simulated regarding to scalable diffusing time for 2%, 6% and 10% along with experimental results, represented by short dashed lines. The difference of scalable diffusing time is also labeled in the figures.

impact on the diffusion process, so does the aggregation effect. In an extreme case where particles are loaded with over 60% concentration, large clusters will be formed in the early stage of the aggregation process, leading to similar thermal conductivities regardless of particle sizes if interfacial thermal resistance is negligible.

3.4 Conclusion

In this work, we have applied DLCA Monte Carlo simulation for Ni-epoxy nanocomposites at 2% volume concentration with difference nanoparticle sizes. While simulating the curing process, we have observed that thermal conductivity increases as aggregation proceeds, and a scalable diffusing time as time over particle volume can help predict thermal conductivity change regarding to both particle size and aggregation time. Due to smaller size and faster diffusion speed, nanoparticles are more likely to be influenced by aggregation effect, while particles larger than $1\mu\mathrm{m}$ are barely affected, resulting in higher thermal conductivity for nanocomposite with smaller particles. The simulation results agree both qualitatively and quantitatively with our previous experiment results, that with similar curing time, small particles yield higher overall thermal conductivity. Comparing with experimental results, we also find out that the aggregation process will have a

diminishing effect on thermal conductivity at higher volume concentration, as large clusters are formed more quickly with decreasing particle-particle distance.

4. THERMAL INTERFACIAL RESISTANCE REDUCTION BETWEEN METAL AND DIELECTRIC MATERIALS BY INSERTING AN INTERMEDIATE METAL LAYER

A version of the chapter is published as [93].

4.1 Introduction

As the thickness of thin films shrinks to micro/nano-scales, the interfacial resistance between metal and dielectric materials [20–24] ($\sim 10^{-8}\mathrm{m}^2\mathrm{K/W}$) becomes comparable to or dominant over the thermal resistance of thin films ($\sim$10nm) in various engineering applications [32, 94, 95]. In these scenarios, interfacial thermal resistance has become a bottleneck for thermal management of nano-scale electronic devices. It is crucial to reduce such interfacial thermal resistances. For example, gold thin films have been widely used in electronic devices and the next generation data storage technology called heat-assisted magnetic recording (HAMR) [96–98] due to its high conductance, low loss, and chemical stability. The thin films are typically deposited on dielectric substrates which serve as heat sinks. Low interfacial thermal resistance and high thermal conductivity of the dielectric are desired for better thermal management. Unfortunately, the interfacial thermal resistance between gold and dielectric materials is still high. Reported results are around $2\times10^{-8}\mathrm{m}^2\mathrm{K/W}$ when gold is deposited on sapphire substrate [21, 99]. However, when it comes to semiconductor devices, most aluminum oxide thin films for electrical insulation is amorphous [100, 101]. The interfacial thermal resistance further increases to $1.1\times10^{-7}\mathrm{m}^2\mathrm{K/W}$ if amorphous aluminum oxide is used [102]. English et al [34] predicted using molecular dynamics that an intermediate layer to help bridge phonon spectra mismatch led to lower total resistance between metal and dielectric materials. Jeong et al [103] inserted an interlayer of Cu and Cr between gold and sapphire substrate, reducing interfacial thermal resistance considerably, and they attributed the reduction to the bridging

of phonon spectra mismatch. Recognizing that gold has weak electron-phonon coupling which introduces high electron-phonon non-equilibrium resistance, Wang et al [35] proposed to insert a metal interlayer that has stronger electron-phonon coupling to reduce this resistance. However, except for our preliminary work [93], the possible role of electron-phonon coupling has not been evaluated in experiments. Also, such studies have not been done on amorphous aluminum oxide.

In this work, we have fabricated three layered structures on silicon substrates, consisting of gold, nickel, and aluminum oxide layers. The nickel layer was selected primarily because of its higher electron-phonon coupling factor. The interfacial thermal resistance characterization is done by the 3ω method. A 70% reduction of total interfacial resistance is observed after adding the nickel layer. Two temperature model is used to explain the change of interfacial resistance and the modeling results show similar trends with experimental data.

4.2 Sample Fabrication

Three structures, including the reference sample A and two sandwich structures B and C, are fabricated to determine the interfacial thermal resistance between metal and aluminum oxide layer, as shown in Fig. 4.1 with TEM images (Transmission Electron Microscope) and schematic views. The silicon substrate is first cleaned with the RCA method [104] (the Radio Corporation of America), and HF (Hydrogen Fluoride) is used to remove any oxidation layer and contaminations. This is crucial due to low thermal conductivity of silicon dioxide. The reference sample A has 40nm aluminum oxide layer on silicon substrate. Sample B consists of 20nm aluminum oxide layer, 50nm gold layer, and another 20nm aluminum oxide layer on top, preserving the total thickness of aluminum oxide layer. By splitting the aluminum oxide layer into two thinner ones, two gold-aluminum oxide interfaces are created for better measurement sensitivity, without introducing unwanted ones, such as gold-silicon interface. The surface also remains electrically insulating for the 3ω measurement. Sample C inserts 20nm nickel layers in between the gold and aluminum

oxide layers. The aluminum oxide layers are deposited with atomic layer deposition to ensure a consistent thickness, and metal layers are deposited by thermal evaporation. During FIB (Focused Ion Beam) lift-off for TEM images, a Pt layer is deposited on the surface to protect the sample during milling, which is still present in Fig.4.1 as the unlabeled top layer above aluminum oxide.

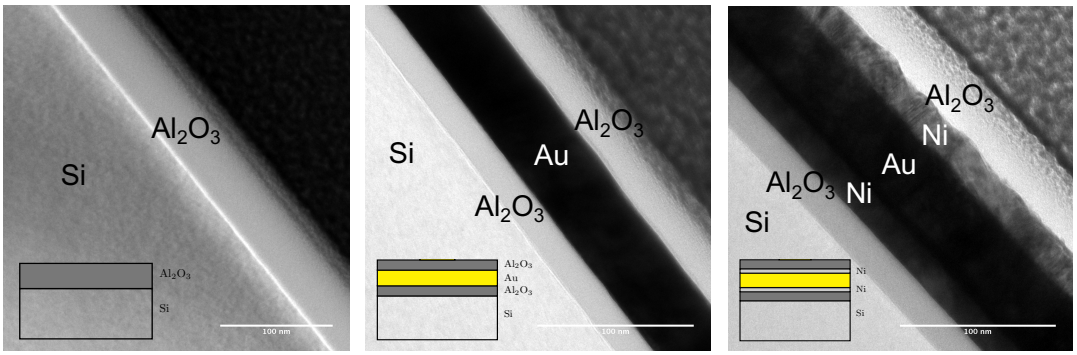

(a) Sample A (b) Sample B (c) Sample C

Figure 4.1. : Sandwich structures fabricated with multiple layers

4.3 Interfacial Thermal Resistance Characterization

The differential 3ω method [25–27] is used to characterize the interfacial resistance in our work. It was developed to measure thin film thermal conductivity and interfacial resistance. In this work, a metal line is deposited as 30μm wide and 3mm long using photolithography. Because of the small size of the metal line, the radiation loss even at high temperature is insignificant. With the joule heating of the metal line under AC current with frequency ω, the surface of the sample experiences a frequency-dependent temperature oscillation amplitude of $\Delta T(\omega)$, and voltage has a frequency of 3ω. Detailed mathematic deviations can be found in literature [25, 26].

$$\Delta T(\omega) = \frac{p}{2bl} R + C_o(\omega) \tag{4.1}$$

where p, b, l are the power consumption, half width, and length of the metal line. C_o is dependent on frequency but remains the same across all three samples. R represents thermal resistance above the substrate. Thermal resistances of Ni and Au layers are neglected due to high thermal conductance and so is the interfacial resistance between them. The amorphous aluminum oxide thin films within 60nm show similar thermal conductivity, reported by DeCoster et al [105]. Thus, thermal resistance of aluminum oxide films is the same across all samples. The thermal resistance above silicon substrate for each sample is

$$R_A = 2R_{\mathrm{Al_2O_3}} + R_{\mathrm{Si-Al_2O_3}} \tag{4.2}$$

$$R_B = 2R_{\mathrm{Al_2O_3}} + R_{\mathrm{Si-Al_2O_3}} + 2R_{\mathrm{Au-Al_2O_3}} \tag{4.3}$$

$$R_C = 2R_{\mathrm{Al_2O_3}} + R_{\mathrm{Si-Al_2O_3}} + 2R_{\mathrm{Ni-Al_2O_3}} + R_{\mathrm{Au-Ni}} \tag{4.4}$$

Subtracting reference Sample A from Sample B and C, we can associate thermal resistance difference ΔR_1 and ΔR_2 with $\Delta T(\omega)$ from 3ω measurement, as shown below [27]

$$\begin{aligned} \Delta R_1 &= R_B - R_A = 2R_{\mathrm{Au-Al_2O_3}} \\ &= 2bl\left(\left(\frac{\Delta T(\omega)}{p}\right)_B - \left(\frac{\Delta T(\omega)}{p}\right)_A\right) \end{aligned} \tag{4.5}$$

$$\begin{aligned} \Delta R_2 &= 2R_{\mathrm{Ni-Al_2O_3}} + 2R_{\mathrm{Au-Ni}} \approx 2R_{\mathrm{Ni-Al_2O_3}} \\ &= 2bl\left(\left(\frac{\Delta T(\omega)}{p}\right)_C - \left(\frac{\Delta T(\omega)}{p}\right)_A\right) \end{aligned} \tag{4.6}$$

where $\Delta T(\omega)$ from 3ω measurement regarding to different samples as well as various frequencies are shown in Fig. 4.2 . Sample B has a overall higher $(\Delta T/p)$, representing higher total resistance than Sample A due to the added Au layer. Sample C sits between Sample A and B, indicating total resistance is lowered as nickel interlayer is added. All three $(\Delta T/p)$ curves are relatively parallel to each other. Thermal resistance difference is calculated from the average of the gaps between the curves at different frequencies. We obtained that the interfacial resistance between gold and aluminum oxide is $4.8 \pm 0.5 \times 10^{-8}\mathrm{m^2K/W}$, and that between the nickel and aluminum oxide is $1.4 \pm 0.1 \times 10^{-8}\mathrm{m^2K/W}$. This indicates a 70% reduction of resistance after inserting the Ni layer. The uncertainties are evaluated based on the variation of these gaps at different frequencies in Eq. 4.5 and

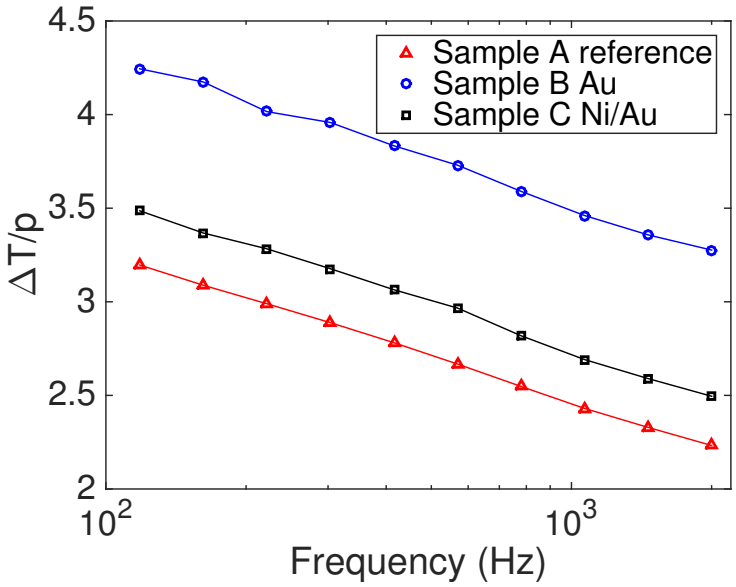

Figure 4.2. : 3ω measurement for three sandwich structures

4.6. In this case, Sample B yields an uncertainty around 11.5%, and Sample C with an uncertainty of 7.9%.

4.4 Theoretical Estimation On Interfacial Resistance

Because our metal-dielectric system involves both electrons and phonons, the two-temperature model suits as the tool for interfacial resistance estimation [33, 36, 106–109], assuming two different temperatures for phonons and electrons respectively in the metal side. Wang et al [36] combined the two temperature model with molecular dynamics to illustrate the impact of electron-phonon coupling effect. The overall interfacial resistance consists of a phonon-phonon component R_{pp}, an electron-phonon nonequilibrium component R_{ep}, as well as an electrical inelastic scattering component, R_{ei}, as shown in Fig. 5.4 [33, 37]. The third component R_{ei} is neglected here.

The first part R_{pp} happens across both metal-dielectric and dielectric-dielectric interfaces. Acoustic mismatch model (AMM) [30, 31], and diffuse mismatch model (DMM) [31] are two models widely used on different interface conditions. The former works

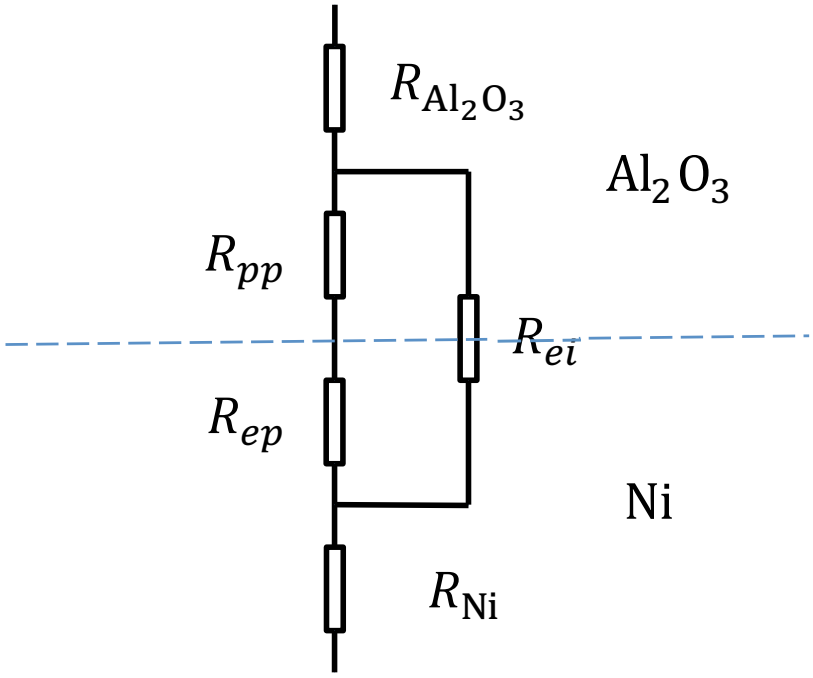

Figure 4.3. : Thermal resistance network between nickel and aluminum oxide

mostly for ideal interfaces at low temperatures, which rarely happens in experiments. Hence we use DMM here, which assumes phonons lose their correlations and randomize directions across the interface. We chose [100] direction for Ni and Au, and [1010] for aluminum oxide for heat flux direction across the interface. The phonon density of states is shown for aluminum oxide, gold and nickel respectively in Fig. 4.4. To calculate phonon dispersion and density of states, we assume crystalline structures of metals and aluminum oxide layer for simplification. Since the metal layers are polycrystalline and aluminum oxide layer is amorphous in our structures, the theoretical results would underestimate interfacial resistance. In Fig. 4.4, both nickel and gold phonons overlap with aluminum oxide phonons at low frequencies where acoustic phonons dominate. Compared with gold, nickel phonons show a larger overlap with aluminum oxide, functioning as a phonon bridge between aluminum oxide and gold phonon frequencies. For phonon transmission coefficient α, $\alpha_{A\to B} = \alpha_{B\to A}$ is satisfied. With that, R_{pp} can be calculated [110]

$$h_{A\to B} = \frac{1}{2\pi A_c}\sum_j \int \hbar\omega M_A(\omega)\alpha_{A\to B}\frac{\partial f}{\partial T}d\omega \tag{4.7}$$

$$\alpha_{A\to B}(\omega^{'}) = \frac{\sum_j M_B(\omega)}{\sum_j M_B(\omega) + \sum_j M_A(\omega)} \tag{4.8}$$

$$M = \pi A_c\,(\frac{v_g}{2})\frac{K(\omega)^2}{2\pi^2 v_g} \tag{4.9}$$

where M is the number of phonon modes, j stands for phonon modes, A_c stands for contact region area, v_g is the group velocity, K is wavevector, and f is the Bose-Einstein distribution function. The results are shown in Table 4.1.

For the resistance due to electron-phonon coupling, the two temperature model considers electron-phonon coupling effect by assigning two temperatures for electrons and phonons. Since electrons are main carriers for heat transfer in most metals, the interfacial resistance based on two temperature model can be written as Eq. (4.10) [33, 36],

$$\begin{aligned} R_i \quad &= R_{pp} + R_{ep} = \frac{1}{h_{pp}} + (\frac{k_e}{k_e + k_p})^{3/2}(\frac{1}{G_{ep}k_p})^{1/2} \\ &\approx \frac{1}{h_{pp}} + (\frac{1}{G_{ep}k_p})^{1/2} \end{aligned} \tag{4.10}$$

Table 4.1. : Comparison between TTM and 3ω measurement

	R_{pp}	R_{ep}	R_i	Experiment
Au-Al_2O_3	20.6*	4.3	24.9	48.4
Ni-Al_2O_3	6.7	0.2	6.9	14.0

* $10^{-9}\mathrm{m}^2\mathrm{K/W}$

where G_{ep} is the electron-phonon coupling factor for metals [107, 111], k_e and k_p are the electron and lattice thermal conductivity of the metal, R_i is the overall interfacial thermal resistance, R_{pp}, h_{pp} are lattice mismatch resistance and conductance respectively, and R_{ep} is the interfacial resistance regarding to electron-phonon coupling effect. G_{ep} is set as $2.88\times10^{17}\mathrm{W/m^3K}$ for nickel, and $2.6\times10^{16}\mathrm{W/m^3K}$ for gold. $k_p = 18.5\mathrm{W/mK}$ for 20nm nickel film and $k_p = 1.5\mathrm{W/mK}$ for 50nm gold film, from first principles calculations [112].

In our study, theoretical estimations using TTM are shown in Table 4.1 along with experimental data. It can be seen that the inserting a Ni layer significantly reduces both R_{pp} and R_{ep}. With Ni interlayer, R_{ep} almost diminishes, and R_{pp} dominates the overall interfacial resistance. Compared with gold, phonons in nickel show a larger match with those in aluminum oxide, resulting in lower phonon-phonon resistance than gold. The difference between experiments and theoretical estimations is mainly due to the fact that we used crystalline phonon properties for $\mathrm{Al_2O_3}$. Adhesion between films is another significant factor leading to poor interfacial thermal resistance [102, 113, 114]. Lahmar et al have measured interfacial thermal resistance of $1.1\times10^{-7}\mathrm{m^2K/W}$ between gold and aluminum oxide, which decreases below $10^{-8}\mathrm{m^2K/W}$ after improving film adhesion by thermal treatment [102]. Despite these simplifications, our model reveals the same trends observed in experiments.

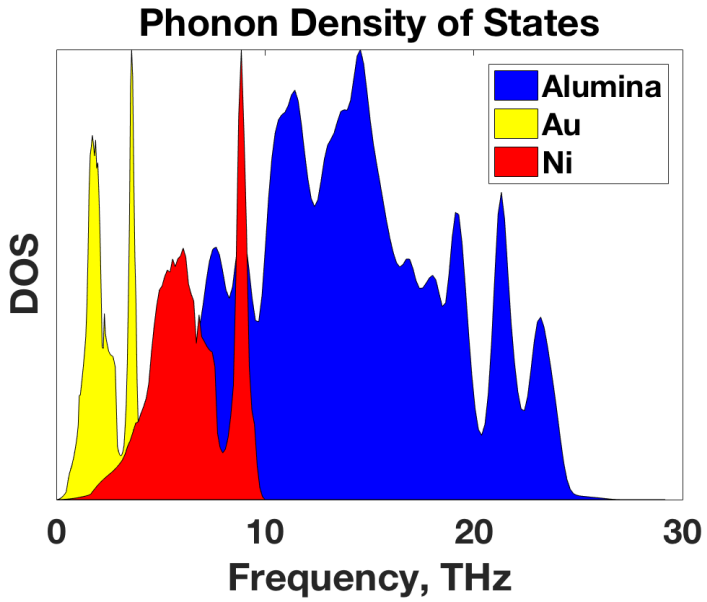

Figure 4.4. : Phonon density of states for Ni, Au, and aluminum oxide

4.5 Conclusion

In this work, we measured the interfacial thermal resistance between gold and aluminum oxide before and after inserting a Ni interlayer. The interfacial resistance decreases by 70%, from $4.8\times10^{-8}\mathrm{m}^2\mathrm{K/W}$ to $1.4\times10^{-8}\mathrm{m}^2\mathrm{K/W}$. Theoretical calculations using the diffuse mismatch model and two-temperature models show a similar trend with experimental data, indicating that the Ni layer significantly reduces both resistances due to phonon mismatch and electron-phonon non-equilibrium.

5. ABSENCE OF COUPLED THERMAL INTERFACES IN AL2O3/NI/AL2O3 SANDWICH STRUCTURE

A version of the chapter is published as [115].

5.1 Introduction

As the thickness of thin films in integrated circuits decreases, the interfacial resistance between metals and dielectric components [22] ($\sim 10^{-2}\mathrm{mm}^2\mathrm{K/W}$) becomes comparable to or even larger than the thermal resistance of thin films ($\sim$10nm). Due to different main carriers of thermal energy in dielectric and metals, electron-phonon non-equailibrium occurs near interfaces. However, it has been shown that when the metal layer thickness decreases to be comparable to phonon mean free path, phonons can transport through the metal layer [29] while electrons do not participate much in thermal transport. Furthermore, in nanostructures with higher interface density and minimal lattice mismatch, coherent phonons are also found to decrease the total thermal resistance [38,40,116,117]. Similarly, cooling length is also studied as the length where electrons and phonons reach equilibrium for metal-dielectric interfaces [36]. For a sandwich structure with metal layer in the middle, the metal layer is responsible for electron-phonon coupling of two interfaces. A shorter metal thickness than cooling length also interferes with electron-phonon coupling effect. Both findings indicate that interfaces are no longer isolated but dependent on the thickness of the thin film that separates them. First finding is studied in both theoretically and experimentally. The second one, however, needs more work.

In this work, we use the differential 3ω method to measure the interfacial resistance of a thin nickel layer sandwiched between two aluminum oxide layers, with the nickel layer thickness varying from 10nm, 15nm to 30nm. The temperature dependence of the interfacial resistance is also studied. The two temperature model and diffuse mismatch model are

used to calculate the theoretical interfacial resistance, which agrees reasonably well with experimental values. Overall thermal resistance is dominant by phonon mismatch resistance. Since phonon mismatch resistance does not vary even when metal layer thickness decreases around cooling length, the two adjacent interfaces in our sandwich structures are not thermally coupled even as nickel layer falls below electron cooling length.

5.2 Sample Fabrication

We have fabricated two sandwich structures in this work to measure the interfacial resistance between nickel and aluminum oxide, illustrated in Fig. 5.1. Schematic views are shown along with TEM images (Transmission Electron Microscope). Before film depositions, silicon wafers were cleaned using the RCA method (the Radio Corporation of America), and any residues or silicon oxide layer on the surface were removed by dipping in HF (Hydrogen Fluoride). Both aluminum oxide and nickel layers are deposited using atomic layer deposition (ALD) to ensure smooth interfaces and consistent thickness. On sample A, the reference sample, a 40nm aluminum oxide layer is deposited on silicon substrate. For sandwich structures with the Ni layer, a 20nm aluminum oxide layer is deposited followed by a thin layer of nickel, then another 20nm aluminum oxide layer. The aluminum oxide layer is deposited at 250C with a rate of 0.12nm/cycle, and the nickel layer at 250C with a rate of 0.2A/cycle with thickness varying from 10nm, 15nm, to 30nm. A layer of Pt is deposited on the structures during FIB (Focused Ion Beam) lift-off, only for TEM images.

5.3 Thermal Interfacial Resistance Characterization

For thin film and interfacial resistance measurement, time-domain thermoreflectance (TDTR) method [28] and differential 3ω method [25–27] are widely applied. Both methods yield reliable results [118]. The formal one shines a pulsed heating laser as well as a weaker probe laser on metal surface. By monitoring the transient thermal response of these ultra short pulses, interfacial resistance is obtained. Differential 3ω method measures total thermal resistance difference between thin film sample and reference sample to get

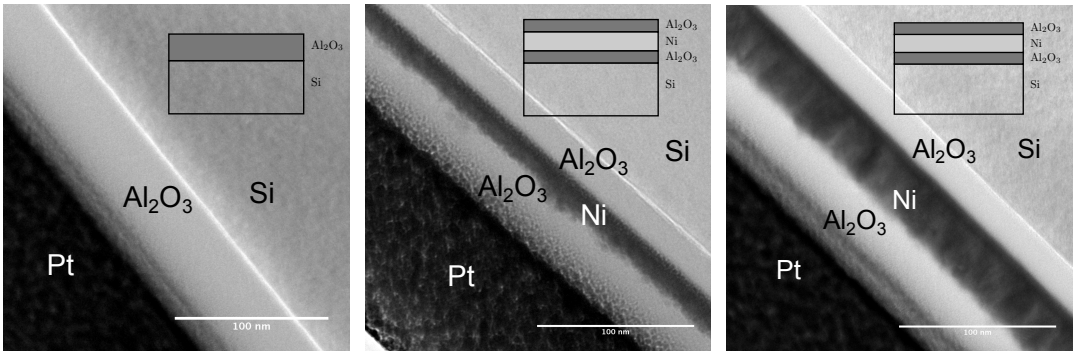

(a) Sample A (b) Sample B (c) Sample C

Figure 5.1. : Sandwich Structures for Thermal Interfacial Resistance Measurement

interfacial resistance. However, temperature control of TDTR is more difficult compared to 3ω method, as pulsed heating laser has the tendency to excite electrons in surface metal film rapidly.

In this work, we apply the differential 3ω method. Ti/Au metal line of 3mm long and 30μm wide is later patterned with photolithography for the 3ω measurement. An AC current of frequency ω is applied to the metal line, resulting in a temperature oscillation amplitude ΔT, and a voltage of 3ω frequency. Three lock-in amplifiers are utilized to monitor metal line $v_{1\omega}$, $v_{3\omega}$, and power consumption p. For a bulk sample, ΔT can be expressed as

$$\Delta T = \frac{2v_{3\omega}}{v_{1\omega}C_{rt}} = \frac{p}{\pi k}\int_0^\infty \frac{sin^2(\lambda b)}{(\lambda b)^2(\lambda^2 + 2i\omega/D)^{1/2}}d\lambda, \tag{5.1}$$

where p is the power consumption across the metal line, k, D are the thermal conductivity and thermal diffusivity of the sample, b is half width of metal line, and $v_{1\omega}$ and $v_{3\omega}$ are the voltage across the metal line with frequency ω and 3ω respectively. In this work, the samples A and B are measured separately, leading to different temperature oscillations and total thermal resistance difference ΔR [27] as

$$\begin{aligned} \Delta R &= 2bl(\left(\frac{\Delta T}{p}\right)_B - \left(\frac{\Delta T}{p}\right)_A) \\ &= R_{Ni} + 2R_i \approx 2R_i \end{aligned} \tag{5.2}$$

where R_i stands for interfacial resistance between nickel and alumina, which is about half of the total thermal resistance difference measured by 3ω method. Uncertainties are evaluated as $(\Delta T/p)_{R+F} - (\Delta T/p)_R$ at different frequencies are collected regarding to Eqn. 5.2, which produce most uncertainties. Uncertainties are valued in a similar fashion for thickness-dependent and temperature dependent thermal conductivity.

To study the potential interface coupling effect when the thickness of the middle metal thin film is comparable to twice the electron-phonon cooling length, the interfacial resistance is measured as a function of different nickel layer thickness. When the metal layer is thinner than or comparable to phonon mean free path, long-wavelength coherent phonons will travel ballistically through two interfaces as one coupled interface, rather than experience two interfaces separately, resulting in lower overall thermal resistance [38]. This is how interfaces become coupled due to ballistic transfer of phonons. If the nickel film is much thicker than most of the phonons' mean free path, most phonons will travel across two interfaces separately. Cooling length stands for electron-phonon non-equilibrium distance [36] . As the metal layer connects two metal-dielectric interfaces, electron-phonon coupling is affected once metal layer is thinner than twice the cooling length, resulting in thickness-dependent interfacial resistance. Considering the mean free path for nickel is around 5nm and cooling length around 15nm, the nickel layer thickness is chosen as 10nm, 15nm, and 30nm, and interfacial resistance is $6.7 \pm 0.6{\times}10^{-3}\mathrm{mm^2K/W}$, $6.7 \pm 0.8{\times}10^{-3}\mathrm{mm^2K/W}$, $7.0 \pm 0.7{\times}10^{-3}\mathrm{mm^2K/W}$ respectively. Results from the 3ω measurement shown in Fig. 5.2 and Tab. 5.1 indicate the thickness dependence of the interfacial resistance is negligible, thus the two interfaces in our system are not coupled.

Table 5.1. : Interfaical Resistance with Different Ni Thickness

Ni Thickness (nm)	Interfacial Resistance ($\times 10^{-3}\mathrm{mm^2K/W}$)
10nm	6.7±0.6
15nm	6.7±0.8
30nm	7.0±0.7

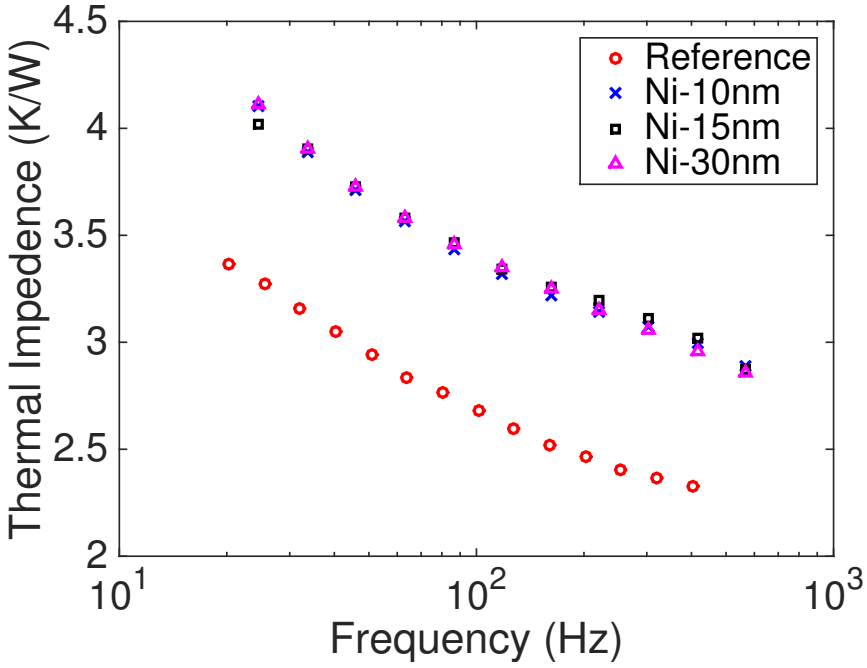

Figure 5.2. : Differential 3ω Method on Thickness Dependence Characterizations of Thermal Interfacial Resistance

Temperature dependence of the interfacial resistance is taken using liquid nitrogen to provide temperature as low as 130K. The result is shown in Fig. 5.3, indicating that the interfacial resistance does not depend much on temperature changes either.

5.4 Theoretical Estimation on Interfacial Resistance

Two temperature model is applied here for Ni-alumina interfaces. The overall interfacial resistance consists of a phonon-phonon scattering resistance $\mathrm{R_{pp}}$, an electron-phonon coupling component $\mathrm{R_{ep}}$, electrical inelastic scattering resistance $\mathrm{R_{ei}}$, phonon transport channel inside the metal layer $\mathrm{R_p}$, as shown in Fig.5.4 [37]. The last one is added to include the ballistic transfer of phonons through nickel layer. $\mathrm{R_{pp}}$ is the thermal interface resistance when phonons travel across the interface. Compared to phonons in nickel film, electrons are more efficient in heat transfer, thus most energy is transferred to nickel elec-

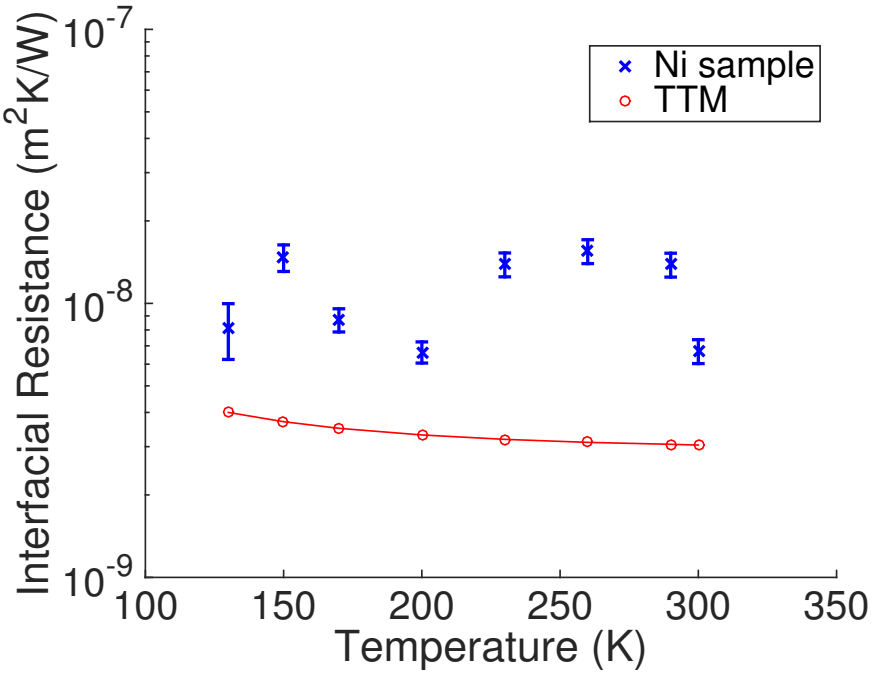

Figure 5.3. : Temperature Dependence of the Thermal Interfacial Resistance, Compared with TTM Results

trons through electron-phonon coupling component $\mathrm{R_{ep}}$. $\mathrm{R_e}$ is the thermal resistance for nickel electrons. For thermal energy remained in nickel phonons, $\mathrm{R_p}$ is the thermal resistance for phonons across the nickel film. On the other hand, $\mathrm{R_{ei}}$ stands for the process where electrons in alumina transfer energy directly to nickel electrons without participations of any phonons. Because of the low density of electrons in aluminum oxide, $\mathrm{R_{ei}}$ is neglected in this work.

Similar to the analysis in previous work in nickel-alumina interface, R_{pp} and R_{ep} can be calculated as in Eqn. 5.5 and 5.4 respectively. From these two equations we are able to calculate thermal interface resistance based on DMM with phonon dispersions, known by lattice dynamics, shown in Fig. 5.5.

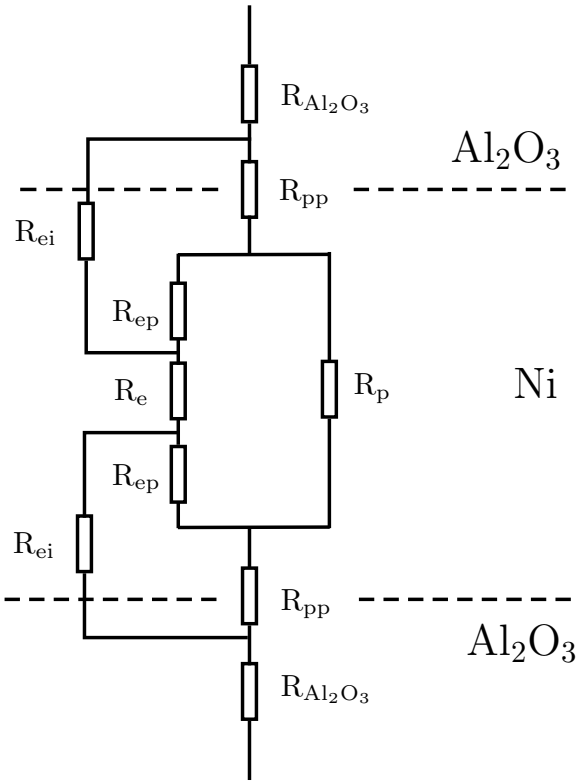

Figure 5.4. : Thermal Resistance Network Between Nickel and Aluminum Oxide

$$\alpha_{A\to B}(\omega') = \frac{\sum_j DOS_{B,j}(\omega)v_{B,j}(\omega)\delta_{\omega',\omega}}{\sum_j DOS_{A,j}(\omega)v_{A,j}(\omega)\delta_{\omega',\omega} + \sum_j DOS_{B,j}(\omega)v_{B,j}(\omega)\delta_{\omega',\omega}} \quad (5.3)$$

$$h_{A\to B} = \frac{1}{4}\sum_j \int \hbar\omega DOS_{A,j}v_{A,j}\alpha_{A\to B}\frac{\partial f}{\partial T}d\omega, \quad (5.4)$$

$$R_{ep} = (\frac{k_e}{k_e + k_p})^{3/2}(\frac{1}{G_{ep}k_p})^{1/2}. \quad (5.5)$$

Direct phonon transfer within nickel layer $\mathrm{R_p}$ can be approximated as d/k_p, where d is the thickness of nickel layer. For nickel [119], k_p is 5.5W/mK for 10nm film, 6.4W/mK for 15nm film, 8.9W/mK for 30nm film, 18W/mK for bulk nickel. On the other hand, k_e remains around 40 to 60W/mK for 10nm to 30nm nickel films [120]. The total thermal interfacial resistance $\mathrm{R_i}$ is calculated as

$$R_i = R_{pp} + R_{ep}//\frac{R_p}{2} = R_{pp} + \frac{R_pR_{ep}}{R_p + 2R_{ep}}. \quad (5.6)$$

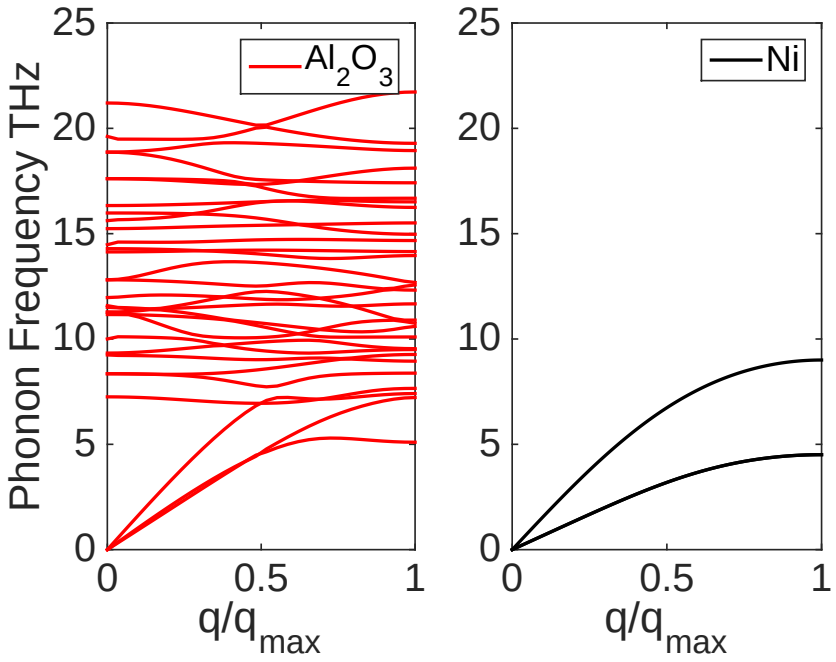

Figure 5.5. : Detailed Phonon Dispersion of Aluminum Oxide and Nickel

The theoretical values together with the experimental values are listed in Tab. 5.2. First, phonon transmission resistance component dominates the overall thermal interfacial resistance due to highly lattice mismatch between nickel and aluminum oxide. On the other hand, $\mathrm{R_p}$ decreases with decreasing metal layer thickness, while $\mathrm{R_{ep}}$ increases. The combination of $\mathrm{R_p}$ and $\mathrm{R_{ep}}$ indicates a possible highest resistance between 10nm and 30nm nickel layer. However, it is still much smaller and less important than phonon mismatch resistance to have a high impact. Compared to nickel-alumina interfacial resistance fabricated with metal evaporation, $14.0\mathrm{mm^2K/W}$, atomic layer deposition provides nickel layer and interfaces of better quality as well as low thermal interfacial resistance.

With temperature changing from 300K to 130K, the electron-phonon coupling coefficient G_{ep} decreases from $2.88\times10^{17}\mathrm{Wm^{-3}K^{-1}}$ at 300K to $5.62\times10^{17}\mathrm{Wm^{-3}K^{-1}}$ at 130K. However, interfacial resistance barely changes, both theoretically and in experiments. Since the Debye temperature of nickel is relatively low at 450K, and aluminum oxide at 873K, the temperature range of 130K to 300K is not sufficient to observe temperature dependent

Table 5.2. : Interfaical Resistance with Different Ni Thickness, Compared with Theoretical Estimation

Ni Layer	$\mathrm{R_p}/2$	$\mathrm{R_{ep}}$	$\mathrm{R_{ep}}//\frac{\mathrm{R_p}}{2}$	$\mathrm{R_{pp}}$	$\mathrm{R_{i,theo}}$	$\mathrm{R_{i,exp}}$
10nm	0.91*	0.79	0.42	3.04	3.46	6.7
15nm	1.67	0.74	0.51	3.04	3.55	6.7
30nm	1.69	0.63	0.46	3.04	3.50	7.0

* Interfacial resistance unit as $10^{-3}\mathrm{mm^2W/K}$

phonon transmission resistance. Thus, as the dominant phonon mismatch resistance is not sensitive to temperature, the overall estimated interface resistance remains almost constant even G_{ep} changes significantly.

5.5 Conclusion

In conclusion, we fabricated sandwich structures of nickel and $\mathrm{Al_2O_3}$, and used the differential 3ω method to measure interfacial thermal resistance. Theoretical estimation is also made with two temperature model along with detailed DMM. The overall interfacial resistance from experiments agrees reasonably well with theoretical prediction. Phonon mismatch is still the dominating mechanism for the interfaces between nickel and aluminum oxide. And interfaces remain independent even when the thickness of metal layer decreases to electron-phonon cooling length.

6. ULTRA-EFFICIENT LOW-COST RADIATIVE COOLING PAINTS

6.1 Introduction

Cooling consumes a great portion of energy in both residential and commercial applications [121]. The performance and reliability of outdoor equipment exposed to direct sunlight also deteriorates due to overheating. Passive radiative cooling can help reduce cooling cost as well as maintain a low temperature for outdoor equipment during daytime without any energy consumption. Exposed surfaces can emit power through a transparent spectral window of the atmosphere, from $8\,\mu\mathrm{m}$ to $13\,\mu\mathrm{m}$ (the sky window) directly to the deep sky, which functions as an infinite heat sink with a temperature of 3K. The net cooling power of the surface is the thermal emission from the surface in the sky window, subtracting the absorbed solar irradiation, energy exchange with the atmosphere as well as the conduction and convection thermal loads. If the surface reflects most of the solar irradiation while maintaining a high emissivity in the sky window, the surface can be cooled below the ambient temperature under direct sunlight.

There have been decades of efforts to create paints with radiative cooling capability under direct sunlight [41–52]. TiO_2 particles are the most common pigments used in these studies as well as commercial paints. The particle size is usually in hundreds of nanometers to several microns, based on the fact that as the diameter of particles gets comparable to solar irradiation wavelength, light can be strongly scattered and reflected [122, 123]. A dual-layer structure was proposed for daytime passive radiative cooling, with titanium dioxide-polymer nanocomposite on top of a carbon black layer [50]. A single-layer paint using SiO_2 particle film was also developed and tested [52]. However, to date no paints have demonstrated cooling below the ambient under direct sunlight. One study put a thin layer of white paint on aluminum and showed cooling below the ambient during a winter day, but the high solar reflectance was from the aluminum film rather than the paints [42].

On the other hand, 24-hour passive refrigeration has been demonstrated in non-paint materials recently. A multi-layer photonic structure was fabricated to achieve 5°C cooler than ambient temperature under direct sunlight [54]. Gentle demonstrated full daytime cooling with a design with polyesters with a silver layer [124]. Another scalable approach involved silica-TPX nanocomposite with silver backing, which managed to provide $93\mathrm{W}/\mathrm{m}^2$ cooling power continuously throughout 24 hours [55]. Another design of three layers of PDMS, silica and silver maintained more than 8°C lower than ambient temperature under direct solar irradiation [56]. These non-paint radiative cooling materials are either expensive or relying on a metal layer for solar reflection which could undesirably interfere with electromagnetic waves in many applications [57, 58]. Most recently, below-ambient cooling was demonstrated in porous poly(vinylidene fluoride-co-hexafluoropropene) which is close to (but still not exactly) the paint form [59], while the layer needs to be thicker than $400\,\mu\mathrm{m}$ to be effective, and the material is five times as expensive as acrylic used in commercial paints [60]. Nevertheless, it is still a pertinent task to develop radiative cooling paints that are high-performance, low-cost, and compatible with commercial paint fabrication process.

6.2 Sample Fabrication

In this work, three samples along with carbon black and commercial paint control samples were fabricated. For the carbon black control sample, carbon black paint was spray coated on a glass substrate and dried in well-vented area overnight. The TiO_2-acrylic paint consists of 500nm TiO_2 nanoparticles from US Research Nanomaterials in acrylic matrix with 8% concentration. The nanoparticles were mixed with butanone first, followed by 10-minute sonication to reduce particle agglomeration. We used Elvacite 2028 from Lucite International as the acrylic matrix due to its low viscosity. The acrylic was then slowly added to the mixture to dissolve. The mixture was later degassed in vacuum chamber to remove air bubbles introduced during the mixing and ultrasonication. After pouring into a mold, the mixture was dried overnight till all solvent was gone. The free-standing finishing coating was released from the mold with a thickness around $400\,\mu\mathrm{m}$. The 60% volume

concentration $CaCO_3$-acrylic paint contains $1.9\,\mu m$ $CaCO_3$ fillers, fabricated in a similar fashion with the TiO_2-acrylic paint. The thickness of the free-standing sample is around $400\,\mu m$. $150\,\mu m$ thin layer of $BaSO_4$ particle film was fabricated on silicon substrate. A mixture of 500nm $BaSO_4$ particles, DI water and ethanol was mixed and coated on the substrate until fully dried.

6.3 Experiment Setup

Two onsite cooling setups were made to characterize the cooling performance of the paints on the roof of a high-rise building, as shown in Fig. 6.1. For the first setup in Fig. S6.1(a), a cavity was made from a block of white styrofoam, providing excellent insulation from conduction. A thin layer of low-density polyethylene film was used as a shield from forced convection. T-type thermal couples were attached to the base of the sample for temperature measurement and outside the foam for the ambient temperature. A pyranometer was secured for solar irradiation measurement. The temperature data and solar irradiance were collected by a datalogger. The second setup in Fig. S6.1(b) includes a feedback heater to synchronize the sample temperature with the ambient temperature. As the sample was heated to the ambient temperature, the power consumption of the heater was recorded as the cooling power. Both of the setups were covered by silver mylar to reflect solar irradiation. These two actual onsite cooling setups are shown in Fig. 6.2.

6.4 Results and Discussion

Here, we show that with the right fillers, we can achieve below-ambient cooling in paints under direct sunlight, and with ultra-high efficiency and low cost. The samples were fabricated as shown in Fig. 6.3(a) and Table 6.1. First we attempted to see whether below-ambient cooling can be achieved in the conventional titanium dioxide-acrylic paint by optimizing the particle size to enhance the solar reflection. We selected an average particle size of 500nm to ensure high reflectance in both the visible and near infrared range of the solar irradiation [50]. The acrylic matrix is transparent in the visible range, also pro-

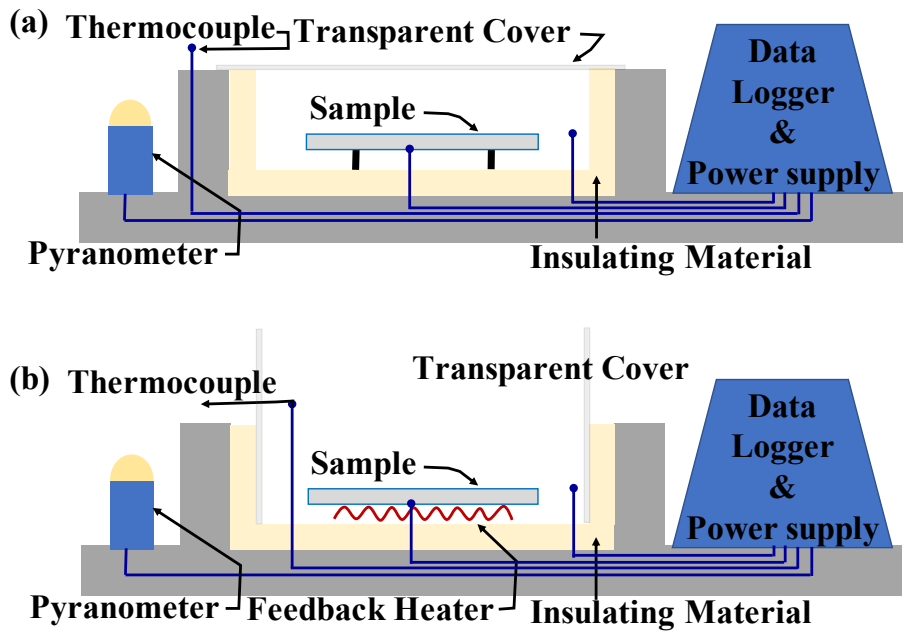

Figure 6.1. : Onsite cooling setups for cooling performance characterizations: (a) The temperatures of the sample and the ambient are recorded. A lower sample temperature than the ambient indicates below-ambient cooling. (b) The sample is maintained at the same temperature as the ambient using a feedback heater. The power consumption of the heater represents the cooling power.

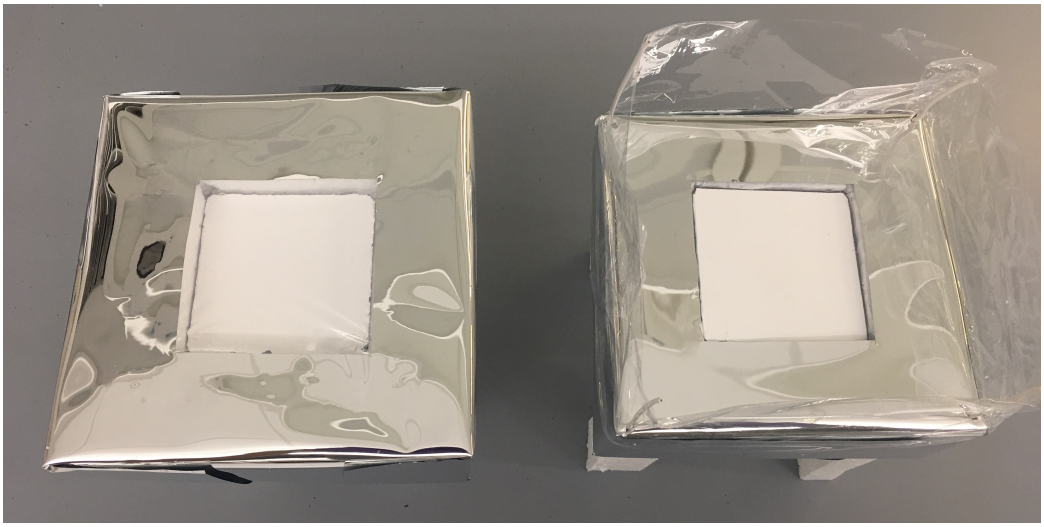

Figure 6.2. : Actual onsite cooling characterization setups are shown here. Left is the setup without a feedback heater, and right is the one for direct cooling power measurement.

Table 6.1. : Sample list for passive radiation cooling paints

Sample	Component
A	TiO_2-acrylic paint
B	$CaCO_3$-acrylic paint
C	$BaSO_4$ film

vides high emissivity in the sky window as TiO_2 lacks optical phonon resonance peaks in the mid-infrared range. A mixture of butanone, acrylic and particle fillers is left fully dried before released from a mold, resulting in a free-standing paint layer. UV-VIS-NIR and FTIR spectrometers with integrating spheres are used for reflectance and emissivity measurement from 250nm to $20\,\mu m$. The solar reflectance is mainly contributed by fillers, and the sky-window emission can come from both matrix and fillers, as shown in Fig. 6.4(a). The emissivity of a 8% volume concentration TiO_2-acrylic paint is shown in Fig. 6.4(b). The TiO_2 paint shows high emissivity of 0.93 in the sky window. The solar reflectance is 89.5$\pm$0.5%, which is only moderately higher than commercial paints. The electron band gap of TiO_2 sits around 3.2eV, resulting in strong absorptivity of 88% in the ultra-violet (UV) range. The reflectance is 94.7% in the visible (VIS) band and 91.6% in near infrared (NIR) range though. The uncertainty is valued based on results of five different samples made in separated batches.

An outdoor temperature measurement was conducted with Sample A (TiO_2 paint) and carbon black sample over a three-day period in West Lafayette, IN on October 16, 2017, as shown in Fig. 6.5(a). The peak solar irradiation was around $800 W/m^2$ at about 2PM of the days. During the night, both samples showed nighttime cooling approximately 7°C below ambient temperature due to their high emissivity in the sky window. The TiO_2-acrylic paints showed partial daytime cooling below ambient temperature except from 11:20am to 4pm when the solar irradiation became higher than $600 W/m^2$. In another onsite experiment in West Lafayette, IN on April 25, 2018, a feedback heater was used, to match the temperature of Sample A to the ambient; therefore directly measuring the cooling power in

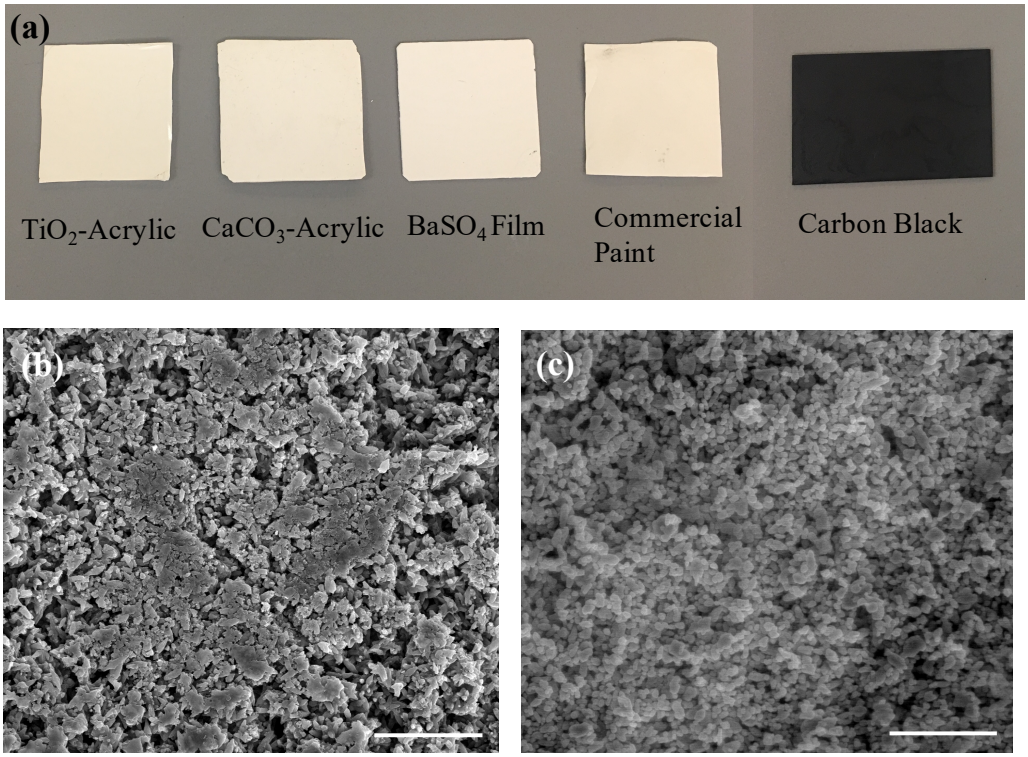

Figure 6.3. : (a) Our radiative cooling paints samples along with carbon black and commercial paint as control samples, (b) an SEM image of the $\mathrm{CaCO_3}$-acrylic paint, (c) an SEM image of the $\mathrm{BaSO_4}$ film. Both scale bars in (b) and (c) are $10\,\mu\mathrm{m}$.

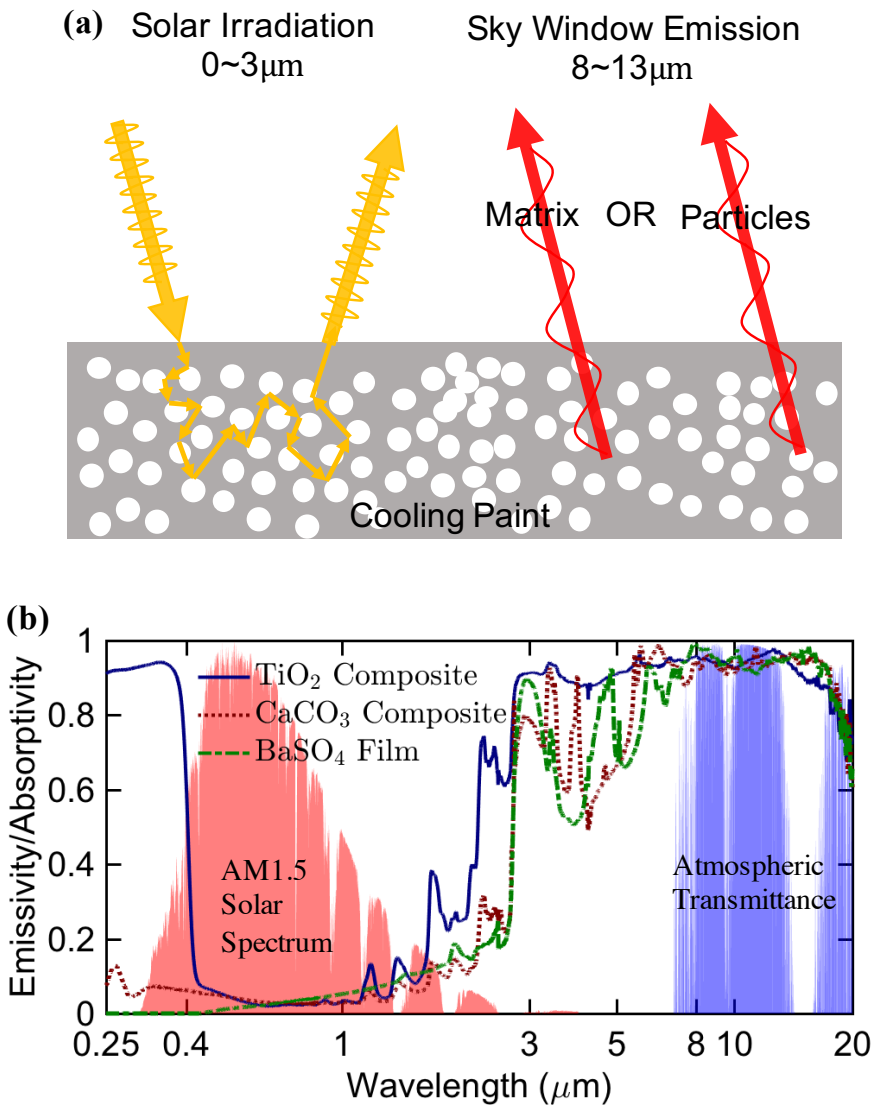

Figure 6.4. : (a) For cooling paint exposed to direct solar irradiation, the fillers are engineered to maximize solar reflection below $3\,\mu\mathrm{m}$, and the particles or polymer matrix contributes to high emissivity in the sky window between $8\,\mu\mathrm{m}$ and $13\,\mu\mathrm{m}$. (b) The emissivity of different radiative cooling paints is characterized from 0.25 to $20\,\mu\mathrm{m}$.

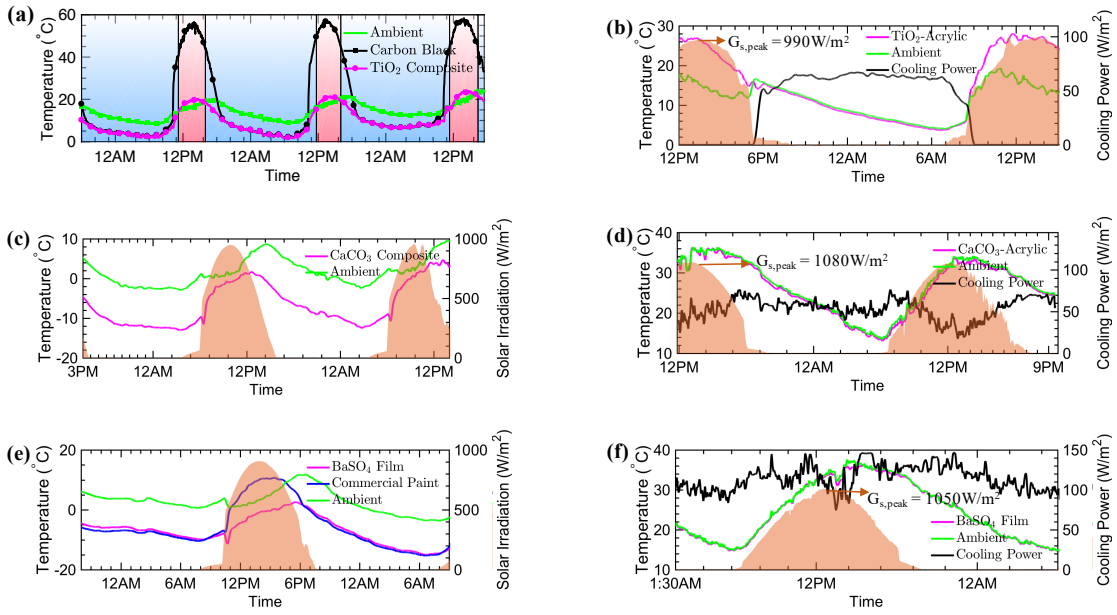

Figure 6.5. : (a)(c)(e) are outdoor temperature measurements for the TiO_2-acrylic paint, $CaCO_3$-acrylic paint and $BaSO_4$ film respectively over periods of more than one day. (b)(d)(f) are direct measurements of the cooling power for the TiO_2-acrylic paint, $CaCO_3$-acrylic paint and $BaSO_4$ film using a feedback heater. The orange regions stand for solar irradiation intensity.

Fig. 6.5(b). The shade represents the solar irradiation, and the black curve representing the cooling power of Sample A shows net radiative cooling power around $63\mathrm{W/m^2}$ during the nights.

We attribute the inability to achieve below-ambient cooling under direct sunlight in the $\mathrm{TiO_2}$-acrylic paint to the 3.2eV electron bandgap of $\mathrm{TiO_2}$ which causes high solar absorption in the UV range. Hence we have searched many alternative materials with higher electron bandgaps, and achieved excellent results in $\mathrm{CaCO_3}$, and $\mathrm{BaSO_4}$, both with $>$5eV bandgaps. Similar to $\mathrm{TiO_2}$, $\mathrm{CaCO_3}$ does not have phonon-polariton resonances in the sky window, therefore a matrix that emits in the sky window, such as acrylic, is essential to provide the cooling power. $\mathrm{BaSO_4}$, on the other hand, has intrinsic emission peaks in the sky window, thus engineering the particle size can allow a single layer of $\mathrm{BaSO_4}$ particle film to function both as a sky window emitter and a solar reflector. These samples are fabricated as Sample B and C using $\mathrm{CaCO_3}$ and $\mathrm{BaSO_4}$ respectively, listed in Table 6.1.

Sample B is $\mathrm{CaCO_3}$-acrylic paint layer with 60% volume concentration of $1.9\,\mu\mathrm{m}$ $\mathrm{CaCO_3}$ fillers, made with a same process with Sample A. The thickness of the sample is around $400\,\mu\mathrm{m}$. The SEM images of the sample surface are shown in Fig. 6.3(b). Its emissivity is shown in Fig. 6.4(b). While maintaining a similarly high emissivity in the sky window with the $\mathrm{TiO_2}$-acrylic paint, its absorptivity in the UV and NIR regions are much lower. The solar reflectance reaches 95.5%, thanks to the high particle concentration. Thinner films with thicknesses of 98, 131, and $177\,\mu\mathrm{m}$ still provide high solar reflectances of 88.9%, 93.4%, 95.1% respectively. Outdoor temperature measurement of Sample B in West Lafayette, IN on March 21, 2018, shows full daytime cooling in Fig. 6.5(c), where the sample stays 10^oC below the ambient temperature at night, and at least 1.7^oC below the ambient temperature at a peak solar irradiation around $950\mathrm{W/m^2}$. Feedback heater experiments in Fig. 6.5(d) show an average cooling power of $56\mathrm{W/m^2}$ during nights and $37\mathrm{W/m^2}$ around noon (between 10am and 2pm) in Reno, NV on August 1, 2018.

Sample C is a $\mathrm{BaSO_4}$ particle film of $150\,\mu\mathrm{m}$ thickness on a silicon wafer. The SEM image is shown in Fig. 6.3(c). $\mathrm{BaSO_4}$ has phonon polariton resonance at $9\,\mu\mathrm{m}$ which provides absorption peaks in the sky window. Hence, it does not need the acrylic matrix to

emit in the sky window. The average particle size is chosen as 500nm to reflect both visible and near infrared range of the solar irradiation. It reaches a solar reflectance of 97.6% and an emissivity of 0.93 in the sky window, as shown in Fig. 6.4(b). The paint achieves full daytime cooling below the ambient temperature with a peak solar irradiation of 900$\mathrm{W/m^2}$ in West Lafayette, IN on March 14, 2018, as shown in Fig. 6.5(e) along with a control commercial white paint (Sherwin-Williams SW 7757). The temperature of the sample drops 10.5^{o}C below the ambient temperature during the nights, and stays 4.5^{o}C below ambient even at the peak solar irradiation, whereas the commercial paint rises 6.8^{o}C above the ambient temperature. The silicon substrate is intended only as a supporting substrate for Sample C, not to enhance solar reflectance, nor does it emit in the sky window. We tested the $\mathrm{BaSO_4}$ film also on glass and aluminum substrates, and the cooling performance remains similar. More information is available in the Supplementary Material. In Fig. 6.5(f), a direct measurement of the cooling power of Sample C in Reno, NV on July 28, 2018 shows that the cooling power reaches an average of 117$\mathrm{W/m^2}$ over a 24-hour period. Counterintuitively, the cooling power between 10am to 2pm, despite the solar absorption, is similar to that from 8pm to 6am, both above 110$\mathrm{W/m^2}$. This is due to the fact the radiative cooling power is proportional to the fourth power of the surface temperature. As the ambient temperature rises to 35°C at noon, the radiative thermal emission increases by 30% compared with that at 15°C at midnight. Combining a high reflection in the solar spectrum, our $\mathrm{BaSO_4}$ paint can maintain a constant high cooling power regardless of the solar irradiation. The cooling performance is close or even higher than the designs with metallic layers [55].

Above ambient cooling tests are also conducted at West Lafayette, IN to compare the cooling performance difference between our $\mathrm{BaSO_4}$ paint and commercial white paint. In the first testing when both samples are heated up by 120 $\mathrm{W/m^2}$ under direct sunlight, in Fig. 6.6(a). Though they reach similar temperature during the nights, $\mathrm{BaSO_4}$ paint shows 7^{o}C lower temperature than the commercial white paint around noon when solar irradiation is around 1000 $\mathrm{W/m^2}$ since it offers 11% more solar reflectance than the commercial white paint. The temperature difference occurs around noon when air conditioning or cooling is

needed the most, and 7^{o}C is a significant portion of the cooling requirement for residential and commercial buildings or warehouses. There are other scenarios when the maximum heating load is of the most interest before the surface reaches a targeted temperature. Other two onside testings are to demonstrate how much more heat load $\mathrm{BaSO_4}$ paint can offer under the same temperature. The white paint is exposed to the ambient air without any additional heat load from the heater, while $\mathrm{BaSO_4}$ paint is heated to the same temperature as the commercial white paint. The heater power added to the $\mathrm{BaSO_4}$ paint is the amount of additional heat load under interest, maximized at 83 $\mathrm{W/m^2}$ at noon, shown in Fig. 6.6(b) along with solar irradiation intensity represented as orange regions. Solar absorption difference between two paints fits well with the additional heater power for the $\mathrm{BaSO_4}$ paint, indicating the heat load difference that the $\mathrm{BaSO_4}$ paint offers comes from the higher solar reflectance alone. A similar test is done with the commercial white paint heated by 50 $\mathrm{W/m^2}$ from the heater, shown in Fig. 6.6(c). The $\mathrm{BaSO_4}$ paint offers additional 85 $\mathrm{W/m^2}$ compared to the commercial paint at noon, which is contributed from the solar reflectance difference. Overall, our cooling paints are able to offer a substantial cooling savings when replacing the commercial white paint.

Thickness-Dependence of the Cooling Paints

The $\mathrm{TiO_2}$-acrylic and $\mathrm{CaCO_3}$-acrylic paint samples with $400\,\mu\mathrm{m}$ thickness were reported in the main report, where the thickness is sufficient to make the cooling performance independent on substrates. However, the thickness of commercial exterior paints is usually below $150\,\mu\mathrm{m}$ when applied. Here we study the impact of thinner samples. Figure 6.7 compiles the solar reflectance results for 8% $\mathrm{TiO_2}$-acrylic paints with the thickness ranging from $30\,\mu\mathrm{m}$ to $107\,\mu\mathrm{m}$. The thin films were deposited on polyethylene terephthalate (PET) film using a film applicator to control the wet film thickness. The dry film thickness was measured with a coordinate measuring machine (Brown&Sharp MicroXcel PFX). The uncertainties of the thickness are calculated based on the thicknesses measured at various spots of the samples. In the UV spectrum, the thin films of $\mathrm{TiO_2}$-acrylic paints share simi-

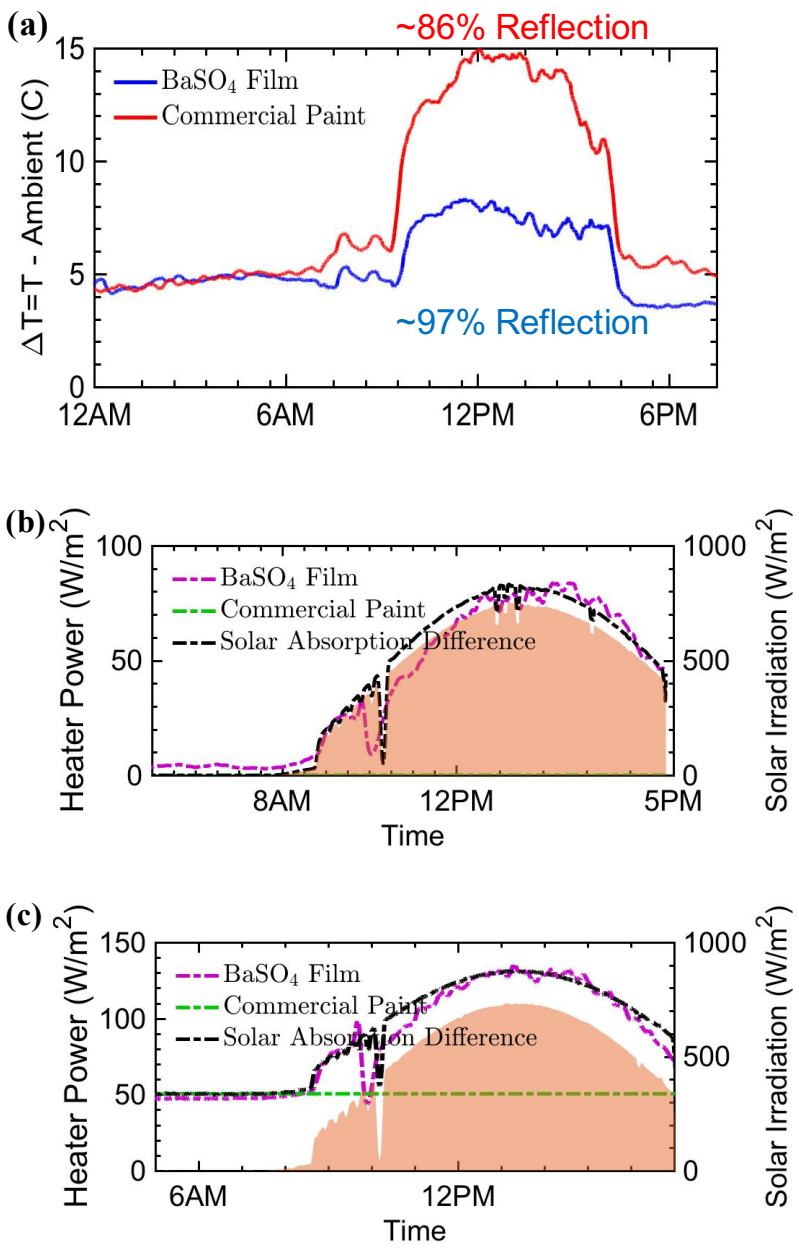

Figure 6.6. : (a) Above ambient cooling test is conducted with a constant heating power from the heaters. (b)(c) Additional cooling power that the $BaSO_4$ paint offers is measured by synchronizing the temperatures of the $BaSO_4$ paint and the commercial white paint.

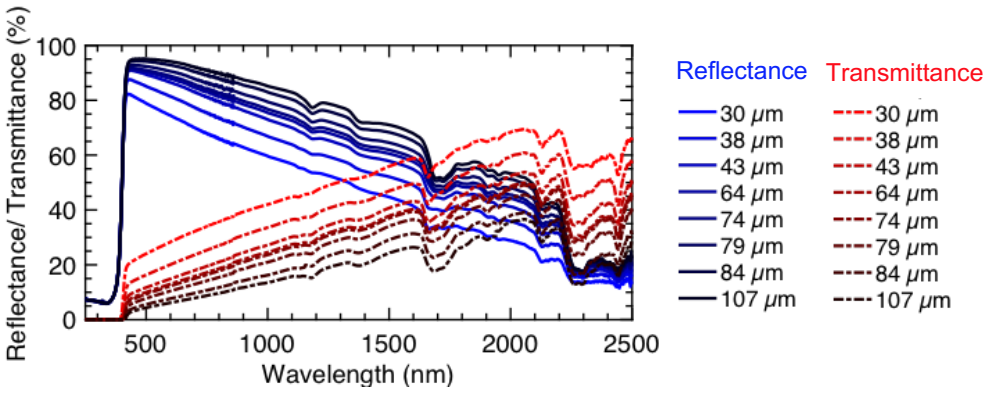

Figure 6.7. : The spectral reflectance and transmittance of thin coatings of 8% TiO_2-acrylic paint to solar irradiation, at a series of thicknesses

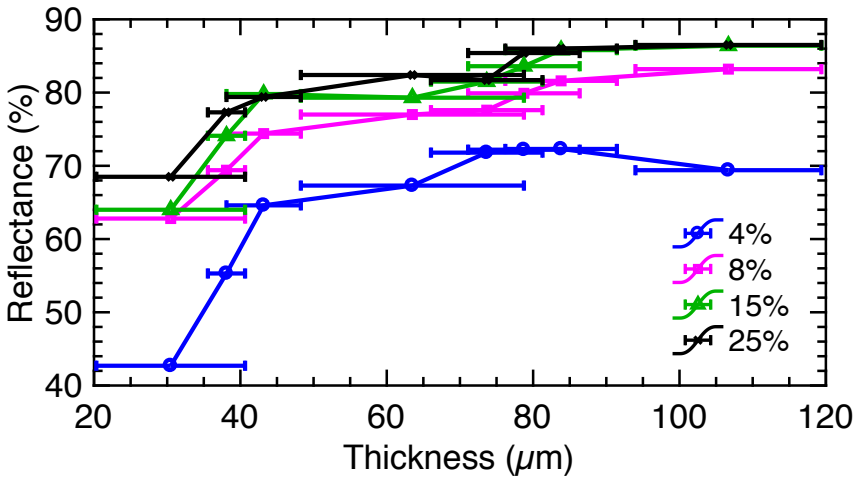

Figure 6.8. : The total solar reflectance of the TiO_2-acrylic paint layer as a function of the thickness and volume concentration

lar absorptance due to the bandgap of TiO_2 at 3.2eV. The optical thickness increases with the paint layer thickness, leading to higher reflectance and lower transmittance. Measurements were repeated for the thin coatings of 4%, 15% and 25% concentrations, shown in Fig. 6.8. With a target reflectance, increasing the filler concentration decreases the layer thickness.

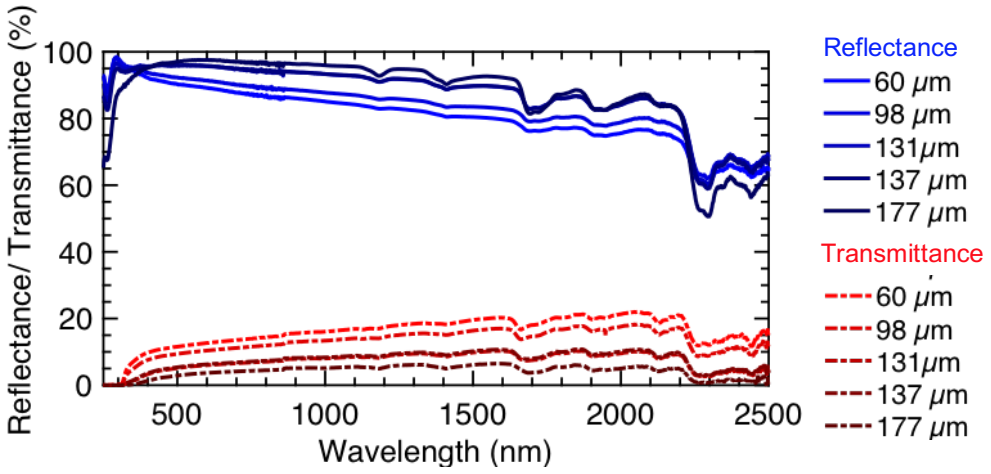

Figure 6.9. : Solar reflectance measurement of 60% $CaCO_3$-acrylic paints with different thin film thicknesses

The $CaCO_3$-acrylic paint with 60% concentration and different thicknesses were fabricated similarly with thin TiO_2 paint layers. The spectral solar reflectance and transmittance are shown in Fig. 6.9. Compared to the solar reflectance of 95.5% with $400\,\mu m$ thickness, thinner layers of $98\,\mu m$, $131\,\mu m$, $177\,\mu m$ show solar reflectance around 88.9%, 93.4% and 95.1% respectively.

Thin films of $BaSO_4$ were fabricated on different substrates along with standalone films. The solar reflectance is independent of the substrate materials, indicating a high opacity of the $BaSO_4$ film in the solar spectrum. We also prepared $BaSO_4$ particle films on non-emitting Al foil and glass substrates. Both samples show similar cooling performance during the night similar to the carbon black sample, among which the differences are within the limits of error for type T thermocouples, as shown in Fig. 6.11. Thus, both the cooling power and the solar reflectance are contributed by the $BaSO_4$ film alone.

Cost Analysis For Cooling Paints

Due to the wide availability of $CaCO_3$ and $BaSO_4$ in natural minerals, the cost of our radiative cooling paints can be comparable to or even less than commercial white paints.

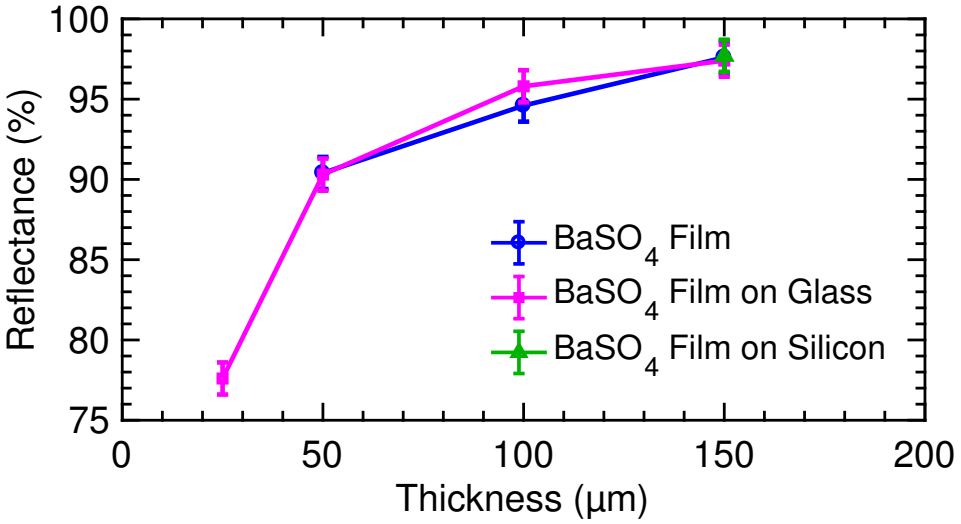

Figure 6.10. : Solar reflectance measurements of the $BaSO_4$ films with different thicknesses and different substrates.

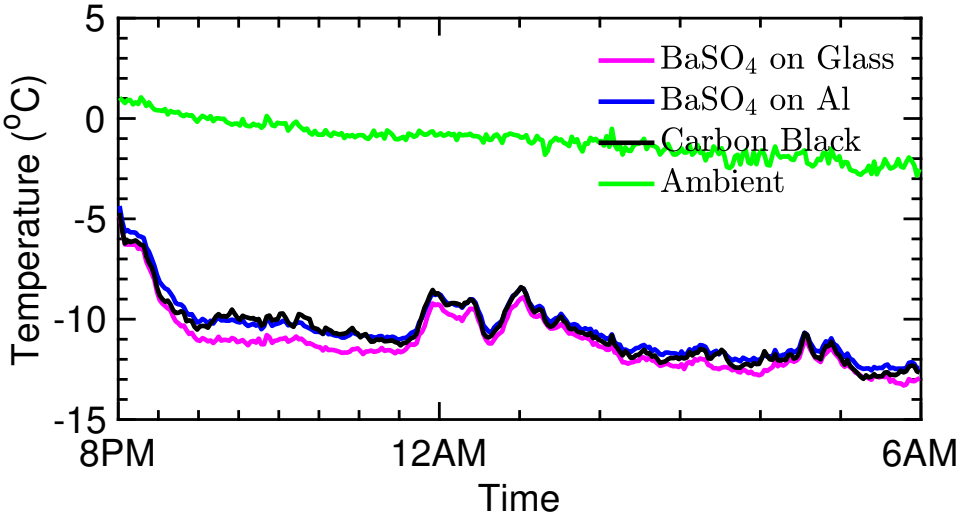

Figure 6.11. : The cooling power of $BaSO_4$ films on different substrates is compared during the night time to show the effect of substrate.

Calcite powders cost only 1 cent to 4 cents per kilograms, which is even cheaper than TiO_2. Industrial grade lithopone powders cost less than \$1/kg, consisting most of $BaSO_4$ and ZnS particles. The cost of the particle fillers for covering $100\mathrm{m}^2$ area is less than \$1.5 for $CaCO_3$ and around \$25 for $BaSO_4$ film, while it is around \$1.7 for TiO_2 fillers. With a similar manufacture process with commercial paint, there is no additional cost to adopt new fabrication techniques.

The Heat Island group at the Lawrence Berkeley National Lab has performed comprehensive testing with 85% solar reflectance roofing materials and concluded that their energy savings to be 40 to 75$\mathrm{Wh}/\mathrm{m}^2/\mathrm{day}$ depending on different buildings [125]. Our two cooling paints show higher performance with over 95% and 97% solar reflectance, respectively. With total solar energy around 5000$\mathrm{Wh}/\mathrm{m}^2/\mathrm{day}$, the higher solar reflectances of our paints account for additional energy savings around 33 to 46$\mathrm{Wh}/\mathrm{m}^2/\mathrm{day}$.

Reliability Testing and Other Designs

A brief reliability test is conducted by exposing $CaCO_3$ paint outdoor continuous for 20 days under various weather conditions. The sky window emissivity is measured at the beginning and the end of the test, both shows 0.92. The solar reflectance is measured every several day, shown in Fig. 6.12. Though a particle film of $BaSO_4$ is not as durable as $CaCO_3$ paint, it is still an excellent filler option once embedded in a matrix to enhance reliability. In this study, two other designs with 30% $BaSO_4$ in PVA and 60% $BaSO_4$ in acrylic produce 98% solar reflectance and 0.94 sky window emissivity, shown in Fig. 6.13.

Invisible Infrared Ink

Due to the difference in the solar reflectance, our cooling paints will maintain a lower temperature than commercial white paints under direct sunlight during the day, though both looking white. A pattern formed with both paints may be obscured visually, but it will be more distinguished under an infrared camera which picks up the temperature difference. The ”invisible” patterns could be further utilized for concealing information from naked

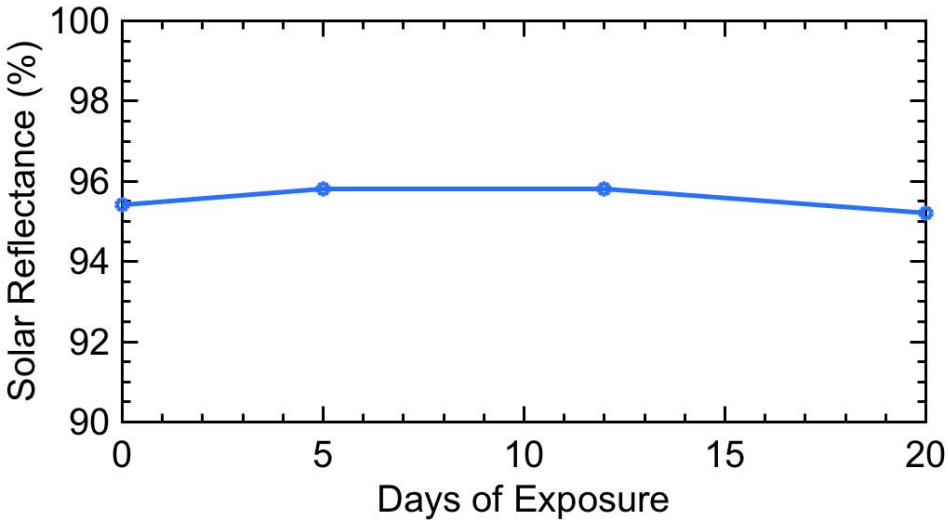

Figure 6.12. : The solar reflectance of $CaCO_3$ paint remains the same throughout the 20-day reliability test.

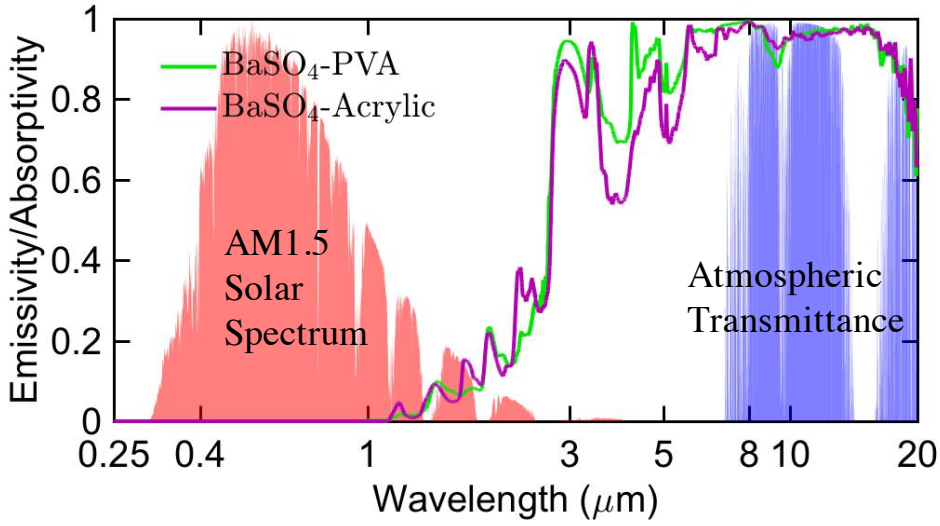

Figure 6.13. : Emissivity is measured for two other paint designs involving $BaSO_4$ from 250nm to $20\,\mu m$

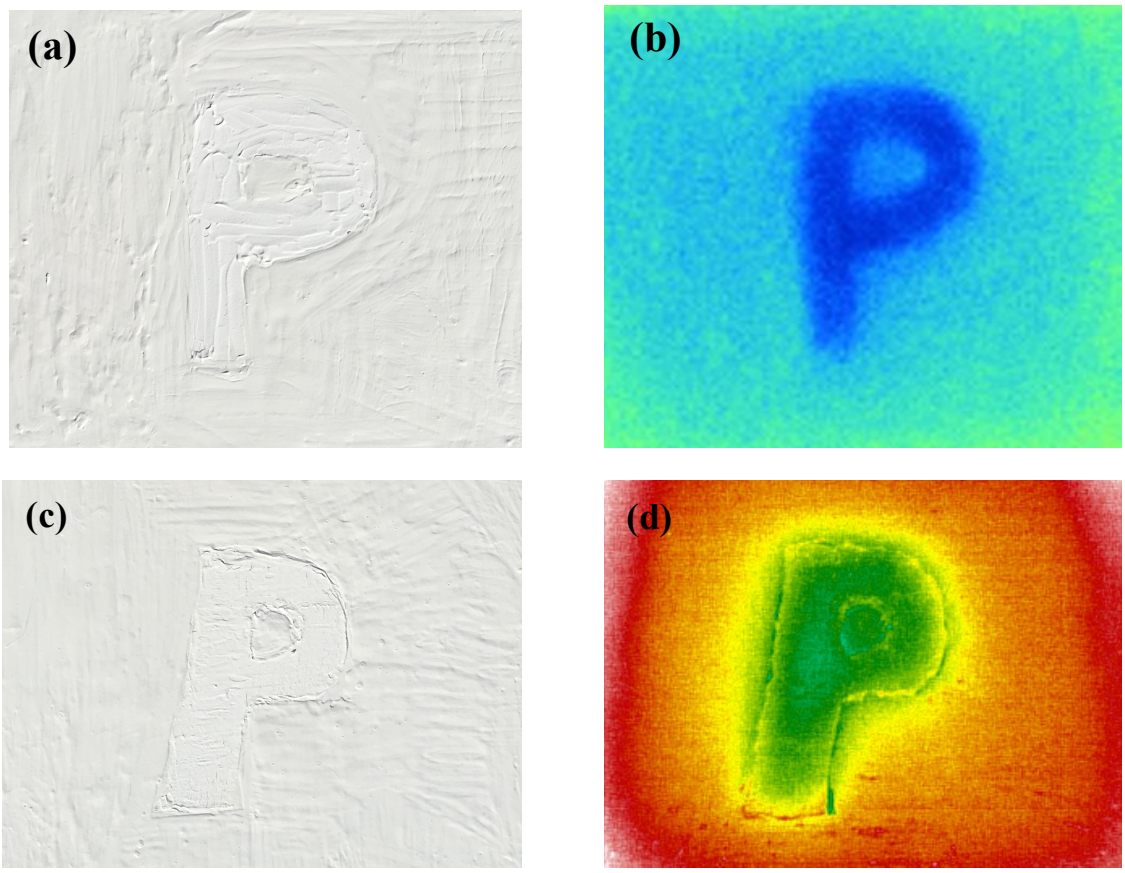

Figure 6.14. : (a)(b) are the first trials under visible light and infrared camera respectively. (c)(d) are the second trials with the same setup. In both trials, the letter P is painted with $BaSO_4$ paint and other areas are coated with commercial white paint.

eyes, but revealing under infrared light range. Several trials have been made to illustrate the applications on a wood board, shown in Fig. 6.14, where the letter P is painted with $BaSO_4$ paint and other areas are coated with commercial white paint. Though the pattern P is still visible but subtle under naked eye due to paint finishes and brush strokes, it is much more pronounced under an infrared camera. We believe that by optimizing and matching both paints closer, it is possible to effectively hide the pattern under visible light while remaining a clear picture under infrared light.

6.5 Conclusion

In conclusion, we have demonstrated that with the $CaCO_3$ and $BaSO_4$ nanoparticle fillers, we can achieve ultra-efficient below-ambient cooling with paints under direct sunlight. They were selected for their large intrinsic band gaps which help minimize the absorption in UV range. The appropriate particle sizes and high particle concentrations help strongly reflect the sunlight. The vibrational resonances of the particles or acrylic matrix provide strong emission in the sky window. These factors work coordinately to maximize the cooling performance. Our $BaSO_4$ film shows an ultra-high solar reflectance of 97.6% which is unseen in other paints, and a high sky-window emissivity over 0.93, resulting in $>$110 W/m^2 cooling power over the 10am to 2pm period when the average solar irradiation is 930 W/m^2. Our radiative cooling paints show comparable or better cooling performance than the other state-of-the-art approaches, while offering unprecedented benefits including the convenient paint form, a fraction of the cost of the other approaches, and the compatibility with commercial paint fabrication process.

REFERENCES

REFERENCES

[1] Ellis B. *Chemistry and technology of epoxy resins*. New York, NY: Blackie Academic & Professional, 1993.

[2] Ji-Hwan Lee, Seung-Hyun Lee, Chul Jin Choi, Seok Pil Jang, and Stephen U. S. Choi. A Review of Thermal Conductivity Data, Mechanisms and Models for Nanofluids. *International Journal of Micro-Nano Scale Transport*, 1(4):269–322, 2011.

[3] S Lee, David G Cahill, and Thomas H Allen. Thermal conductivity. *Physical Review B*, 52(1), 1995.

[4] M Wang and N Pan. Predictions of effective physical properties of complex multiphase materials. *Materials Science and Engineering: R: Reports*, 63(1):1–30, dec 2008.

[5] J.C. Maxwell. *A treatise on electricity and magnetism*. Dover Publications, 1954.

[6] J. C. M. Garnett. Colours in Metal Glasses, in Metallic Films, and in Metallic Solutions. II. *Philosophical Transactions of the Royal Society A: Mathematical, Physical and Engineering Sciences*, 205(387-401):237–288, 1906.

[7] R. L. Hamilton and O. K. Crosser. Thermal conductivity of heterogeneous two-component systems. *Industrial & Engineering Chemistry Fundamentals*, 1(3):187–191, 1962.

[8] Austin Minnich and Gang Chen. Modified effective medium formulation for the thermal conductivity of nanocomposites. *Applied Physics Letters*, 91(7):073105, 2007.

[9] Ce-Wen Nan, R. Birringer, David R. Clarke, and H. Gleiter. Effective thermal conductivity of particulate composites with interfacial thermal resistance. *Journal of Applied Physics*, 81(10):6692, 1997.

[10] A Eucken. Thermal conductivity of ceramic refractory materials: calculation from thermal conductivities of constituents. *Forsch. Gebiete Ingenieurw*, B3(353):16, 1932.

[11] Rolf Landauer. The electrical resistance of binary metallic mixtures. *Journal of Applied Physics*, 23(7):779–784, 1952.

[12] Guoqing Zhang, Yanping Xia, Hui Wang, Yu Tao, Guoliang Tao, Shantung Tu, and Haiping Wu. A Percolation Model of Thermal Conductivity for Filled Polymer Composites. *Journal of Composite Materials*, 44(8):963–970, 2010.

[13] Ce-Wen Nan. Physics of inhomogeneous inorganic materials. *Progress in Materials Science*, 37(1):1 – 116, 1993.

[14] C.-W. Nan, Y. Shen, and Jing Ma. Physical Properties of Composites Near Percolation. *Annual Review of Materials Research*, 40(1):131–151, 2010.

[15] Bu Xuan Wang, Le Ping Zhou, and Xiao Feng Peng. A fractal model for predicting the effective thermal conductivity of liquid with suspension of nanoparticles. *International Journal of Heat and Mass Transfer*, 46(14):2665–2672, 2003.

[16] P Meakin, I Majid, S Havlin, and H E Stanley. Topological properties of diffusion limited aggregation and cluster-cluster aggregation. *Journal of Physics A: Mathematical and General*, 17(18):L975–L981, 1999.

[17] Paul Meakin. Fractal aggregates. *Advances in Colloid and Interface Science*, 28:249–331, 1987.

[18] Kamyar Pashayi, Hafez Raeisi Fard, Fengyuan Lai, Sushumna Iruvanti, Joel Plawsky, and Theodorian Borca-Tasciuc. High thermal conductivity epoxy-silver composites based on self-constructed nanostructured metallic networks. *Journal of Applied Physics*, 111(10):104310, 2012.

[19] Indira Seshadri, Gibran L. Esquenazi, Theodorian Borca-Tasciuc, Pawel Keblinski, and Ganpati Ramanath. Multifold Increases in Thermal Conductivity of Polymer Nanocomposites through Microwave Welding of Metal Nanowire Fillers. *Advanced Materials Interfaces*, 2(15):1–6, 2015.

[20] S.-M. Lee and David G. Cahill. Heat transport in thin dielectric films. *Journal of Applied Physics*, 81(6):2590, mar 1997.

[21] R. J. Stoner and H. J. Maris. Kapitza conductance and heat flow between solids at temperatures from 50 to 300 K. *Physical Review B*, 48(22):16373–16387, dec 1993.

[22] Robert J. Stevens, Andrew N. Smith, and Pamela M. Norris. Measurement of Thermal Boundary Conductance of a Series of Metal-Dielectric Interfaces by the Transient Thermoreflectance Technique. *Journal of Heat Transfer*, 127(3):315, mar 2005.

[23] A. J. Griffin, F. R. Brotzen, and P. J. Loos. Effect of thickness on the transverse thermal conductivity of thin dielectric films. *Journal of Applied Physics*, 75(8):3761, apr 1994.

[24] Jung Hun Kim, Albert Feldman, and Donald Novotny. Application of the three omega thermal conductivity measurement method to a film on a substrate of finite thickness. *Journal of Applied Physics*, 86(7):3959, oct 1999.

[25] David G. Cahill. Thermal conductivity measurement from 30 to 750 K: the 3ω method. *Review of Scientific Instruments*, 61(2):802, 1990.

[26] David G. Cahill. Thermal conductivity of thin films: Measurements and understanding. *Journal of Vacuum Science & Technology A: Vacuum, Surfaces, and Films*, 7(3):1259, may 1989.

[27] T. Borca-Tasciuc, a. R. Kumar, and G. Chen. Data reduction in 3ω method for thin-film thermal conductivity determination. *Review of Scientific Instruments*, 72(4):2139, 2001.

[28] David G. Cahill, Wayne K. Ford, Kenneth E. Goodson, Gerald D. Mahan, Arun Majumdar, Humphrey J. Maris, Roberto Merlin, and Simon R. Phillpot. Nanoscale thermal transport. *Journal of Applied Physics*, 93(2):793, 2003.

[29] Edward Dechaumphai, Dylan Lu, Jimmy J Kan, Jaeyun Moon, Eric E Fullerton, Zhaowei Liu, and Renkun Chen. Ultralow thermal conductivity of multilayers with highly dissimilar Debye temperatures. *Nano letters*, 14(5):2448–55, may 2014.

[30] W A Little. THE TRANSPORT OF HEAT BETWEEN DISSIMILAR SOLIDS AT LOW TEMPERATURES. *Canadian Journal of Physics*, 37(3):334–349, 1959.

[31] E. Swartz and R. Pohl. Thermal boundary resistance. *Reviews of Modern Physics*, 61(3):605–668, jul 1989.

[32] Ravi S. Prasher and Patrick E. Phelan. A Scattering-Mediated Acoustic Mismatch Model for the Prediction of Thermal Boundary Resistance. *Journal of Heat Transfer*, 123(1):105, 2001.

[33] Arun Majumdar and Pramod Reddy. Role of electronâĂŞphonon coupling in thermal conductance of metalâĂŞnonmetal interfaces. *Applied Physics Letters*, 84(23):4768, 2004.

[34] Timothy S. English, John C. Duda, Justin L. Smoyer, Donald A. Jordan, Pamela M. Norris, and Leonid V. Zhigilei. Enhancing and tuning phonon transport at vibrationally mismatched solid-solid interfaces. *Physical Review B*, 85(3):035438, jan 2012.

[35] Yan Wang, Zexi Lu, Ajit K. Roy, and Xiulin Ruan. Effect of interlayer on interfacial thermal transport and hot electron cooling in metal-dielectric systems: An electron-phonon coupling perspective. *Journal of Applied Physics*, 119(6):065103, feb 2016.

[36] Yan Wang, Xiulin Ruan, and Ajit K. Roy. Two-temperature nonequilibrium molecular dynamics simulation of thermal transport across metal-nonmetal interfaces. *Physical Review B*, 85(20):205311, may 2012.

[37] Zijian Li, Si Tan, Elah Bozorg-Grayeli, Takashi Kodama, Mehdi Asheghi, Gil Delgado, Matthew Panzer, Alexander Pokrovsky, Daniel Wack, and Kenneth E Goodson. Phonon dominated heat conduction normal to Mo/Si multilayers with period below 10 nm. *Nano letters*, 12(6):3121–6, jun 2012.

[38] Maria N Luckyanova, Jivtesh Garg, Keivan Esfarjani, Adam Jandl, Mayank T Bulsara, Aaron J Schmidt, Austin J Minnich, Shuo Chen, Mildred S Dresselhaus, Zhifeng Ren, Eugene a Fitzgerald, and Gang Chen. Coherent phonon heat conduction in superlattices. *Science (New York, N.Y.)*, 338(6109):936–9, nov 2012.

[39] Jayakanth Ravichandran, Ajay K Yadav, Ramez Cheaito, Pim B Rossen, Arsen Soukiassian, S J Suresha, John C Duda, Brian M Foley, Che-Hui Lee, Ye Zhu, Arthur W Lichtenberger, Joel E Moore, David a Muller, Darrell G Schlom, Patrick E Hopkins, Arun Majumdar, Ramamoorthy Ramesh, and Mark a Zurbuchen. Crossover from incoherent to coherent phonon scattering in epitaxial oxide superlattices. *Nature materials*, 13(2):168–72, feb 2014.

[40] Yan Wang, Haoxiang Huang, and Xiulin Ruan. Decomposition of coherent and incoherent phonon conduction in superlattices and random multilayers. *Physical Review B*, 90(16):165406, oct 2014.

[41] S. Catalanotti, V. Cuomo, G. Piro, D. Ruggi, V. Silvestrini, and G. Troise. The radiative cooling of selective surfaces. *Solar Energy*, 17(2):83–89, 1975.

[42] A.W. Harrison and M.R. Walton. Radiative cooling of tio2 white paint. *Solar Energy*, 20(2):185 – 188, 1978.

[43] C. G. Granqvist and A. Hjortsberg. Radiative cooling to low temperatures: General considerations and application to selectively emitting SiO films. *Journal of Applied Physics*, 52(6):4205–4220, 1981.

[44] A Andretta, B Bartoli, B Coluzzi, V Cuomo, A Andretta, B Bartoli, B Coluzzi, V Cuomo Selective, and Surfaces For. Selective surfaces for natural cooling devices. *Journal de Physique Colloques*, 42(C1):C1–423–C1–430, 1981.

[45] E. M. Lushiku, A. Hjortsberg, and C. G. Granqvist. Radiative cooling with selectively infrared-emitting ammonia gas. *Journal of Applied Physics*, 53(8):5526–5530, 1982.

[46] Elias M. Lushiku and Claes-Goran Granqvist. Radiative cooling with selectively infrared-emitting gases. *Applied Optics*, 23(11):1835, 1984.

[47] B. Orel, M. Klanjšek Gunde, and A. Krainer. Radiative cooling efficiency of white pigmented paints. *Solar Energy*, 50(6):477–482, 1993.

[48] Deda M. Diatezua, Paul A. Thiry, Alain Dereux, and Roland Caudano. Silicon oxynitride multilayers as spectrally selective material for passive radiative cooling applications. *Solar Energy Materials and Solar Cells*, 40(3):253–259, 1996.

[49] A. R. Gentle and G. B. Smith. Radiative heat pumping from the Earth using surface phonon resonant nanoparticles. *Nano Letters*, 10(2):373–379, 2010.

[50] Zhifeng Huang and Xiulin Ruan. Nanoparticle embedded double-layer coating for daytime radiative cooling. *International Journal of Heat and Mass Transfer*, 104:890–896, 2017.

[51] Hua Bao, Chen Yan, Boxiang Wang, Xing Fang, C. Y. Zhao, and Xiulin Ruan. Double-layer nanoparticle-based coatings for efficient terrestrial radiative cooling. *Solar Energy Materials and Solar Cells*, 168(November 2016):78–84, 2017.

[52] Sarun Atiganyanun, John Plumley, Seok Jun Han, Kevin Hsu, Jacob Cytrynbaum, Thomas L. Peng, Sang Min Han, and Sang Eon Han. Effective Radiative Cooling by Paint-Format Microsphere-Based Photonic Random Media. *ACS Photonics*, page acsphotonics.7b01492, 2018.

[53] Eden Rephaeli, Aaswath Raman, and Shanhui Fan. Ultrabroadband photonic structures to achieve high-performance daytime radiative cooling. *Nano Letters*, 13(4):1457–1461, 2013.

[54] Aaswath P Raman, Marc Abou Anoma, Linxiao Zhu, Eden Rephaeli, and Shanhui Fan. Passive radiative cooling below ambient air temperature under direct sunlight. *Nature*, 515(7528):540–4, 2014.

[55] Yao Zhai, Yaoguang Ma, Sabrina N David, Dongliang Zhao, Runnan Lou, Gang Tan, Ronggui Yang, and Xiaobo Yin. Scalable-manufactured randomized glass-polymer hybrid metamaterial for daytime radiative cooling. *Science*, 7899:1–9, 2017.

[56] Jun-long Kou, Zoila Jurado, Zhen Chen, Shanhui Fan, and Austin J. Minnich. Daytime radiative cooling using near-black infrared emitters. *ACS Photonics*, page acsphotonics.6b00991, 2017.

[57] Mats Gustafsson, Anders Karlsson, António Pedro Pontes Rebelo, and Björn Widenberg. Design of frequency selective windows for improved indoor outdoor communication. *IEEE Transactions on Antennas and Propagation*, 54(6):1897–1900, 2006.

[58] Ghaffer I. Kiani, Lars G. Olsson, Anders Karlsson, Karu P. Esselle, and Martin Nilsson. Cross-dipole bandpass frequency selective surface for energy-saving glass used in buildings. *IEEE Transactions on Antennas and Propagation*, 59(2):520–525, 2011.

[59] J Mandal, Y Fu, A Overvig, M Jia, K Sun, N Shi, H Zhou, X Xiao, N Yu, and Y Yang. Hierarchically porous polymer coatings for highly efficient passive daytime radiative cooling. *Science*, page eaat9513, 2018.

[60] Robert F. Service. Cool paint job fights solar warmth. *Science*, 361(6409):1303–1303, 2018.

[61] Midwest Tungsten. How does Electron Beam Evaporation work? `https://www.tungsten.com/how-does-electron-beam-evaporation-work/`.

[62] Riikka L. Puurunen. A short history of atomic layer deposition: Tuomo Suntola's atomic layer epitaxy. *Chemical Vapor Deposition*, 20(10-12):332–344, 2014.

[63] Xiangyu Li, Wonjun Park, Yong P. Chen, and Xiulin Ruan. Effect of Particle Size and Aggregation on Thermal Conductivity of Metal-Polymer Nanocomposite. *Journal of Heat Transfer*, 139(2):022401, oct 2016.

[64] S H Hsu, C W Chou, and S M Tseng. Enhanced thermal and mechanical properties in polyurethane/Au nanocomposites. *Macromolecular Materials and Engineering*, 289(12):1096–1101, 2004.

[65] N.R. Karthikeyan, John Philip, and Baldev Raj. Effect of clustering on the thermal conductivity of nanofluids. *Materials Chemistry and Physics*, 109(1):50–55, may 2008.

[66] Iván Pardiñas-Blanco, Cristina E. Hoppe, M.a. López-Quintela, and J. Rivas. Control on the dispersion of gold nanoparticles in an epoxy network. *Journal of Non-Crystalline Solids*, 353(8-10):826–828, apr 2007.

[67] John Philip, P D Shima, and Baldev Raj. Evidence for enhanced thermal conduction through percolating structures in nanofluids. *Nanotechnology*, 19(30):305706, 2008.

[68] John Philip, P. D. Shima, and Baldev Raj. Nanofluid with tunable thermal properties. *Applied Physics Letters*, 92(4):2–5, 2008.

[69] John Philip, P. D. Shima, and Baldev Raj. Enhancement of thermal conductivity in magnetite based nanofluid due to chainlike structures. *Applied Physics Letters*, 91(20):2–5, 2007.

[70] Benjamin N. Reinecke, Jerry W. Shan, Karl K. Suabedissen, and Anna S. Cherkasova. On the anisotropic thermal conductivity of magnetorheological suspensions. *Journal of Applied Physics*, 104(2), 2008.

[71] Shuying Wu, Raj B. Ladani, Jin Zhang, Anthony J. Kinloch, Zhiheng Zhao, Jun Ma, Xuehua Zhang, Adrian P. Mouritz, Kamran Ghorbani, and Chun H. Wang. Epoxy nanocomposites containing magnetite-carbon nanofibers aligned using a weak magnetic field. *Polymer*, 68:25 – 34, 2015.

[72] Haitao Zhu, Canying Zhang, Shiquan Liu, Yaming Tang, and Yansheng Yin. Effects of nanoparticle clustering and alignment on thermal conductivities of fe3o4 aqueous nanofluids. *Applied Physics Letters*, 89(2), 2006.

[73] Ravi Prasher, William Evans, Paul Meakin, Jacob Fish, Patrick Phelan, and Pawel Keblinski. Effect of aggregation on thermal conduction in colloidal nanofluids. *Applied Physics Letters*, 89(14):1–4, 2006.

[74] William Evans, Ravi Prasher, Jacob Fish, Paul Meakin, Patrick Phelan, and Pawel Keblinski. Effect of aggregation and interfacial thermal resistance on thermal conductivity of nanocomposites and colloidal nanofluids. *International Journal of Heat and Mass Transfer*, 51(5-6):1431–1438, mar 2008.

[75] G. Chen. Thermal conductivity and ballistic-phonon transport in the cross-plane direction of superlattices. *Physical Review B*, 57(23):14958–14973, jun 1998.

[76] Chenggang Chen and David Curliss. Evolution of Epoxy Nanocomposites. *Applied of Polymer Science*, 2(1), 2003.

[77] Z. Hashin and S. Shtrikman. A Variational approach to the theory of the effective magnetic permeability of multiphase materials. *Journal of Applied Physics*, 33(10):3125–3131, 1962.

[78] M.ĂL'S. Toprak, C. Stiewe, D. Platzek, S. Williams, L. Bertini, E. Muller, C. Gatti, Y. Zhang, M. Rowe, and M. Muhammed. The impact of nanostructuring on the thermal conductivity of thermoelectric cosb3. *Advanced Functional Materials*, 14(12):1189–1196, 2004.

[79] Wee-Liat Ong, Shubhaditya Majumdar, Jonathan A. Malen, and Alan J. H. McGaughey. Coupling of organic and inorganic vibrational states and their thermal transport in nanocrystal arrays. *The Journal of Physical Chemistry C*, 118(14):7288–7295, 2014.

[80] Daniele Cangialosi, Virginie M. Boucher, Angel Alegría, and Juan Colmenero. Enhanced physical aging of polymer nanocomposites: The key role of the area to volume ratio. *Polymer*, 53(6):1362–1372, 2012.

[81] D. P N Vlasveld, H. E N Bersee, and S. J. Picken. Creep and physical aging behaviour of PA6 nanocomposites. *Polymer*, 46(26):12539–12545, 2005.

[82] Virginie M. Boucher, Daniele Cangialosi, Angel Alegrìa, Juan Colmenero, Juan González-Irun, and Luis M. Liz-Marzan. Physical aging in PMMA/silica nanocomposites: Enthalpy and dielectric relaxation. *Journal of Non-Crystalline Solids*, 357(2):605–609, 2011.

[83] Dongjun Wang and Toyoko Imae. Morphological Dependence of Fluorescence Emitted from PbS/PAMAM Dendrimer Nanocomposite. *Chemistry Letters*, 34(5):640–641, 2005.

[84] Marjorie J Vold. Computer simulation of floc formation in a colloidal suspension. *Journal of Colloid Science*, 18(7):684–695, 1963.

[85] David N Sutherland. A theoretical model of floc structure. *Journal of Colloid and Interface Science*, 25(3):373–380, 1967.

[86] DN Sutherland. Chain formation of fine particle aggregates. *Nature*, 226(5252):1241, 1970.

[87] DN Sutherland and I Goodarz-Nia. Floc simulation: the effect of collision sequence. *Chemical Engineering Science*, 26(12):2071–2085, 1971.

[88] RC Ball, DA Weitz, TA Witten, and F Leyvraz. Universal kinetics in reaction-limited aggregation. *Physical review letters*, 58(3):274, 1987.

[89] M. Rottereau, J. C. Gimel, T. Nicolai, and D. Durand. Monte Carlo simulation of particle aggregation and gelation: II. Pair correlation function and structure factor. *European Physical Journal E*, 15(2):141–148, 2004.

[90] M. Rottereau, J. C. Gimel, T. Nicolai, and D. Durand. Monte Carlo simulation of particle aggregation and gelation: I. Growth, structure and size distribution of the clusters. *European Physical Journal E*, 15(2):133–140, 2004.

[91] R. Iwao, Y. Matsuda, H. Yamaguchi, and T. Niimi. Study on diffusion process of nanoparticles in a pdms layer using spt technique. In *2015 International Symposium on Micro-NanoMechatronics and Human Science (MHS)*, pages 1–3, Nov 2015.

[92] Clinton Van Siclen. Walker diffusion method for calculation of transport properties of finite composite systems. *Physical Review E*, 65(2):26144, 2002.

[93] Xiangyu Li, Wonjun Park, Yong P Chen, and Xiulin Ruan. Thermal interfacial resistance reduction between metal and dielectric materials by inserting intermediate metal layer. In *ASME 2016 Heat Transfer Summer Conference*, pages V001T04A006–V001T04A006. American Society of Mechanical Engineers, 2016.

[94] Baratunde a. Cola, Jun Xu, Changrui Cheng, Xianfan Xu, Timothy S. Fisher, and Hanping Hu. Photoacoustic characterization of carbon nanotube array thermal interfaces. *Journal of Applied Physics*, 101(5):1–9, 2007.

[95] C. Dames. Theoretical phonon thermal conductivity of Si/Ge superlattice nanowires. *Journal of Applied Physics*, 95(2):682, 2004.

[96] Liang Pan and David B Bogy. Data storage: Heat-assisted magnetic recording. *Nature Photonics*, 3(4):189, 2009.

[97] W. A. Challener, Chubing Peng, A. V. Itagi, D. Karns, Wei Peng, Yingguo Peng, XiaoMin Yang, Xiaobin Zhu, N. J. Gokemeijer, Y. T. Hsia, G. Ju, Robert E. Rottmayer, Michael A. Seigler, and E. C. Gage. Heat-assisted magnetic recording by a near-field transducer with efficient optical energy transfer. *Nature Photonics*, 3:220 EP –, 03 2009.

[98] M. A. Seigler, W. A. Challener, E. Gage, N. Gokemeijer, G. Ju, B. Lu, K. Pelhos, C. Peng, R. E. Rottmayer, X. Yang, H. Zhou, and T. Rausch. Integrated heat assisted magnetic recording head: Design and recording demonstration. *IEEE Transactions on Magnetics*, 44(1):119–124, Jan 2008.

[99] Yibin Xu, Haitao Wang, Yoshihisa Tanaka, Masato Shimono, and Masayoshi Yamazaki. Measurement of Interfacial Thermal Resistance by Periodic Heating and a Thermo-Reflectance Technique. *Materials Transactions*, 48(2):148–150, 2007.

[100] M. Specht, H. Reisinger, F. Hofmann, T. Schulz, E. Landgraf, R.J. Luyken, W. RÃűsner, M. Grieb, and L. Risch. Charge trapping memory structures with al2o3 trapping dielectric for high-temperature applications. *Solid-State Electronics*, 49(5):716 – 720, 2005. 5th International Workshop on the Ultimate Intergration of Silicon, ULIS 2004.

[101] PD Ye, B Yang, KK Ng, J Bude, GD Wilk, S Halder, and JCM Hwang. Gan metal-oxide-semiconductor high-electron-mobility-transistor with atomic layer deposited al2o3 as gate dielectric. *Applied Physics Letters*, 86(6):063501, 2005.

[102] A. Lahmar, T. P. Nguyen, D. Sakami, S. Orain, Y. Scudeller, and F. Danes. Experimental Investigation on the Thermal Contact Resistance Between Gold Coating and Ceramic Substrates. *Thin Solid Films*, 389(1-2):167–172, 2001.

[103] Minyoung Jeong, Justin P. Freedman, Hongliang Joe Liang, Cheng-Ming Chow, Vincent M. Sokalski, James A. Bain, and Jonathan A. Malen. Enhancement of Thermal Conductance at Metal-Dielectric Interfaces Using Subnanometer Metal Adhesion Layers. *Physical Review Applied*, 5(1):014009, jan 2016.

[104] W Kern and D a Puotinen. Cleaning solutions based on hydrogen peroxide for use in silicon semiconductor technology. *Rca Review*, 31(2):187–206, 1970.

[105] Mallory E. DeCoster, Kelsey E. Meyer, Brandon D. Piercy, John T. Gaskins, Brian F. Donovan, Ashutosh Giri, Nicholas A. Strnad, Daniel M. Potrepka, Adam A. Wilson, Mark D. Losego, and Patrick E. Hopkins. Density and Size Effects on the Thermal Conductivity of Atomic Layer Deposited TiO2 and Al2O3 Thin Films. *Thin Solid Films*, 650(January):71–77, 2018.

[106] D M Duffy and A M Rutherford. Including the effects of electronic stopping and electronâĂŞion interactions in radiation damage simulations. *Journal of Physics: Condensed Matter*, 19(1):16207, 2007.

[107] Zhibin Lin, Leonid Zhigilei, and Vittorio Celli. Electron-phonon coupling and electron heat capacity of metals under conditions of strong electron-phonon nonequilibrium. *Physical Review B*, 77(7):075133, feb 2008.

[108] L. Koči, E. M. Bringa, D. S. Ivanov, J. Hawreliak, J. McNaney, A. Higginbotham, L. V. Zhigilei, A. B. Belonoshko, B. A. Remington, and R. Ahuja. Simulation of shock-induced melting of Ni using molecular dynamics coupled to a two-temperature model. *Physical Review B*, 74(1):012101, 2006.

[109] Reese E. Jones, Jeremy A. Templeton, Gregory J. Wagner, David Olmsted, and Nomand A. Modine. Electron transport enhanced molecular dynamics for metals and semi-metals. *International Journal for Numerical Methods in Engineering*, 83(8-9):940–967, aug 2010.

[110] T.S. Fisher. *Thermal Energy at the Nanoscale*. Lessons from Nanoscience. World Scientific, 2013.

[111] Carolyn L. Phillips and Paul S. Crozier. An energy-conserving two-temperature model of radiation damage in single-component and binary Lennard-Jones crystals. *Journal of Chemical Physics*, 131(2009):0–11, 2009.

[112] Yan Wang, Zexi Lu, and Xiulin Ruan. First principles calculation of lattice thermal conductivity of metals considering phonon-phonon and phonon-electron scattering. *Journal of Applied Physics*, 119(22):225109, 2016.

[113] A Lahmar, N Hmina, Y Scudeller, and J.P Bardon. Correlation Between the Adhesion and the Thermal Contact Resistance: Effects of Substrate Surface Ion Bombardment Etching. *Thin Solid Films*, 325(1-2):156–162, 1998.

[114] T. P. Nguyen, J. Ip, P. Le Rendu, and A. Lahmar. Improved Adhesion of Gold Coatings on Ceramic Substrates by Thermal Treatment. *Surface and Coatings Technology*, 141(1):108–114, 2001.

[115] Xiangyu Li, Wonjun Park, Yong P Chen, and Xiulin Ruan. Absence of coupled thermal interfaces in al2o3/ni/al2o3 sandwich structure. *Applied Physics Letters*, 111(14):143102, 2017.

[116] Jayakanth Ravichandran, Ajay K Yadav, Ramez Cheaito, Pim B Rossen, Arsen Soukiassian, S J Suresha, John C Duda, Brian M Foley, Che-Hui Lee, Ye Zhu, Arthur W Lichtenberger, Joel E Moore, David a Muller, Darrell G Schlom, Patrick E Hopkins, Arun Majumdar, Ramamoorthy Ramesh, and Mark a Zurbuchen. Crossover from incoherent to coherent phonon scattering in epitaxial oxide superlattices. *Nature materials*, 13(2):168–72, feb 2014.

[117] Jingjing Shi, Yalin Dong, Timothy Fisher, and Xiulin Ruan. Thermal transport across carbon nanotube-graphene covalent and van der Waals junctions. *Journal of Applied Physics*, 118(4):044302, jul 2015.

[118] Yee Kan Koh, Suzanne L. Singer, Woochul Kim, Joshua M O Zide, Hong Lu, David G. Cahill, Arun Majumdar, and Arthur C. Gossard. Comparison of the 3ω method and time-domain thermoreflectance for measurements of the cross-plane thermal conductivity of epitaxial semiconductors. *Journal of Applied Physics*, 105(5), 2009.

[119] P. Heino and E. Ristolainen. Thermal conduction at the nanoscale in some metals by MD. *Microelectronics Journal*, 34(9):773–777, 2003.

[120] Yuan Shiping and Jiang Peixue. Thermal conductivity of nanoscale thin nickel films. *Progress in Natural Science*, 15(10):922–929, oct 2005.

[121] U.S. Energy Information Administration. Annual Energy Outlook 2018 with projections to 2050. *Journal of Physics A: Mathematical and Theoretical*, 44(8):1–64, 2018.

[122] Louis Lorenz. *Lysbevægelsen i og uden for en af plane Lysbølger belyst Kugle*. na, 1890.

[123] Gustav Mie. Beiträge zur optik trüber medien, speziell kolloidaler metallösungen. *Annalen der physik*, 330(3):377–445, 1908.

[124] Angus R. Gentle and Geoff B. Smith. A Subambient Open Roof Surface under the Mid-Summer Sun. *Advanced Science*, 2(9):2–5, 2015.

[125] Hashem Akbari, Ronnen Levinson, and Leo Rainer. Monitoring the energy-use effects of cool roofs on California commercial buildings. *Energy and Buildings*, 37(10):1007–1016, 2005.

VITA

VITA

Xiangyu Li was born in Changchun, Jilin Province, China. He obtained his Bachelor of Science in Electrical Engineering, Tsinghua University, Beijing, China. Then he was admitted to the School of Mechanical Engineering at Purdue University in 2012 for a direct Ph.D. degree, joining Prof. Xiulin Ruan's group Nanoscale Energy Transport and Conversion Laboratory. He mainly focuses on experiments with thin film interfacial resistance, thermal interface materials with metal nanoparticles, as well as passive radiative cooling paints. He is expected to receive his Ph.D. degree at the end of 2018.